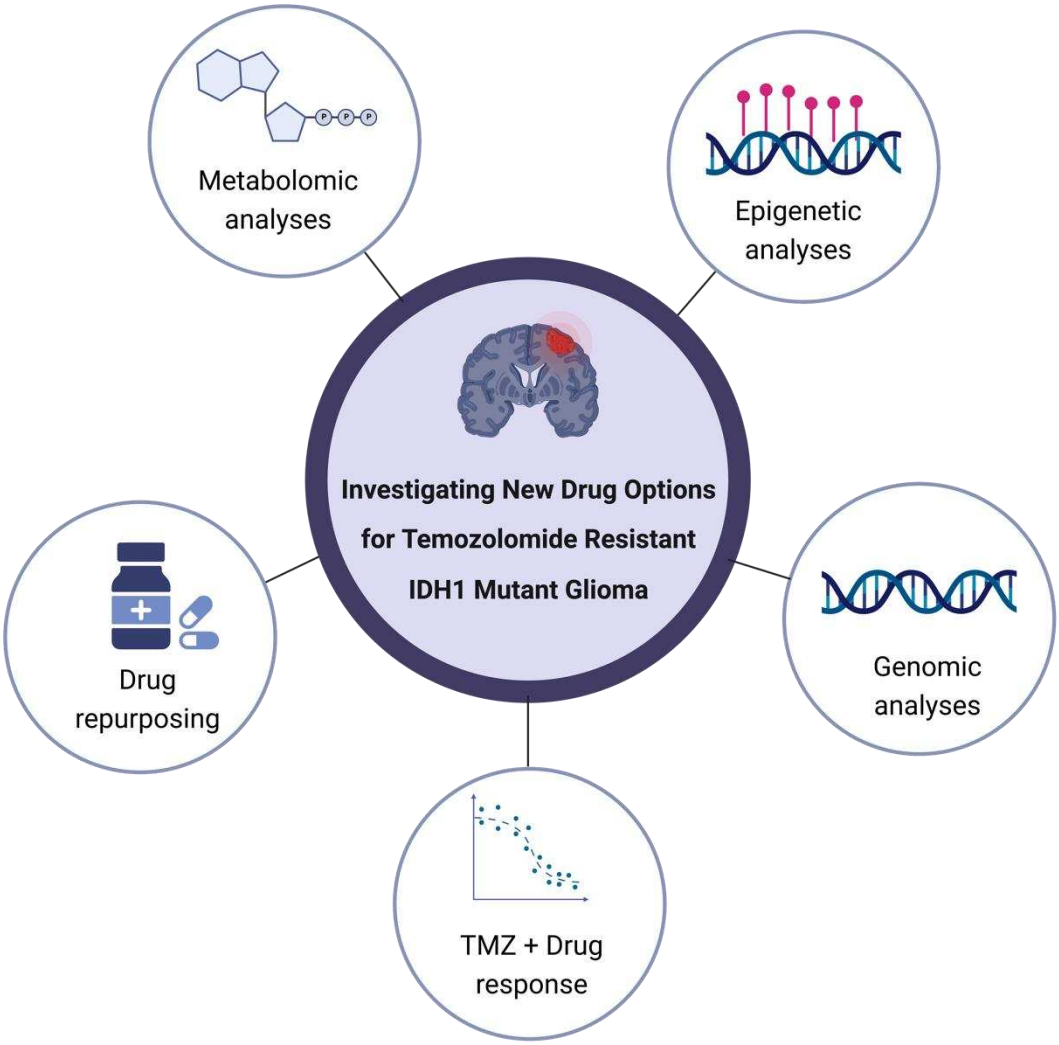

Presented by

M.Sc. Xueyuan Sun

Born in Kaifeng, China

Oral examination: 14.09.2023

Inaugural dissertation

for

obtaining the doctoral

degree of the

Combined Faculty of Mathematics, Engineering and Natural

Sciences of the

Ruprecht - Karls -

University Heidelberg

Presented by

M.Sc. Xueyuan Sun

Born in Kaifeng, China

Oral examination: 14.09.2023

Investigating New Drug Options for Temozolomide Resistant IDH1 Mutant Glioma

Referees:

Prof. Dr. Peter Angel

Dr. Sevin Turcan

Declaration

I hereby declare that I have written and submitted the dissertation „ Investigating New Drug Options for Temozolomide Resistant IDH1 Mutant Glioma “myself and in this process have not used any other sources than those expressly indicated.

I hereby declare that I have not applied to be examined at any other institution, nor have I used the dissertation in this or any other form at any other institution as an examination paper, nor submitted it to any other faculty as a dissertation.

Xueyuan Sun

Table of Contents

Summary

Gliomas, a prevalent form of malignant brain tumors in adults, often exhibit mutations in the isocitrate dehydrogenase 1 (IDH1) gene. Temozolomide (TMZ) is a commonly used chemotherapy drug for treating gliomas; however, the development of drug resistance poses a significant challenge to its effectiveness.

My study aimed to investigate new drug options for IDH1 mutant gliomas and was divided into two main parts. The first part focused on reversing TMZ resistance and identifying synergistic drugs, while the second part sought alternative treatments for IDH1 mutant TMZ-resistant gliomas.

To achieve the objectives of the first part, patient-derived glioma tumorspheres (PDTs) harboring IDH1 mutations were utilized. Vehicle and TMZ treated tumor models were subjected to transcriptional, metabolic, and epigenetic analyses. Transcriptome analysis revealed the upregulation of the p53 signaling pathway and its associated transcription factor, *TP53*. Notably, combining the p53 activator RITA with TMZ demonstrated strong synergy in certain PDTs. Metabolome analysis uncovered that glycolytic inhibition with the glucose analog 2-DG (2-Deoxy-D-glucose) or combining Mildronate, L-carnitine biosynthesis inhibitor, with TMZ treatment showed efficacy in specific PDTs. Additionally, employing epigenetic approaches using decitabine (DAC) in combination with TMZ revealed robust synergistic effects in select PDTs. These findings underscore the significance of genetic and metabolic heterogeneity among cells in gliomas.

In the pursuit of alternative drugs, a high-throughput miniaturized screening identified more than 20 potential candidate drugs, among which the YAP inhibitor Verteporfin (VP) emerged as a promising option. VP exhibited anti-tumor activity in IDH1 mutant PDTs independent of the YAP1 protein. It downregulated the nucleocytoplasmic transport pathway, with NUP107 identified as an upstream regulator associated with VP response.

In conclusion, this study elucidated the intricate interplay of signaling pathways and their impact on drug sensitivity in diverse glioma cell populations. It emphasized the need to consider the complexities inherent to gliomas when devising effective therapeutic strategies. The findings provide valuable insights into the development of alternative treatments and strategies to overcome TMZ resistance in IDH1 mutant gliomas.

Zusammenfassung

Gliome, eine häufige Form bösartiger Hirntumoren bei Erwachsenen, weisen häufig Mutationen im Isocitratdehydrogenase-1 (IDH1) Gen auf. Temozolomid (TMZ) wird häufig zur Behandlung von Gliomen eingesetzt, jedoch entwickelt sich oft eine Arzneimittelresistenz.

Die Studie untersuchte neue Optionen für IDH1-mutierte Gliome und bestand aus zwei Teilen: Umkehrung der TMZ-Resistenz und Identifizierung synergistischer Medikamente sowie alternative Behandlungen für IDH1-mutierte, TMZ-resistente Gliome.

Um diese Ziele zu erreichen, wurden patientenabgeleitete Gliom-Tumorsphären (PDTs) mit IDH1-Mutationen verwendet. Die Tumormodelle wurden auf transkriptionelle, metabolische und epigenetische Anfälligkeiten analysiert. Die Transkriptom-Analyse ergab eine Hochregulation des P53-Signalwegs und seines assoziierten Transkriptionsfaktors P53. Insbesondere zeigte die Kombination des P53-Aktivators RITA mit TMZ eine starke Synergie in bestimmten PDTs. Die Metabolom-Analyse ergab, dass die Hemmung des Glucosestoffwechsels mit 2-DG oder die Kombination von Mildronat mit TMZ eine Wirksamkeit in spezifischen PDTs zeigte. Zusätzlich zeigten epigenetische Ansätze unter Verwendung von Decitabin (DAC) in Kombination mit TMZ eine robuste Synergie in ausgewählten PDTs. Diese Ergebnisse verdeutlichen die Bedeutung der metabolischen Plastizitätsheterogenität in Gliomzellen.

Im Rahmen der Suche nach alternativen Medikamenten identifizierte ein Hochdurchsatz-Screening mehr als 20 potenzielle Kandidaten, unter denen Verteporfin (VP) als vielversprechende Option hervorstach. VP zeigte eine antitumorale Aktivität in IDH1-mutierten PDTs unabhängig vom YAP1-Signalweg. Es regulierte den nukleozytoplasmatischen Transportweg herunter, wobei NUP107 als ein upstream-Regulator in Verbindung mit der Reaktion auf VP identifiziert wurde.

Zusammenfassend beleuchtet diese Studie das komplexe Zusammenspiel von Signalwegen und deren Auswirkungen auf die Arzneimittelsensitivität in unterschiedlichen Gliomzellpopulationen. Sie unterstreicht die Notwendigkeit, die inhärenten Komplexitäten von Gliomen bei der Entwicklung wirksamer therapeutischer Strategien zu berücksichtigen. Die Ergebnisse liefern wertvolle Einblicke für die Entwicklung alternativer Behandlungen und Strategien zur Überwindung der TMZ-Resistenz bei IDH1-mutierten Gliomen.

List of Figures

List of tables

Abbreviations

AA – Amino acids
ACT – Actin
CGGA - Chinese Glioma Genome Atlas
CCNU – lomustine
PCV - vincristine
DAC -Decitabine
DMA - Droplet Microarray
DMSO - Dimethyl sulfoxide
2-HG - 2-Hydroxyglutarate
2-DG - 2-Deoxy-D-glucose
DNMT - DNA methyltransferase
GAPDH - Glyceraldehyde 3-phosphate dehydrogenase
GCMS - Gas Chromatography-Mass Spectrometry
GLASS - The Glioma Longitudinal AnalySiS
HiSeq - High-throughput DNA sequencing
LGGs - Lower-grade gliomas
IDH - Isocitrate dehydrogenase
IHA - Immortalized human astrocytes
FA – Fatty acid
FDA - U.S. Food and Drug Administration
ICER - incremental cost-effectiveness ratio
IPA - Ingenuity pathway analysis
MGMT - O6-methylguanine-DNA methyltransferase,
MMR – Mismatch repair
MS - Mass spectrometry
MSMS - Tandem Mass Spectrometry
MTT - Thiazolyl Blue Tetrazolium Bromide
Mut - mutant or mutation
PTX - Paclitaxel
PDTs - patient derived tumorspheres
QALYs - quality-adjusted life years
Ssd – Saikosaponin D
TCA - Tricarboxylic Acid Cycle
TCGA - The Cancer Genome Atlas
TMZ-R – Temozolomide resistance

VP – Verteporfin

WT- Wild type

YAP1 - Yes Associated Protein 1

NUPs - nucleoporin proteins

TP53 - Tumor Protein 53

1 Materials and Methods

1.1 Materials

1.1.1 Cell lines

The patient-derived tumorspheres were obtained as follows: TS603 from Memorial Sloan Kettering Cancer Center; NCH612 (oligodendroglioma) and NCH1681 (astrocytoma) from Heidelberg University Hospital; SU-AO3 (oligodendroglioma) cells were kindly provided by Dr. Michelle Monje (Stanford University).

Immortalized human astrocytes (IHAs) and isogenic cells expressing mutant IDH1 (R132H), wild-type IDH1, or neither have been well-characterized and utilized in our previous studiesto investigate the role of IDH1 in hypermethylation [1].

1.1.2 Cell culture media and supplements

Patient-derived IDH mutant glioma lines TS603, NCH1681, NCH612, SU-AO3 were maintained in Neurocult Basal Medium with proliferation supplements (Stemcell, Cat. # 05751), 20 ng/ml EGF (Stemcell, Cat. # 78006.2), 20 ng/ml basic-FGF (Stemcell, Cat. # 78003.2) and 2 µg/ml Heparin (StemCell, Cat. # 07980).

HEK293TN and IHAs were maintained in DMEM-high glucose (Sigma, D5796) supplemented with 10% fetal bovine serum (Gibco, A476680).

1.1.3 Drugs

Auranofin (Selleck, S4307-5mg)
Berberine Chloride (Selleck, S2271-10mg)
Decitabine (Sigma, A3656)
2-DG (2-deoxy-D-glucose) (Sigma, D8375)
Epirubicin hydrochloride (Merck, E9406-5mg)
Harringtonin (SCBT, sc-204771-5mg)
Homoharringtonine (SCBT, sc-202652-1mg)
Mildronate (Selleck, S4130)
Paclitaxel (Sigma, T7191-1mg)
Pyrvinium (Selleck, s5816-5mg)

RITA (Cayman Chemical,10006426)
Saikosaporin D (Selleck, S5454-1mg)
Temozolomide (Sigma, T2577-25mg)
Triptonide (SCBT, sc-200122-1mg)
Verteporfin (Sigma, SML0534-5mg)

1.1.4 Bacteria

Stable 3 (Thermo Fisher, C7381201)

1.1.5 Plasmids

shYAP1 #1(Addgene #42540)
shYAP1 #2 (Addgene #42541)
pLKO.1 puro (Addgene #8453)
pCMV-VSV-G (Addgene #8454)
psPAX2 (Addgene #12260)

1.1.7 Antibodies

anti- glyceraldehyde 3-phosphate dehydrogenase (GAPDH) (Cell Signaling, #2118)
anti-beta actin (ACTB) (Cell Signaling, #4967)
anti–IDH1 R132H (Dianova, #DIA-H09)
anti-ACTB (Sigma, #A3854)
Alexa Fluor® 647 anti-Nuclear Pore Complex Proteins Antibody (Biolegend, #682203)

1.1.8 Buffers and solutions

SDS Gel 10%:
Stacking gel, 10 mL (4 gels): 6,8 mL H_2O, 1,7 mL acrylamide 30%, 1,25 mL Tris 1 M pH 6,8, 100 µL SDS 10 %, 100 µL APS,10 µL TEMED;
Separating gel, 40 mL (4 gels): 19,8 mL H2O, 16,7 mLacrylamide 30 %, 1,5 mL Tris 1 M pH 8,8, 500 µL SDS 10 %,500 µL APS, 20 µL TEMED

SDS Page running Buffer 10 x: 60,6 g TRIS, 288,2 g Glycin, 20 g SDS, Volume: 2 L, fill up with H_2O, dilute 1:10 for 1 x concentration

Transfer Buffer (Western Blot): 72 g TRIS, 345,6 g Glycine, Volume: 2 L, fill up with H_2O, dilute 1:10 in 20 % (v/v) Methanol and 80 % H_2O for 1 x concentration

Tris-buffered Saline (TBS) 20 x: 121 g TRIS, 175,2 g NaCl, Volume: 1 L, fill up with H_2O, pH 7,4, dilute 1:20 for 1 x concentration

Tris-buffered Saline-Tween (TBS-T): 500 mL 20 x TBS, 10 mL Tween 20, Volume: 10 L, fill up with H_2O

1.1.9 Kits

BCA Protein Assay (Thermo Fisher)
QIAprep Spin Miniprep Kit (Qiagen)
QIAprep Spin Maxiprep Kit (Qiagen)
CellTiter-Glo® 2.0 Cell Viability Assay (Promega, Cat. #G9241)

1.1.10 Equipment and devices

Cell culture hood (Thermo Fisher)
Cell incubator (Thermo Fisher)
Centrifuge (Thermo Fisher)
ChemiDoc XRS+ Gel Imaging System (Bio-Rad)
iBlot 2 Dry Blotting System (Thermo Fisher)
Infinite 200Pro microplate reader (Tecan)
Luna automated cell counter (Biocat)
Microplate reader infinite 200Pro (Tecan)
Microscope (Zeiss)
Mini-PROTEAN. Tetra electrophoresis wet blot system (Bio-Rad)
NanoDrop (Thermo Fisher)
Sonorex Digitec (Bandelin)
Tabletop centrifuge (Thermo Fisher)
Thermal cycler (Biometra)

1.1.11 Consumables

Cell culture flasks (25cm^2, 75 cm^2, 175 cm^2) (Greiner Bio-One GmbH)
Cell culture plates (6-, 12-, 24-, 96-well) (Greiner Bio-One GmbH)
Cell counting slides (Logos Biosystems)

Pipette filter tips (STARLAB)
Pipette tips (STARLAB)
PVDF membrane (Merck, Darmstadt, Germany)
Reaction tubes (1,5 mL, 2 mL) (Eppendorf AG)
Reaction tubes (15 mL, 50 mL) (Corning)
Reagent reservoirs (Corning)

1.2 Methods

1.2.1 Cell culture

The patient-derived IDH mutant glioma cell lines, including TS603, NCH1681, NCH612, and SU-AO3, were cultured in Neurocult Basal Medium supplemented with proliferation supplements (Stemcell, Cat. #05751), 20 ng/ml EGF (Stemcell, Cat. #78006.2), 20 ng/ml basic-FGF (Stemcell, Cat. #78003.2), and 2 µg/ml Heparin (StemCell, Cat. #07980) to maintain their growth and viability. On the other hand, HEK293TN and IHAs cell lines were cultured in DMEM-high glucose (Sigma, D5796) supplemented with 10% fetal bovine serum (Gibco, A476680) to support their growth and proliferation.1.2.2 Cell toxicity analysis.

1.2.2.1 MTT assay

For cell survival analysis, I seeded 800 – 5,000 cells in 100 µL of medium per well in a 96-well plate. To prevent evaporation of the inner wells and minimize edge effects, 100 µL of PBS was added to the edge wells. The following day, the drugs were diluted in 50 µL of medium at different concentrations and added to the corresponding wells. After 96 hours of drug treatment, 10 µL of 10 mg/mL MTT (Sigma, Cat. # M5655) was added to each well. Following an additional 2-hour incubation at 37°C in the dark, 100 µL of solvent (10% SDS in 0.01 M HCl) was added and protected from light. The color was measured the next day using a Microplate reader (infinite 200Pro) at a wavelength of 580 nm, with a plate background measurement at 670 nm. The MTT readings were adjusted by subtracting the background reading obtained from wells containing only medium without cells. To determine the viability percentage, the survival percentage of each treatment well was then normalized to that of the non-TMZ treated wells based on the adjusted reading.

1.2.2.2 CellTiter-Glo cell viability assay

It is performed according to the manufacturer's recommendations (Promega, Cat. #G9241). For simplicity, the procedure was similar to the MTT assay, involving cell seeding and drug treatment. I seeded 800 – 5,000 cells in 100 µL of medium per well in a 96-well plate. To minimize edge effects and prevent evaporation in the inner wells, 100 µL of PBS was added to the edge wells. On the following day, the drugs were diluted in 50 µL of medium at various concentrations and added to the corresponding wells. After 96 hours of drug treatment, the CellTiter-Glo reagent was prepared by equilibrating it to room temperature. We carefully added an equal volume of the reagent to each well containing cells, allowing for cell lysis and even distribution of the reagent throughout the well. The plate was then incubated at room temperature for approximately 10 minutes to ensure complete cell lysis and reaction of ATP with the luciferase-luciferin system in the reagent. Following the incubation period, the luminescent signal was measured using a Microplate reader (infinite 200Pro) to detect luminescence. By comparing the luminescence readings between different samples or treatments, the relative cell viability was determined.

1.2.2.3 Soft agar anchorage-independent growth assay

To perform the anchorage-independent cell survival assay, I seeded a range of 100,000 to 150,000 cells in 0.4% soft agar (Lonza, Cat. # 50101) between 0.6% (top) and 0.8% (bottom) agar in 6-well plates. After two weeks of growth with fresh medium, the respective media were supplemented with drugs or control for a specific treatment duration. Following an additional 4 weeks of growth in fresh medium, the cells were stained with 0.005% crystal violet (Sigma, SML0534) and imaged using the Bio-Rad ChemiDoc XRS+ imaging system. The colonies were manually counted or quantified using ImageJ software. The acquired images were analyzed using ImageJ software, applying the same threshold for all colonies and excluding background noise, while restricting particle size to a range of 100-200.

For the soft-agar assay assessing the response to TMZ, I seeded 10,000 cells from TS603 and NCH1681, as well as 15,000 cells of SU-AO3, in a 12-well plate. After one week of cell growth, the media were refreshed daily with either 100 µM TMZ or 0.1% DMSO (control) for continuous treatment over 4 days. Images were captured following staining with 0.005% crystal violet one month later. Colony numbers and sizes were compared between patient-derived tumors (PDTs). For the soft-agar assay evaluating the response to VP, I seeded 10,000 cells from TS603, SU-AO3, and NCH1861. The cells were treated with 1µM VP or 0.04% DMSO (control) for 1 hour.

1.2.3 Calculation of IC_{50} and IC_{10}

The IC_{50} values were determined using the GraphPad Prism software, utilizing the four-parameter variable slope equation derived from the dose-response curve to calculate the [inhibitor] vs. response relationship. Subsequently, the IC_{10} values were derived from the IC_{50} values, along with the hillslope, obtained from the official website of https://www.graphpad.com/quickcalcs/Ecanything1.cfm.

1.2.4 Western Blot

To extract proteins for western blotting, the following steps were performed to ensure successful protein harvesting: cells were pelleted by centrifugation at 900 rpm for 5 minutes, washed three times with cold PBS, and lysed using 120 µL (per 6-well plate) of M-PER™ Extraction reagents (ThermoFisher #78501) containing 1X Protease Inhibitor Cocktail (Roche, SKU11697498001). The lysates were sonicated for 2 minutes using a Sonorex Digitec (Bandelin), followed by incubation on ice for 30 minutes. Subsequently, the samples were centrifuged at 13,000 g for 15 minutes at 4 °C, and the supernatant was carefully collected in 1.5 mL microcentrifuge tubes. The protein concentration was determined using the BCA Protein Assay Kit following the manufacturer's instructions (ThermoFisher, #23225). For the western blotting procedure, 20 µg of protein was mixed with 4X Laemmli Buffer (BioRad, #1610747) supplemented with 10% β-mercaptoethanol (Sigma, #M6250) and boiled at 95 °C for 10 minutes. The protein samples were loaded onto 10% resolving and 5% stacking SDS-PAGE gels for electrophoresis. The separated proteins were transferred onto a 0.2 µM PVDF membrane (Bio-Rad) using either the Mini-PROTEAN Tetra electrophoresis wet blot system (Bio-Rad) for proteins with molecular weights (MW) > 100 kDa or iBlot2 for MWs < 100 kDa. Transfer efficiency was assessed by Coomassie dye (Thermo Fisher, #20279) gel staining and Ponceau Red (Thermo Fisher, #46430) membrane staining. Following Ponceau staining, the membrane was washed with TBST and blocked with 5% milk at 4°C for 1 hour. Primary antibodies were applied overnight at 4°C in 5% milk. Protein signals were detected using Pierce ECL Western Blotting Substrate (ThermoFisher, #32109) and the ChemiDoc MP Gel Imaging System (Bio-Rad). To probe the same membrane with additional antibodies, the membranes were stripped using Restore PLUS Western Blot Stripping Buffer (ThermoFisher, #46430) for 15 minutes, repeated twice. The membranes were then washed with TBST, re-blocked with 5% milk, and subsequently used for subsequent immunoprobing experiments.

1.2.5 RNA-seq

Cells were seeded in a concentration of 5 x 10^5 cells/well in 6-well dishes. Cells were harvested, centrifuged at 4°C and 900 rpm for 5 min. Supernatant was discarded and pellets

were washed once with PBS and centrifuged at 900 rpm for 5 min again. RNA was then extracted using the RNeasy RNA isolation kit (QIAGEN) according to manufacturer's protocol. Samples were stored at -80°C until submission to the DKFZ Genomics Core Facility.

1.2.6 Metabolic assay

For metabolome analysis of TS603, SU-A03, NCH1681, and NCH612 PDTs. For sample preparation, 300,000 cells were seeded in 60 mm x 15 mm plates and treated with either 400 µM TMZ or 0.4% DMSO control or no treatment for 24 and 96 hours. Additionally, the no treatment samples was used for measurement of the base levels of metabolites to eliminate the effect of DMSO.

To prepare the samples for metabolome analysis, spheroids were dissociated into single cells using accutase, and cell numbers were counted. The cells were then washed three times with cold PBS and frozen in dry ice before being stored at -80°C. The metabolome analysis was performed using both GCMS (Gas Chromatography-Mass Spectrometry) and MSMS (Tandem Mass Spectrometry) metabolic assays. To ensure accurate data analysis, the protein concentration of the same vial after the metabolic assay was measured for normalization of the final concentration of metabolites. The TCA cycle was analyzed for 12 chemicals, while 29 fatty acids and 23 amino acids were measured.

1.2.7 Preparation of 3D glioma spheroid array

To obtain a single-cell suspension, the cells were harvested and dissociated using Accutase® (BioLegend, Inc. 423201). DMA slides were acquired from Aquarray GmbH (catalog, IR0050241542, Eggenstein-Leopoldshafen, Germany). Each DMA slide contained 588 square hydrophilic spots measuring 1 mm2, with a unique barcode assigned to differentiate between slides. The spots on the DMA were coated with an anti-adherence rinsing solution (50 nL, catalog # 07010, STEMCELL Technologies Inc.) and carefully dried under sterile conditions. Subsequently, a universal liquid dispenser (I-DOT, Dispendix GmbH, Germany) was employed to dispense 200 nL of cell suspension (cell concentration: 1.5 × 106 mL-1) onto each spot of the DMA slide. The slide was immediately inverted and cultured in an incubator, utilizing the hanging drop method. To monitor the growth of tumorspheres, images of the spheroids were captured after 1, 3, 5, and 7 days of cultivation using a microscope (Keyence BZ-X800, Japan).

1.2.8 Mass spectrometry

Whole cell lysates from three replicates per condition (drugs and control) from $1x10^6$ cells were prepared. Proteomics were performed at the Mass Spectrometry Core Facility at the German Cancer Center (DKFZ).

Data analysis was performed using MaxQuant software with default settings. An organism-specific database extracted from Uniprot.org was used for identification, and identification FDR cutoffs were set at 0.01 for both peptide-level and protein-level identification. The match between runs (MBR) option was enabled to transfer peptide identifications across RAW files based on accurate retention time and m/z. LFQ quantification was carried out using the MaxLFQ algorithm, requiring a minimum of 2 quantified peptides per protein. Individual LFQ normalization was performed for each cell line. Additionally, iBAQ-values were generated via MaxQuant.

For statistical analysis, protein groups with valid LFQ- or iBAQ values in at least 70% of the samples in one of the conditions were considered. Variance stabilization normalization was applied to LFQ and iBAQ values of VP treatment. Missing LFQ- or iBAQ values that were completely absent in one condition were imputed with random values drawn from a downshifted and narrowed intensity distribution of the individual samples. For missing LFQ- or iBAQ values without complete absence in one condition, imputation was performed using the R package missForest. The statistical analysis of LFQ- or iBAQ values was conducted using the R-package "limma," and p-values were adjusted using the Benjamini-Hochberg method for multiple testing.

1.2.9 Immunofluorescence and microscopy

To perform immunofluorescent analysis, 12 mm coverslips were placed in 12-well dishes and coated with 10 µg mL-1 laminin (Sigma, L2020-1MG) overnight at 4°C. The following day, the laminin was removed, and the coverslips were washed three times with PBS. Then, 1x105 cells were seeded onto the coverslips and treated with 1 µM VP or 0.04% DMSO in triplicate for 3 hours. After removing the drug, the cells were washed with PBS and fixed with 4% PFA for 20 minutes at room temperature. The PFA was then removed, and the cells were washed twice with PBS. To permeabilize the cells, 0.1% Triton X-100 was applied for 15 minutes at room temperature, followed by three gentle washes with PBS. For observation of VP subcellular localization, one drop of anti-fade mounting medium containing DAPI (VECTASHIELD, H-1200-10) was dispensed onto a microscope slide. The coverslips were mounted with the cells facing towards the microscope slide. Image z-stacks were acquired using a Zeiss LSM710 Confocal microscope with a 63 x (oil) objective. The acquisition

included T-PMT (bright field), Alexa-405 (DAPI), and Alexa-633 (autofluorescence of VP) channels, and the process was controlled using ZEISS ZEN microscope software.

1.2.10 Viral transductions

YAP1 was knocked down in TS603 and NCH1681 tumorspheres by viral transduction using two shRNA plasmids (shYAP1 #1, Addgene #42540; shYAP1 #2, Addgene #42541), and scrambled control plasmid (pLKO.1 puro, Addgene #8453). For virus production, $2x10^5$ HEK293TN cells were seeded in 6-well plates, transfection mixtures (1 µg target Plasmid + 0.6 µg envelope plasmid (pCMV-VSV-G, Addgene #8454) + 0.6 µg packaging plasmid (psPAX2, Addgene #12260) + 6.6 µL FuGene (Promega, E2311) + OptiMEM media (Gibco, # 31985062) up to a total of 100 µL) were added the next day. Cell culture medium was changed after 24 hours and collected for harvesting at 48 and 72 hours after transfection and filtered through 0.45 µm filters. The filtered cell culture supernatant was mixed in 3:1 ratio to a lab-made filtered 4x virus precipitation buffer (40 g PEG 8000, 7 g NaCl, 10 mL PBS, final pH adjusted to 7.4 with 1 M HCl, filled up to 100 mL with distilled water) and incubated overnight at 4 °C. Next, the PEG/medium mix was centrifuged at 1600 x g at 4 °C for 45 min for virus collection. Supernatant was discarded, virus pellets were resuspended in 250 µL PBS and added to the NCH1681 and TS603 tumorspheres (Seeded with density of $3x10^5$ cells per 6 well-plate one day ahead of transduction) 100 µL a time, and another 100 µL after 24 hours. Transfection efficacy was checked 48 hours post-transfection by imaging with fluorescent microscope and counting the number of fluorescing cells. Stably transduced cells were selected with fresh complete medium containing 0.5-1 µg mL^{-1} puromycin every 3-4 days until drug-resistant colonies become visible (generally 7-14 days after selection). As selection control, parental cells were used. HEK293-TN, NCH1681 and TS603 were passaged at least 2 times and less than 10 times before transfection and after thawing from the liquid nitrogen stock.

1.2.11 High-throughput FDA compound screening on DMA

For high throughput screening, the DMA spots were pre-printed with different drugs. The FDA-approved drug library was obtained from Selleck Chemicals LLC and stored according to supplier guidelines (L1300-Z351463, https://www.selleckchem.com/screening/fda-approved-drug-library.html). A non-contact dispensing system (sciFLEXARRAYER, SCIENION AG. Germany) was utilized to print 2 nL of the drug solution in DMSO into each spot. The final drug concentration in droplets containing cells was 5 µM, with 5 replicates for each drug. A total of 2208 drugs were printed on 24 DMA slides, excluding the outer rows to minimize edge effects. Each slide consisted of 92 drugs and a DMSO control group.

Subsequently, 300 cells in 200 nL of medium were seeded for each spot, using two tumorspheres (NCH1681, TS603). The slides were incubated for 3 days using the hanging drop method. After incubation, the cells were stained with Calcein AM (1/2000) and PI (1/2000) for 20 minutes. Imaging of the DMA slide was performed using an automated screening microscope, Leica Thunder 3D Imager (Leica Microsystems, Germany).

For the analysis of screening results, the exported TIF format images were processed. Each spot had two channels: green for live cells and red for dead cells. To accurately segment the fluorescence images, a deep learning system was developed. Pre-labelling was applied to optimize image processing, enabling the distinction between non-cellular fluorescent signals and reducing background interference. Based on this, the areas of spheroids in the green and red fluorescent channels were accurately determined, representing the live and dead portions of the spheroids, respectively. The green area was designated as Area (Calcein), and the red area as Area (PI). The viability of each spheroid was estimated as Area (Calcein) / [Area (Calcein) + Area (PI)].

1.2.11 Statistical analysis

Student's t test and 1- or 2-way ANOVA were used, as appropriate, to calculate significance (*P < .05, **P < .01, ***P < .001).

1.2.12 Software and databases

1.1.12.1 Software

GraphPad Prism (GraphPad Software Inc., La Jolla, CA, USA)
FIJI: http://fiji.sc/
ImageJ: http://imagej.nih.gov./ij/
Ingenuity Pathway Analysis (Qiagen)
Microsoft Office (Microsoft Corporation, Redmond, WA, USA)
Inkscape: https://inkscape.org
R: http://r-statistics.com
ChatGPT: https://chat.openai.com
Combenefit: https://sourceforge.net/projects/combenefit/
SRplot: http://www.bioinformatics.com.cn
ClustVis: https://biit.cs.ut.ee/clustvis/
Venny: https://bioinfogp.cnb.csic.es/tools/venny/index2.0.2.html
SynergyFinder: https://synergyfinder.fimm.fi

BioRender: https://www.biorender.com

1.1.12.2 Database

PubMed: http://www.ncbi.nlm.nih.gov/pubmed
Chinese Glioma Genome Atlas (CGGA) Database: http://www.cgga.org.cn
The Cancer Genome Atlas (TCGA) Database: http://cancergenome.nih.gov
The Human Protein Atlas: https://www.proteinatlas.org
String: https://string-db.org/cgi
Metascape: https://metascape.org
cBioPortal: https://www.cbioportal.org
GlioVis: http://gliovis.bioinfo.cnio.es
Enrichr: https://maayanlab.cloud/Enrichr/
Reactome: https://reactome.org
Drugbank: https://go.drugbank.com

2 Introduction

2.1 Adult-type diffuse glioma

Gliomas are the most common primary malignant tumor in the central nervous system (CNS), representing approximately 24% of all primary brain and other CNS tumors (over 100 distinct types) and 80.9% of malignant ones (Figure 1A) [2, 3]. Despite significant efforts to understand their underlying causes [4, 5], there is no clear genetic or environmental factor that predisposes to gliomas. The symptoms of glioma are mainly due to the pressure on the brain, leading to headaches, blurred vision, nausea and vomiting, seizures, and balance problems.

The standard diagnostic tools for glioma include MRI (magnetic resonance imaging), PET (positron emission tomography), CT (computerized tomography) scans to determine the size and location of the brain tumors, and stereotactic needle/surgery biopsy to examine the tissue (Figure 1C).

The latest edition of the WHO Classification of Tumors of the Central Nervous System (CNS), published in 2021, WHO CNS5 , has simplified the classification of adult-type diffuse gliomas into three major types: astrocytoma, IDH-mutant; oligodendroglioma, IDH-mutant, 1p/19q-codeleted; and glioblastoma, IDH-wildtype [6]. Patient tumor data from The Cancer Genome Atlas (TCGA) [7] and the Chinese Glioma Genome Atlas (CGGA) [8] suggest that glioblastoma, IDH-wildtype accounts for approximately 53% of glioma cases, astrocytoma, IDH-mutant accounts for 18.8 %, and oligodendroglioma, IDH-mutant, 1p/19q-codeleted accounts for 28.2 % of cases (Figure 1B).

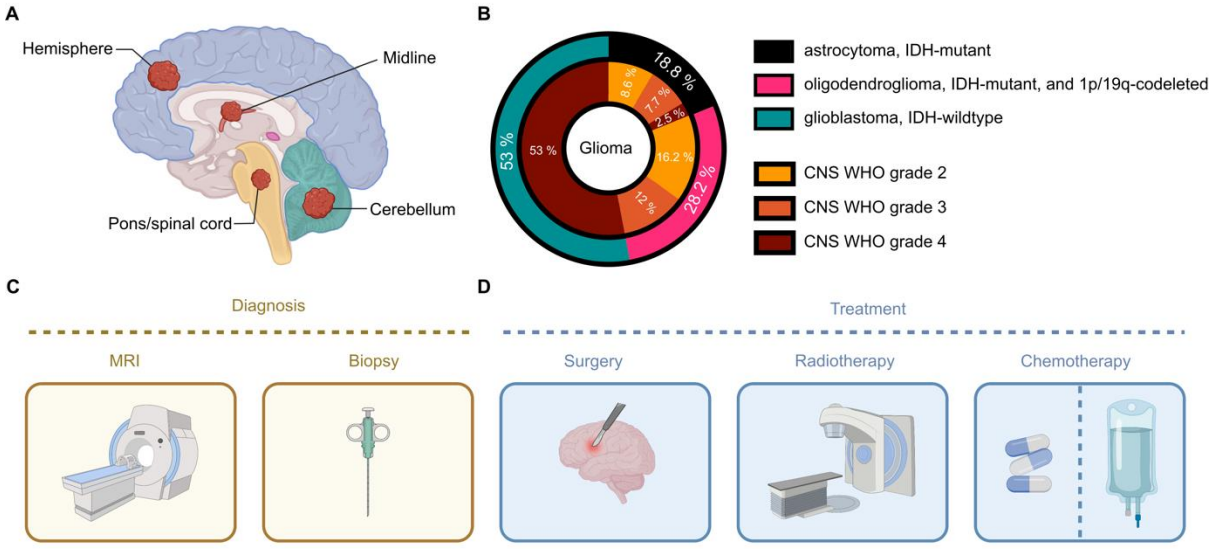

Figure 1. Diagnosis, classification, and treatment of gliomas.
(A) Location of gliomas in the brain. (B) Incidence of adult-type diffuse glioma subtypes classified according to the fifth edition of the WHO classification, based on data from CGGA. (C) Diagnostic modalities for adult diffuse glioma. (D) Treatment options for adult diffuse glioma. Image was created with BioRender.com.

Tumor grade is assigned to each subtype based on histopathology. CNS WHO grade is assigned to each tumor subtype, with astrocytoma, IDH-mutant having grades 2, 3, and 4; oligodendroglioma, IDH-mutant, and 1p/19q-codeleted having grades 2 and 3; and glioblastoma, IDH-wildtype, having only grade 4 [6, 9] (Figure 1B). CNS WHO grade 3 tumors often display increased cell density and greater nuclear atypia, and multinucleated tumor cells and abnormal mitoses may be seen. CNS WHO grade 4 tumors histologically manifest necrosis and/or microvascular proliferation in addition to the features of grade 3 lesions [10]. Grade 2 and 3 tumors tend to progress to a higher grade, and grade 4 is the most malignant grade, with a median survival period of less than two years. Based on CGGA data, among astrocytoma, IDH-mutant cases, 45.5% are grade 2, 41.0% are grade 3, and 13.46% are grade 4. Among oligodendroglioma, IDH-mutant, 1p/19q-codeletion cases, 57.5% are grade 2, and 42.5% are grade 3 (Figure 1B).

Different glioma subtypes have different genetic/epigenetic alterations. For example, key diagnostic genes and altered molecules in astrocytoma include IDH1, IDH2, ATRX,TP53, CDK2A/B; in oligodendroglioma: IDH1, IDH2, 1p/19q,TERT promoter, CIC, FUBP1, NOTCH1; and in glioblastoma, IDH-wildtype, TERT promoter, chromosomes 7/10 copy number alterations, and EGFR amplification [11]. These molecular changes also play a role in determining response to therapy [12]. For instance, 1p/19q co-deletion is associated with

response to treatment with alkylating agents [13]. As chemotherapy is carried out after surgical operation, rapid molecular diagnosis is necessary in order to provide prognostic evidence and more precise targeted therapy [14].

The treatment options for gliomas include surgery, RT (radiation therapy), chemotherapy, chemoradiation (combination of radiation and chemotherapy) [9, 15]. Despite these treatment options, gliomas are highly infiltrative and resistant to therapy, rendering them largely incurable (Figure 1D).

2.2 IDH mutation

In gliomas, IDH (isocitrate dehydrogenase) mutation was first reported in 2008 through whole-exome sequencing of 22 glioblastoma cases [16]. A year later, it was discovered that IDH1 mutation resulted in overproduction of the oncometabolite D-2-hydroxyglutarate (2HG) [17]. Since then, numerous studies have shed light on the biological impact of IDH mutations and their potential role in oncogenesis [18-20].

IDH1 and IDH2 (referred to IDH) are metabolic enzymes located in the cytosol and mitochondria, respectively [21]. IDH mutations typically result in single amino acid substitutions, with the arginine to histidine substitution at position 132 (R132H) in the catalytic site of IDH1 being affected in about 90% of cases [22].

IDH mutations are heterozygous and require wildtype protein for functional activity [23]. Patients with IDH-mutated gliomas have a more favorable prognosis than those with IDH-wildtype tumors [24]. The loss of IDH mutation contributes to an aggressive tumor phenotype, while IDH mutations are typically maintained in glioma recurrences. IDH mutations may have different roles at different stages of tumor development, with evidence suggesting that they may be necessary for tumor initiation and positively selected in most tumors but may not be required for continued tumor maintenance and progression [1, 25]. So, the prospect of IDH-mutation as a therapeutic target in glioma remains under investigation with early clinical studies showing efficacy of mutant IDH inhibitors in non-contrast enhancing gliomas.

The precise mechanisms underlying the pathogenic role of IDH mutations in cancer remains unclear. Studies show that 2-HG generated by mutant IDH establishes distinctive patterns in cancer metabolic profiles and epigenetic programs (Figure 2) leading to a block in

differentiation. In normal physiology, IDH catalyzes the oxidative decarboxylation of isocitrate to α-ketoglutarate, reducing NADP+ to NADPH. However, IDH mutations lead to neomorphic enzymatic activity that converts alpha-ketoglutarate (α-KG) to 2HG, consuming NADPH and causing the accumulation of 2HG, which drains carbohydrates from the Krebs cycle [26]. Although alterations in central carbon metabolism, amino acid metabolism, lipid metabolism, and redox homeostasis have been observed, evidence suggests that these changes are context-dependent, and vary with cancer type and disease models [27].

α-KG is a molecule that serves as an intermediate in the Krebs cycle, a metabolic pathway that generates energy by breaking down carbohydrates, fats, and proteins in the presence of oxygen [28]. It is also involved in other metabolic processes such as the synthesis of amino acids and nucleotides [29]. In addition, α-KG can also serve as a co-substrate for a family of enzymes known as α-KG-dependent dioxygenases [17]. Elevated 2HG levels in IDH-mutant cells have been proposed to cause many of the observed metabolic changes, particularly via inhibition of these enzymes. As 2HG and α-KG are structurally similar, 2-HG acts as a competitive inhibitor of α-KG-dependent dioxygenases. α-KG-dependent dioxygenases are a family of 70 enzymes that require α-KG as a co-substrate to catalyze the hydroxylation of various substrates, including DNA, RNA, proteins, and small molecules [30]. Examples of include DNA and histone demethylases, as well as enzymes involved in the regulation of hypoxia-inducible factor (HIF) stability and activity [31, 32]. This inhibition leads to altered histone methylation [33] and DNA hypermethylation [1], associated with increased H3K27me3 (repressive histone H3 lysine 27 trimethylation) and decreased H3K4me3 (the activating histone H3 lysine 4 trimethylation) and decreased 5-hydroxylmethlcytosine (5hmC) [17]. Such epigenetic effect leads to blocking of cellular differentiation and other transformative effects [33].

IDH-mutant cancers consistently exhibit a hypermethylated state, with the glioma CpG island methylator phenotype (G-CIMP) being a distinct subset of glioma samples with this phenotype as revealed in an analysis of 272 samples from TCGA [34]. Patients carrying G-CIMP (G-CIMP+) tumors have shown a better prognosis than those not carrying that phenotype (G-CIMP−) [35]. G-CIMP+ tumors were closely related to IDH mutation and nearly all IDH-mutant gliomas were G-CIMP+ and had a favorable prognosis [36].

While overproduction of 2HG, hypermethylation, and blocked normal differentiation patterns are common biological effects of IDH mutations that occur independently of the cell or cancer type, variations exist in the effects on metabolism. These differences suggest that

IDH mutations have cancer-, tissue-, and differentiation state-dependent phenotypes. The effects of IDH mutations are likely to depend on the cell type and genetic context, and the overall prognostic and therapeutic implications of these mutations are also dependent on the tumor context.

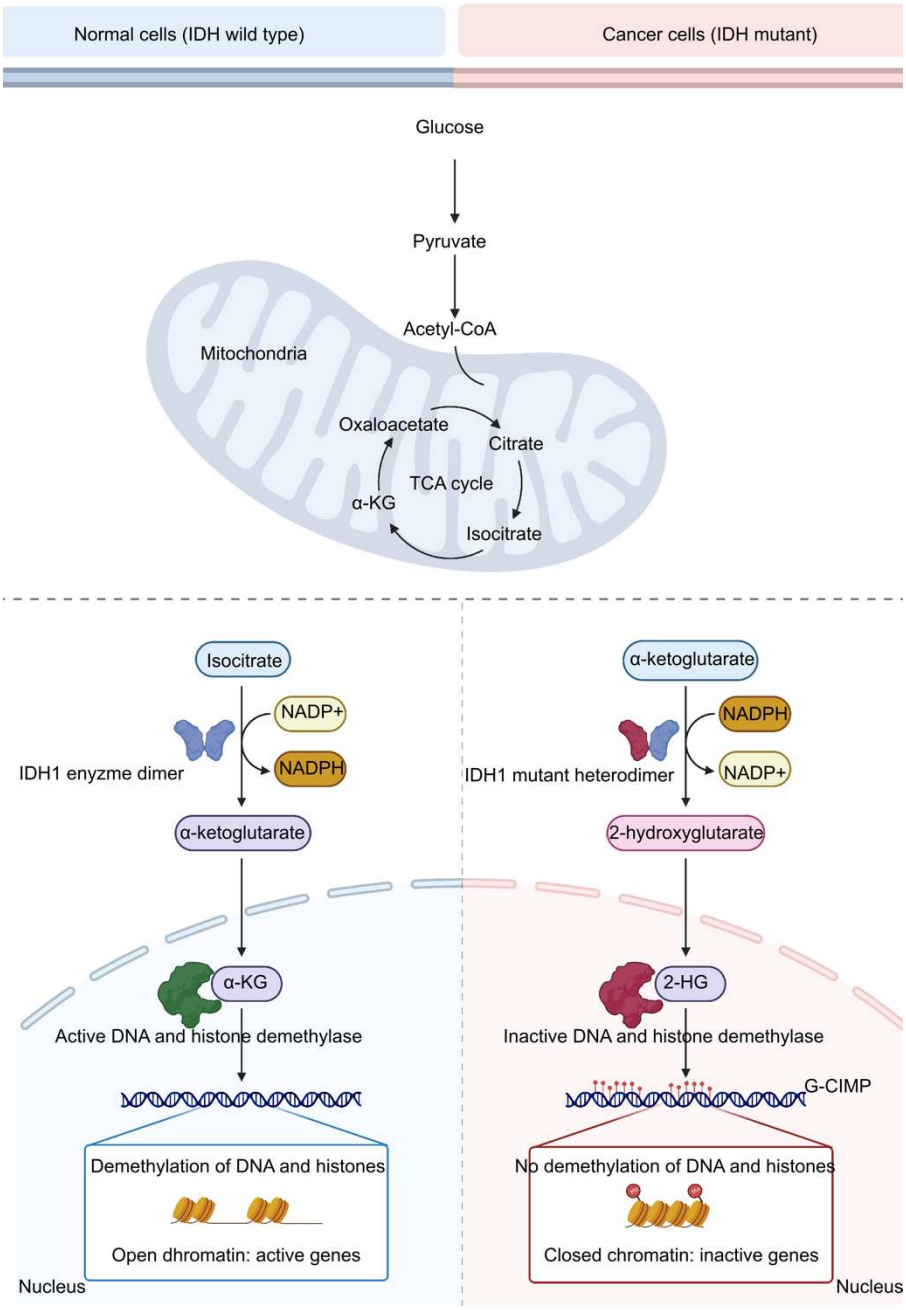

Figure 2. Epigenetic effect of Oncometabolite 2-Hydroxyglutarate.
The heterodimer mutation of IDH1 results in the excessive production of 2-HG, which leads to the inactivation of DNA and histone demethylase enzymes. Consequently, this causes chromatin to adopt a closed state, resulting in gene inactivation. Image was created with BioRender.com.

Orally administered Vorasidenib (AG-881) is a novel brain-penetrant dual inhibitor targeting mutant IDH1 and IDH2 enzymes. In an open-label, Phase I trial, Vorasidenib demonstrated favorable tolerability and preliminary antitumor activity in patients with recurrent or progressive non-enhancing IDH-mutant gliomas [37]. These findings suggest a potential benefit of incorporating mutant-IDH targeted therapy during the watch and wait period. Currently, Vorasidenib is being further evaluated in a Phase III study (NCT04164901) [37].

2.3 Clinical use and challenges of TMZ

2.3.1 Clinical use of TMZ

TMZ first received approval from the U.S. Food and Drug Administration (FDA) in 1999 for treating glioblastoma multiforme (GBM). However, its significant impact on the standard-of-care treatment for newly diagnosed GBM was not realized until 2005. This was when the influential EORTC 26981/22981-NCIC CE.3 trial, also known as the "Stupp protocol", demonstrated that adding TMZ chemotherapy to radiation therapy, instead of using radiation alone, greatly improved patient outcomes [38]. Since then, TMZ has been integral to the standard GBM regimen, typically used in conjunction with radiation therapy initially, followed by maintenance therapy solely with TMZ. An examination of data from the Surveillance, Epidemiology, and End Results (SEER) Program revealed an increase in survival rates for adult glioblastoma patients between the pre-TMZ period of 2000-2003 and the post-TMZ period of 2005-2008. Specifically, median survival times for all patients increased from 8.1 months to 9.7 months, a shift likely attributable to the introduction of TMZ [39].

The American Society of Clinical Oncology (ASCO) and the Society for Neuro-Oncology (SNO) conducted a systematic review in 2022, examining 59 randomized trials about treatment strategies for adult diffuse astrocytoma and oligodendroglioma tumors [15]. For newly diagnosed oligodendroglioma patients, grades 2 and 3, who are IDH-mutant and 1p19q codeleted, the recommendation is radiation therapy (RT) and PCV chemotherapy (procarbazine, lomustine, vincristine). TMZ may be an alternative for patients intolerant to PCV, although its first-line treatment efficacy is not firmly established.

For newly diagnosed astrocytoma patients, IDH-mutant, 1p19q non-codeleted, grade 2, the suggestion is RT and adjuvant chemotherapy (TMZ or PCV). Grade 3 patients should receive RT and adjuvant TMZ. Grade 4 patients should follow either grade 3 astrocytoma recommendations or those for glioblastoma, IDH-wildtype, grade 4. Newly diagnosed glioblastoma patients, IDH-wildtype, grade 4, should receive concurrent TMZ and RT,

followed by six months of adjuvant TMZ. Alternating electric field therapy is a consideration, while Bevacizumab is not advised. Hypofractionated RT plus TMZ is a suitable alternative for those where standard treatment may be excessively strenuous [9, 15].

TMZ is usually given in cycles involving daily doses for a set number of days, followed by a rest period. This rest period allows the body to recover and helps balance the medication's benefits with possible side effects. The cycle repeats for several weeks or months, depending on the treatment plan. Sometimes, it is taken on an empty stomach for better absorption. Typically, the drug is taken orally in capsule form, with dosages ranging from 150–200 mg/m^2/day for 5 days in a 28-day cycle, repeated for 6–12 cycles.

2.3.2 Chemical properties and pharmacokinetics of TMZ

TMZ is an oral chemotherapy medication available in capsule form that is consumed with water. Its chemical name is 3,4-dihydro-3-methyl-4-oxoimidazo[5,1-d]-as-tetrazine-8-carboxamide, appearing as a white to light tan or pink powder. The molecule, with a molecular formula of $C_6H_6N_6O_2$ and a molecular weight of 194.15, is stable at acidic pH (< 5) but labile at pH >7.

TMZ is a prodrug, meaning it is not directly active but is rapidly converted at physiological pH to the reactive compound 5-(3-methyltriazen-1-yl)-imidazole-4-carboxamide (MTIC) [40]. This conversion process is spontaneous and does not require hepatic activation. Further hydrolysis of MTIC results in two additional compounds: 5-amino-imidazole-4-carboxamide (AIC), an intermediate in purine and nucleic acid biosynthesis, and methylhydrazine, which is thought to be the active alkylating agent. The cytotoxic effect of MTIC is mainly attributed to its ability to alkylate DNA, specifically at the O^6 and N^7 positions of guanine [41].

According to the information from drug bank TMZ is quickly absorbed from the gut, with nearly 100% bioavailability. It easily crosses the blood-brain barrier, with cerebrospinal fluid (CSF) concentrations reaching approximately 20-30% of blood plasma concentrations. The elimination half-life of TMZ is around 1.8 hours. After oral administration, peak plasma concentrations typically occur within 30 to 90 minutes.

TMZ exhibits linear kinetics within the therapeutic dose range of 75 mg/m^2/day to 250 mg/m^2/day. Its absorption is influenced by food intake; for instance, when administered after a high-fat meal, the mean maximum concentration (C_{max}) and area under the curve (AUC) decreased by 32% and 9%, respectively. In terms of distribution, about 15% of TMZ or its

metabolites bind to proteins in the blood plasma. Bound drug molecules are generally inactive and less available for interaction with target sites. About 38% of an administered TMZ dose is excreted over seven days, primarily through urine (38%) and a minor amount through feces (0.8%).

The pharmacokinetics of TMZ in the brain or CSF has been explored in several studies. A 2004 study confirmed a CSF/plasma ratio of 20% [42]. While a pilot study using Intracerebral Microdialysis (ICMD) suggested a delay in peak TMZ concentrations in the brain, implying potential benefits of administering TMZ 2-3 hours prior to radiation treatment [43]. Furthermore, a study utilizing human positron emission tomography (PET) data predicted that peak TMZ concentrations ranged from 2.9 to 6.7 μM in human glioma tumors and from 1.8 to 3.7 μM in normal brain tissues. This study also suggested higher TMZ exposure in brain tumors compared to normal brain tissue, possibly due to the breakdown of the blood-brain barrier and increased intratumoral angiogenesis [44] .

2.3.3 Mechanism of toxicity and resistance to TMZ

The primary toxicity of TMZ arises from methylation at the O6 positions of guanine (O^6-meG) [41]. During replication, DNA polymerase places a thymine (T) opposite O^6-meG, leading to an O^6-meG: T mismatch. If the mismatch repair systems (MMR) attempt to repair this, DNA polymerase reinserts a T opposite O^6-meG, thereby triggering another round of MMR. This process results in repeated repair attempts for the same base T [45]. As a consequence, single-strand DNA (ssDNA) gaps accumulate, prompting a succession of increasingly extensive DNA insertions and excisions. This process eventually gives rise to double-strand breaks (DSBs) in subsequent replication rounds and triggers cell cycle arrest in the G2/M phase, as well as inducing apoptosis and autophagy [46] (Figure 3).

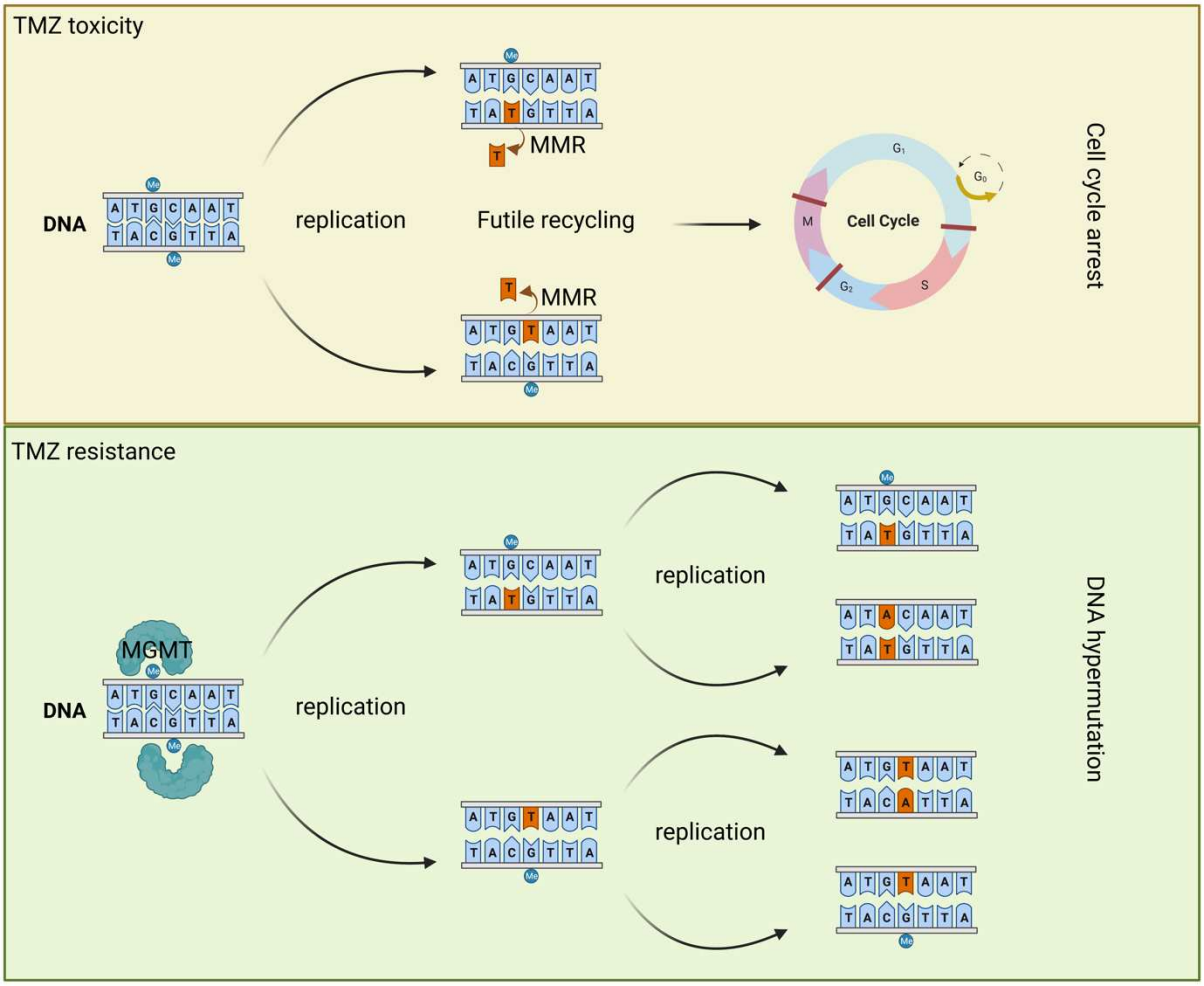

Figure 3. Toxicity and resistance of TMZ.
The mismatch between thymine (T) and O6-methylguanine (O6-meG) triggers the futile recycling of mismatch repair proteins, resulting in cell cycle arrest and cell death. While O6-meG lesions can be directly repaired by the enzyme O6-methylguanine DNA methyltransferase (MGMT), a defect in the recognition by the mismatch repair (MMR) system can lead to the persistence of the T:G mismatch, ultimately causing subsequent DNA hypermutation. Image was created with BioRender.com.

In most MGMT-deficient GBM patients, the initial response to TMZ is eventually followed by tumor recurrence coincident with mutations in genes that encode MMR proteins and the development of a hypermutator phenotype. However, O^6-meG lesions can be directly repaired by the enzyme O^6-methylguanine DNA methyltransferase (MGMT) [47]. This enzyme removes the lesions through a process of covalent transfer, effectively repairing the alteration before replication takes place [48]. The methylation of the MGMT promoter is a predictive biomarker for TMZ response in glioblastoma multiforme (GBM) [49]. Generally, the repair of O^6-meG is dependent on the quantity of MGMT molecules per cell and the rate of MGMT regeneration. Therefore, the cytotoxicity induced by TMZ relies on low levels of MGMT and a fully functional MMR pathway [50].

Patients with a hypomethylated MGMT promoter exhibit increased levels of MGMT protein and greater resistance to alkylating agents like TMZ. MGMT methylation status remains a valuable predictor of survival in GBM. Even though there is relevant association on mismatch repair (MMR) protein as a novel biomarker due to its high relevant association with tumor mutation burden, it appears the MMT status in recurrent GBM is not a prognostic marker [51]. It is still controversial if MMR can be used as a prognostic marker. The expression of the MGMT gene is repressed by DNA methylation of its promoter. This occurs in ~50% of GBMs and >70% of lower-grade gliomas (grades II and III), and less frequently in other cancers [52].

Therapy resistance in diffuse glioma remains poorly understood, but recent studies have aimed to shed light on treatment-induced plasticity and temporal heterogeneity by examining genomic changes in primary and recurrent tumors after TMZ treatment.
In a 2014 study, Johnson et al. sequenced the exomes of 23 initial low-grade IDH mutant gliomas and recurrent tumors from the same patients. They found that in 43% of cases, at least half of the mutations in the initial tumor were undetected at recurrence. Furthermore, 6 out of 10 patients treated with TMZ at recurrence showed hypermutation [53]. The Glass (The Glioma Longitudinal AnalySiS) consortium conducted a study in 2019 involving a database of initial and recurrent samples from 222 patients [54]. Among this cohort, 35 patients exhibited treatment-related hypermutation at recurrence, and 70% of the patients had an increased mutational burden after recurrence. However, the study revealed that driver genes detected in the initial disease were retained at recurrence, with little evidence of recurrence-specific gene alterations. Notably, within IDH-mutant tumors without 1p/19q deletion, 47% of patients had treatment-associated hypermutation, indicating a potential dependency of treatment-related mutations on IDH mutation status. This led the authors to conclude that the strongest selective pressures occur early in glioma development, and current therapies shape this evolution in a stochastic manner.

Further studies have explored the mechanisms underlying the hypermutation phenotype associated with TMZ. In a 2020 study with a large cohort of 10,294 gliomas, 558 cases were identified with hypermutation signatures primarily associated with mismatch repair (MMR) defects induced by TMZ. *In vitro* experiments using glioma cells with MMR defects exposed to TMZ confirmed the development of a treatment-induced hypermutated signature, suggesting that TMZ selects for subclones deficient in MMR and thus resistant to it [55].

2.3.4 Cost-effectiveness of TMZ

TMZ, marketed under the brand name Temodar, represents a considerable financial burden in the management of brain tumors, with costs often surpassing $100,000 per patient due to intense resource utilization [56]. The cost-effectiveness of TMZ is generally evaluated using quality-adjusted life years (QALYs) and the incremental cost-effectiveness ratio (ICER).

In studies conducted in 2021, the cost-effectiveness of a short-course radiation in conjunction with TMZ for the treatment of newly diagnosed glioblastoma multiforme (GBM) was examined among elderly patients in both China and the USA. The findings revealed that for US patients with methylated tumors, the treatment was cost-effective, with an ICER of $89,358.51, below the willingness-to-pay (WTP) threshold of $100,000 per QALY gained. However, for the treatment to be cost-effective among Chinese patients with methylated tumor status, the cost of TMZ would need to fall below ¥120 per 20 mg [57].

In general, the cost of TMZ (Temodar®) treatment in the US ranges between $1,600 and $4,600 per month. The total cost of adjuvant treatment can reach up to $9,000 per month, excluding surgery costs [58]. Despite these high costs, TMZ remains a critical treatment option due to its significant impact on both the quality and quantity of life for patients, as assessed through the QALY framework.

2.4 Combination therapy and drug synergy

Treating adult diffuse gliomas presents a significant challenge due to the tendency of these cells to infiltrate surrounding tissue, which often makes surgical intervention ineffective. In the past decade, whole genome sequencing and other ''omic'' technologies have pinpointed pathogenic driver mutations that are crucial for tumor cell survival [59, 60]. Despite these advancements, the remarkable intratumor genetic diversity uncovered by deep sequencing elucidates why both de novo and acquired resistance occur with molecularly targeted drugs and cytotoxic chemotherapy, thereby limiting their effectiveness [61-63].

It is increasingly evident that single-agent targeted therapy may not yield substantial clinical benefits [64]. Implementing combination strategies could enhance the likelihood of successful therapeutic outcomes (Figure 4). The logic behind combination cytotoxic chemotherapy has been to concurrently administer drugs that operate through distinct molecular mechanisms [65]. This approach aims to amplify tumor cell destruction, decrease the chance of drug resistance, and minimize overlapping toxicity [59]. Presently, cancer drug discovery and development are intensely centered on exploiting pathogenic oncogene and non-oncogene addiction, synthetic lethality, and other susceptibilities.

One significant obstacle in the development of combination drug therapy is the complexity of mathematical combinations [66]. Evaluating two-way and three-way combinations with varying dosages and timings can quickly become unfeasibly expensive, especially when considering the multitude of drug and/or target combinations in animal models, let alone in clinical settings. Another challenge lies in the translation of data from preclinical to clinical stages. A recent report in oncology revealed that published data completely aligned with in-house findings in only approximately 20-25% of the projects. Remarkably, nearly two-thirds of the projects encountered discrepancies between published and in-house data, leading to the termination of these projects [67].

One of the key challenges in combination drug therapy is understanding the interactions and predicting the outcomes of various drug combinations. To address this, computational methods are increasingly being used to explain and predict therapeutic resistance and potential drug combinations, with a particular focus on exploiting high-throughput experimental data.

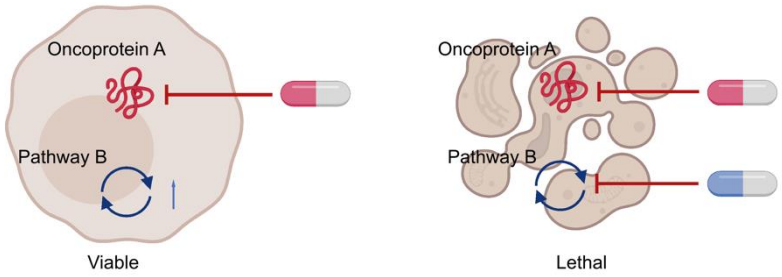

Figure 4. Drug specific synthetic lethality.
Inhibition of oncoprotein A triggers pathway B activation. Inhibition of oncoprotein A and pathway B is lethal for cancer cells. Image was created with BioRender.com.

Historically, models such as the Loewe additivity model, the Goldie-Coldman hypothesis, and the Chou and Talalay's combination index have been used to predict the effects of combined drugs and explain the emergence of drug resistance [68-71]. These models incorporate principles of mass action law and enzyme kinetics, allowing for a prediction of the degree of inhibition by combined drugs.

In 2012, an unbiased computational approach was utilized to develop an algorithm predicting effective drug synergies. This approach analyzed various drug features, such as molecular targets, pharmacological data, and toxicity profiles, and identified 16 high-scoring drug combinations using 184 pairwise combinations of US Food and Drug Administration (FDA)-

approved drugs for potential clinical use [72]. However, the development of successful drug combinations still faces hurdles, such as additive toxicity. This is particularly true when combining multiple molecularly targeted agents, which can result in both on-target and off-target toxicity [73, 74]. To manage these issues, careful target engagement, pathway biomarker evaluation, and adjustments to administration schedules are needed.

Further recommendations have been proposed regarding the combination of molecularly targeted agents with chemotherapy [75]. Molecularly targeted agents, also known as "targeted therapies," are drugs or substances designed to obstruct cancer growth by interacting with specific molecules involved in cancer development, progression, and spread. Conversely, chemotherapy primarily disrupts a cell's capacity to divide or reproduce. While this approach effectively eliminates cancer cells, it can also damage healthy cells that rapidly divide, leading to potential side effects (Figure 4).

Nevertheless, combining these two treatment strategies has proven advantageous in numerous instances [76]. For instance, targeted therapies can occasionally increase the susceptibility of cancer cells to chemotherapy or slow cancer growth, thereby enhancing the potential effectiveness of chemotherapy.

A search on ClinicalTrials.gov using the key terms 'glioma' and 'combination therapy' yielded 899 studies globally. Narrowing it down to clinical trials with results, there were 171 studies primarily involving all types of glioma. A specific search for low-grade gliomas revealed one clinical trial (NCT02023905), which investigated the effects of everolimus (RAD001, or Afinitor®), an mTOR inhibitor, alone or in combination with TMZ in adult low-grade glioma. However, this study was terminated due to sponsor decisions.

When I refined the search terms to include gliomas with IDH mutation and combination therapy with results, only one trial appeared (NCT03684811). This Phase 1/2 study evaluated the safety, efficacy, pharmacokinetics (PK), and pharmacodynamics (PD) of FT-2102 (olutasidenib), a potent, orally active, brain-penetrant and selective inhibitor of mutant Isocitrate dehydrogenase 1 (IDH1). The study explored olutasidenib as a single agent and in combination with other anti-cancer drugs, including the epigenetic drug Azacytidine and PD-1 monoclonal antibody Nivolumab or chemotherapy drugs Gemcitabine (an antimetabolite), and cisplatin, in patients with advanced solid tumors and gliomas. FT-2102 was well-tolerated as a single agent; however, the combined results have not yet been reported [77]. Searching for combination therapy with TMZ across all tumor types revealed 554 clinical trials globally and 344 specifically in glioma. Only 2 of these were in IDH mutant gliomas:

'BGB-290 and TMZ in treating patients with recurrent gliomas With IDH1/2 Mutations' (NCT03914742) and 'PARP Inhibitor -290 and TMZ in treating (IDH)1/2-mutant grade I-IV gliomas' (PNOC017).

In summary, despite the extensive search for synergistic effects targeting different facets of cancer metabolism and epigenetics, the number of combination therapy trials for IDH mutant gliomas remains limited.

2.5 Drug repurposing

Drug repurposing, also known as drug repositioning or drug reprofiling, is the process of identifying new therapeutic uses for existing drugs that are already approved for other indications [78].

The traditional drug development process is characterized by its lengthy duration, high costs, and inherent risks. On average, it takes approximately 13 years of extensive research and an investment of around US$1.8 billion to successfully bring a single drug from the laboratory to the patient's bedside [79]. This process involves various stages, including design, production, and comprehensive evaluations of the drug's efficacy, toxicity, pharmacokinetics, and pharmacodynamics through cell- and animal-based studies (Figure 5).

The subsequent step in drug development entails conducting clinical trials to assess the safety and efficacy of the drug in human subjects [80]. These trials typically consist of four phases. Phase I clinical trials involve administering the new drug to a small group of individuals (usually between 20 and 80) to evaluate its safety, determine an appropriate dosage range, and identify any potential side effects. Phase II clinical trials are conducted on a larger cohort, usually comprising several hundred participants, to assess the drug's efficacy and further evaluate its safety. Following promising results, phase III studies involve testing the drug's effectiveness in large groups of trial participants, ranging from several hundred to several thousand individuals. These studies compare the new intervention with existing standard treatments or experimental interventions, while also monitoring adverse effects and gathering additional safety information to ensure the drug can be used safely. Phase IV studies occur after the drug has received regulatory approval and entered the market. These studies aim to monitor the drug's effectiveness in the general population and

collect data on any adverse effects that may arise from its widespread use over longer periods of time.

In general, if a drug demonstrates efficacy in phase III trials, it is likely to receive approval from regulatory bodies such as the FDA. However, it is important to note that the journey from drug development to approval is arduous. Only a minuscule fraction, approximately one out of every 5,000 to 10,000 prospective anticancer agents, ultimately receives FDA approval. Additionally, a mere 5% of oncology drugs that enter phase I clinical trials successfully make it to market [80].

According to Statista, the number of FDA approvals for new drugs per year has experienced a decline over the past three decades, starting from the 1990s. Between 2013 and 2022, the Center for Drug Evaluation and Research (CDER), the FDA's primary drug evaluation center, averaged approximately 43 novel drug approvals annually. However, due to the shared molecular origins of various diseases, an estimated 90% of approved drugs have secondary indications and can potentially be repurposed for other purposes [81]. A more recent estimate suggests that while only 10% of new molecular entities successfully reach the market following Phase II clinical trials and 50% following Phase III, the rates for repurposed compounds are significantly higher at 25% and 65%, respectively [82]. These figures highlight the higher success rates associated with repurposed drugs, underscoring their potential as valuable therapeutic options.

Typically, drug repurposing strategy involves three essential steps before advancing the candidate drug through the development pipeline. These steps include the identification of a candidate molecule for a specific indication, hypothesis generation, followed by a mechanistic assessment of the drug's effects in preclinical models. Subsequently, the drug's efficacy is evaluated in Phase II clinical trials, assuming sufficient safety data from Phase I studies conducted for the drug's original indication [78]. This approach offers significant advantages, including reduced development time and cost, known safety profiles, increased chances of success, and expanded treatment options.

Several notable examples demonstrate the success of drug repurposing [79]. For instance, aspirin (Acetylsalicylic acid) was initially used as a pain reliever and fever reducer but was later discovered to have antiplatelet properties. It is now widely used in low doses to reduce the risk of heart attacks, strokes, and blood clots [83]. Botox (Botulinum toxin), originally approved for the treatment of muscular conditions like strabismus and blepharospasm, has

been repurposed for cosmetic procedures, including wrinkle reduction, as well as for the treatment of chronic migraines, excessive sweating, and muscle spasticity [84].

Pharmaceutical companies have increasingly recognized the value of drug repurposing, leading to its popularity in recent years. Companies such as Pfizer, AstraZeneca, and GlaxoSmithKline have established specialized units dedicated to systematically scanning for repositioning opportunities [85]. Collaboration between academia, non-profit organizations, and pharmaceutical companies has also emerged to facilitate repurposing efforts and promote the sharing of resources and expertise.

The COVID-19 pandemic further emphasized the importance of drug repurposing as researchers quickly explored existing drugs for potential treatments against the virus. This heightened awareness has sparked greater interest and investment in drug repurposing within the pharmaceutical industry [86]. The lessons learned from the pandemic have underscored the value of repurposing existing drugs to address urgent medical needs and provide potential solutions during crises.

While drug repurposing offers significant advantages, it also presents challenges [87]. Limited patent protection for repurposed drugs, as they are often existing compounds, reduces the opportunity for exclusive marketing rights. This, in turn, reduces financial incentives for extensive research and clinical trials. Additionally, attracting funding for repurposing efforts may be more challenging compared to novel drug development. Conducting additional clinical trials for new indications can be time-consuming, expensive, and may not always yield positive results, leading to certain repurposing efforts being abandoned. Furthermore, a limited understanding of the underlying mechanisms of action for potential new uses hampers dosing optimization, prediction of side effects, and comprehension of drug interactions. Overcoming these challenges requires collaboration, careful consideration, and dedicated efforts. Despite these obstacles, drug repurposing remains a valuable approach with the potential to unlock new therapeutic opportunities and improve patient care.

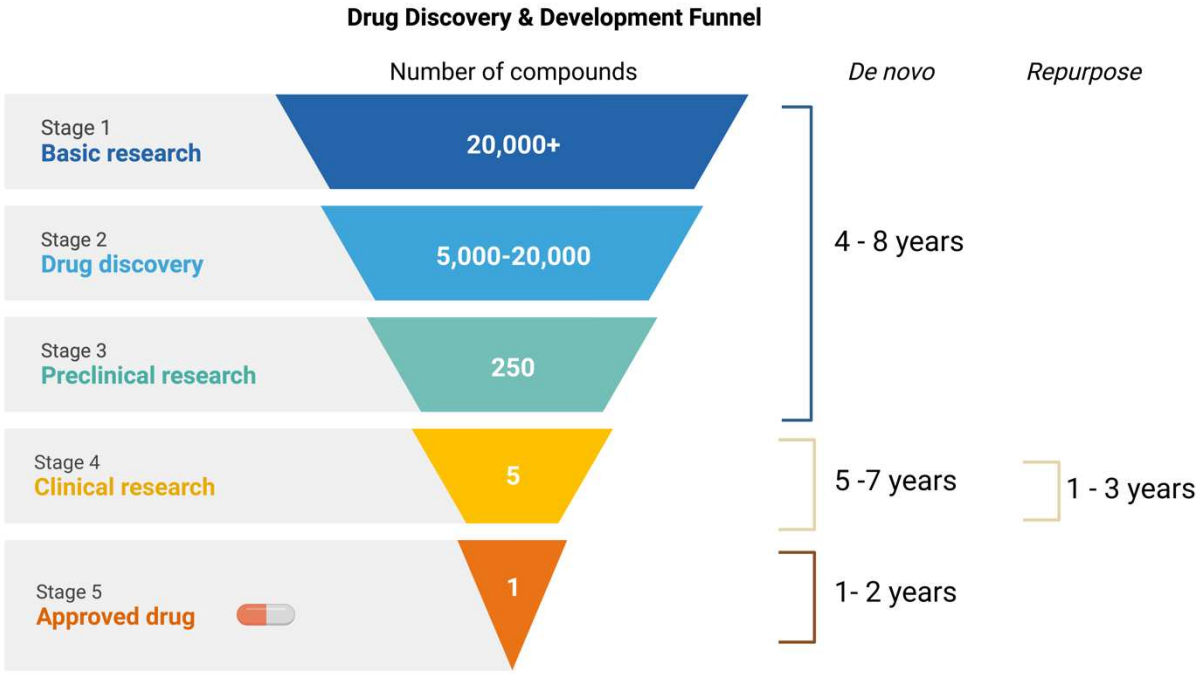

Figure 5. Drug discovery and development funnel.
A large number of potential drugs that, for various reasons, have failed to advance to clinical and commercial use can be added to candidates available for such purposes. Image was created with BioRender.com.

3 Aim of study

The primary objective of this study is to explore alternative drug options for the treatment of lower-grade gliomas with IDH1 R132 mutations. Our aim is to gain a comprehensive understanding of the molecular mechanisms that determine the sensitivity or resistance to TMZ in these specific gliomas. Specifically, I sought to reverse TMZ resistance, enhance its efficacy in tumor models, and identify synergistic drugs that can be combined with TMZ for improved therapeutic outcomes.

Additionally, I aimed to repurpose FDA-approved drugs to overcome TMZ resistance in IDH mutant gliomas. By investigating the potential of these drugs, I aimed to identify alternative treatment options that can effectively target and address the challenges associated with TMZ resistance in this specific subset of gliomas.

4 Results

4.1 Characterization of IDH1 mutant PDTs

In this part, I have analyzed the TMZ response from four PDTs that were derived from lower-grade gliomas with IDH1 R132 mutations diagnosed as grade 2 and 3. The four PDTs are TS603, SU-AO3, NCH1681, and NCH612. TS603 and SU-AO3 are oligodendrogliomas with complete 1p/19q co-deletion, while NCH1681 is an astrocytoma without 1p/19q loss. NCH612 has partial 1p/19q co-deletion, and I have considered it as an oligodendroglioma for this study.

4.1.1 Confirmation of IDH1 mutation in lower-grade gliomas and characterization of their growth features

In this study, our objective was to explore the underlying molecular mechanisms responsible for temozolomide (TMZ) resistance in IDH1 mutant gliomas. To achieve this, I initially confirmed the IDH1 mutation status in our patient-derived tumorspheres (PDTs) and conducted a comprehensive characterization of their growth properties in vitro.

All four tumorspheres exhibited a suspension growth pattern and formed spheroid-like cell aggregates in uncoated cell culture flasks. Through Western blot analysis, I successfully verified the presence of the IDH1 R132H hotspot mutation in the PDTs (Figure 6A). To assess the growth rate, I performed a seeding experiment using a cell number standard ranging from 0 to 1000 cells in 96-well plates. Subsequently, the cells were allowed to grow for four days without any treatment. I measured the MTT readings and compared the adjusted readings after subtracting the readings from the empty control wells. Our findings demonstrated that IDH1 mutant PDTs displayed slower growth rates compared to non-IDH1 mutant cells (Figure 6B). Among the IDH1 mutant PDTs, NCH612 exhibited relatively faster growth compared to NCH1681 and TS603, while SU-AO3 demonstrated the slowest growth rate. Specifically, when seeding $5x10^5$ cells in a 6-well plate, TS603 took 6-7 days to reach confluency, accompanied by the appearance of necrosis in the center of the tumorsphere. In contrast, SU-AO3 required 3-4 weeks to achieve confluency under the same conditions.

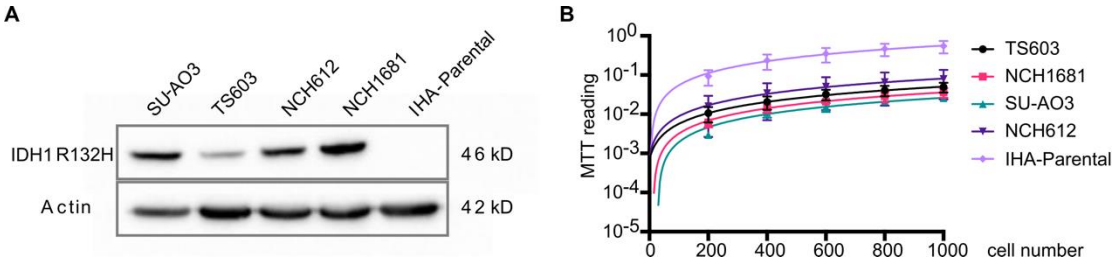

Figure 6. IDH mutation status of the PDTs and their growth rate.
(A) Western blot confirms IDH1mut protein expression in four PDTs. (B) Comparison of growth rates between IDH1mut PDTs and IHA cell line. Cells were seeded in 96-well plates with a cell number standard, and MTT readings were taken 4 days later.

4.1.2 Determining appropriate concentrations of TMZ for in vitro study using MTT assay

To ensure the validity of in vitro studies on our IDH1 mutant PDTs, I determined the maximum concentration of TMZ that could be used without causing significant cell death due to dimethyl sulfoxide (DMSO) toxicity. As TMZ has limited solubility in DMSO, it is crucial to consider the impact of DMSO on our subsequent experiments. I therefore investigated the dose response of our PDTs to both TMZ and DMSO to determine the maximum concentration of TMZ that could be used in vitro before DMSO causes more than 5-10% cell death.

The solubility of TMZ in DMSO is 50 mg/mL, so I prepared a stock of 92.7 mM based on this maximum solubility. I then calculated the subsequent DMSO control for each TMZ concentration gradient, using the criteria of 92.7 mM TMZ stock containing 100% DMSO. For instance, 100 µM TMZ has a DMSO control of 0.1%.

I utilized a colorimetric-based MTT cell viability assay, which assess the metabolic activity of the cells, to determine the IC_{50} of TMZ and IC_{10} of DMSO for each PDTs. To establish a TMZ and DMSO concentration gradient for the cells, I seeded an equal number of cells in 100 µL of medium into each well of a 96-well plate. The next day, I added 50 µL of medium containing varying amount of TMZ or DMSO from the 97.2 mM TMZ stock or 100% DMSO through serial dilution to each well to achieve the desired final concentration as designed. After 96 hours of incubation, I measured MTT readings and adjusted them by subtracting the background reading obtained from wells containing only medium but without cells. I then normalized the survival percentage of each treatment well to that of the non-treated wells based on the adjusted reading.

The IC_{50} and IC_{10} values of TMZ and DMSO were calculated using the GraphPad Prism software, based on the [inhibitor] vs. response variable slope (four parameter) equation

derived from the dose-response curve. The results showed that all IDH^{mut} PDTs exhibited a significantly higher IC_{50} of TMZ compared to GBM PDT and immortalized human astrocytes (IHAs) (Figure 7A). IHAs and isogenic cells expressing mutant IDH1 (R132H), wild-type IDH1, or neither have been well-characterized and utilized in our previous study to investigate the role of IDH1 in hypermethylation [4]. Specifically, the IC_{50} values of TMZ for the IDH1^{mut} gliomas TS603, SU-AO3, NCH1681 and NCH612 were 211.3 μM, 205.2 μM, 252.2 μM and 121.5 μM, respectively. The IDH1^{WT} glioma line L0627 had an IC_{50} of 71.75 μM, while the parental, IDH1^{mut} and IDH1^{WT} immortalized human astrocytes (IHAs) had IC_{50} values of 10.61 μM, 10.61 μM and 11.76 μM respectively (Table 1). The IC_{10} values of DMSO for the IDH1^{mut} gliomas TS603, SU-AO3, NCH1681 and NCH612 were 0.053%, 0.02%, 0.044% and 0.98% respectively (Figure 7B, Table 2), which is equivalent to the TMZ concentration of 53 μM, 20 μM, 44 μM and 980μM. Therefore, the upper limit for in vitro TMZ treatment concentration should not exceed these values. The experiments were repeated multiple times (7 biological repeats, each with three technical repeats), with varying cell number seeding (800-5000), to ensure reproducibility of the results. Outliers were eliminated based on a comparison of the parameters (bottom, top, IC_{50}, hillslope) using Prism. Therefore, to minimize the toxicity from DMSO, the concentration of TMZ used for all IDH1 mutant PDTs should be limited to less than 100 μM, except for NCH612 which exhibited higher sensitivity to TMZ and higher resistance to DMSO.

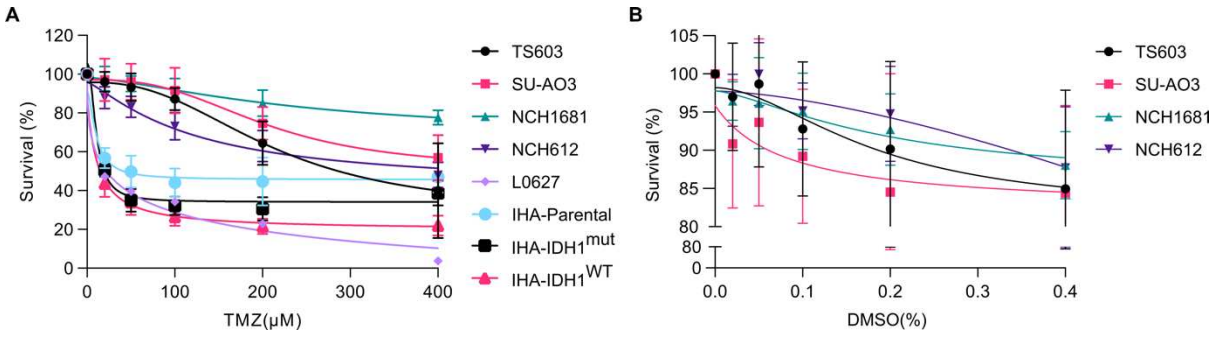

Figure 7. Dose response curves of TMZ and DMSO.

(A) Dose response curve of TMZ from MTT viability assay between IDH1 mutant (IDH1mut), IDH1 Wild Type (IDH1WT) PDTs and IHAs (n≥3 biological repeats, each with 3 technical repeats). IC50 values were calculated using GraphPad Prism with [inhibitor] vs. response (four-parameter) model.

(B) Response of IDH1mut PDTs to DMSO treatment. IC10 values for TS603, SU-AO3, NCH1681, and NCH612 were 0.053%, 0.02%, 0.044%, and 0.98%, respectively, calculated using GraphPad Prism with [inhibitor] vs. response (four-parameter) model.

Table 1. IC_{50} values of TMZ.

IC_{50} of TMZ	Oligodendroglioma		Astrocytoma		IDH1WT	IHAs		
	IDH1mut-codel		IDH1mut-non-codel					
	TS603	SU-A03	NCH1681	NCH612	L0627	Parental	IDH1mut	IDH1WT
Bottom	28,64	50,63	67,14	41,21	-31,19	45,62	34,11	19,57
Top	95,8	97,08	98,17	95,91	98,18	91,1	105,5	88,62
IC_{50}	211,3	205,2	252,2	121,5	71,75	10,61	10,61	11,76
HillSlope	-2,501	-2,769	-1,462	-1,228	-0,4371	-1,649	-2,036	-1,006
logIC_{50}	2,325	2,312	2,402	2,084	1,856	1,026	1,026	1,07
Span	67,16	46,45	31,03	54,7	129,4	45,48	71,37	69,05

IC_{50} of DMSO	TS603	SU-AO3	NCH1681	NCH612
Bottom	81,99	82,21	85,90	-270,3
Top	98,20	95,87	97,76	97,75
IC_{50}	0,1841	0,08110	0,1971	4,085
HillSlope	-1,826	-0,9972	-1,455	-1,541
logIC_{50}	-0,7350	-1,091	-0,7053	0,6112
Span	16,20	13,65	11,86	368,0
IC_{10}	0.053	0.02	0.044	0.98

Table 2. IC_{50} and IC_{10} values of DMSO.

4.1.3 Validation of the TMZ efficacy IDH1 mutant PDTs using colony formation assay

To validate the TMZ resistance of our IDH1 mutant PDTs, I employed two more analysis including a 3D soft agar culture system and direct cell counting after treatment with TMZ.

For the soft agar colony formation analysis, I seeded 10,000-15,000 cells in the middle layer of a three-layer agar culture and treated them with 100μM TMZ after one week of recovery, TMZ was administered continuously for four days with daily drug replacement. After 96 hours, fresh drug-free medium was added, which was replenished weekly according to the cell growth rate. Approximately one month later, the colonies became visible to the naked eye, at which point they were stained with 0.005% crystal violet, and images were captured. Colony number and size were quantified with ImageJ. I found that, in three of the IDH1 mutant PDTs (TS603, SU-AO3 and NCH1681), there was no difference in colony number and size between the 0.1% DMSO control and TMZ-treated sample (Figure 8 A, B, C), indicating that TMZ did not affect

the tumorigenic potential and confirmed the TMZ resistance (TMZ-R) of TS603, NCH1681, and SU-AO3. NCH612, on the other hand, showed high sensitivity to TMZ in this treatment regime, as no colonies were formed after TMZ treatment.

For direct cell counting, a total of $1x10^5$ cells of TS603, NCH1681, and NCH612, and $2x10^5$ cells of SU-AO3 were seeded in 6-well laminin coated plates and treated with 100 µM TMZ or 0.1% DMSO with daily drug replacement. After four days of drug treatement, cells were harvested and counted using trypan blue staining in an illuminar cell counter. I found that NCH612 had lower survival compared to the 0.1% DMSO control, while TS603, SU-AO3, and NCH1681 showed no significant difference in survival (Figure 8D). These results provide further evidence of the TMZ resistance of the IDH1 mutant PDTs and highlight NCH612 as a potentially more sensitive cell line.

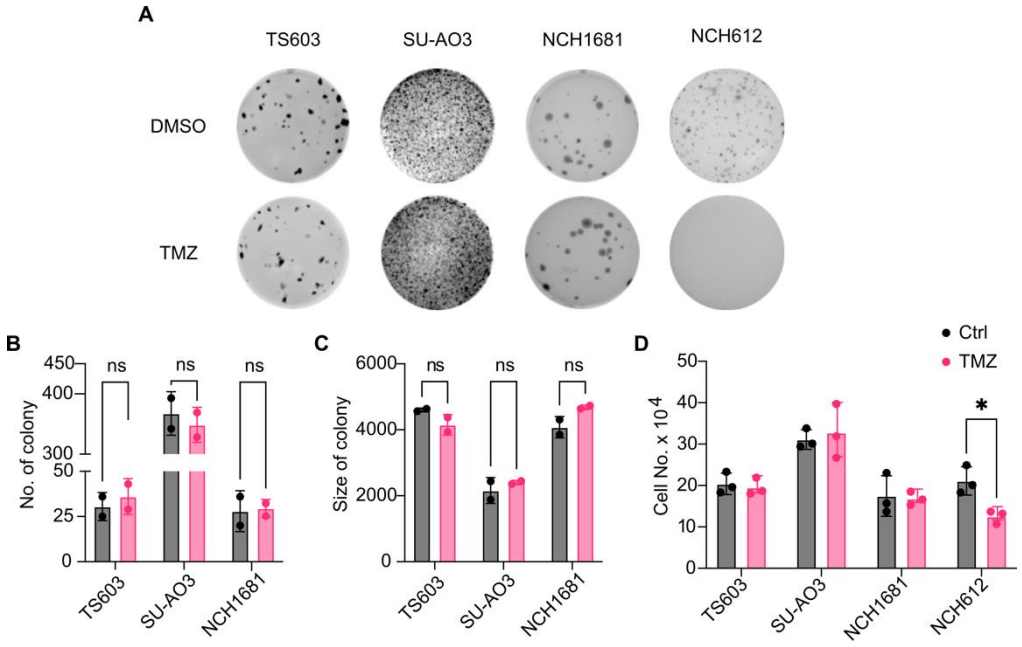

Figure 8. Validation of TMZ resistance in IDH1 mutant PDTs.
(A) Soft agar colony formation assay in PDTs upon TMZ treatment. 10000 cells of TS603 and NCH1681, 15000 of SU-AO3 were seeded, treated with 100 µM TMZ for 4 days, followed by one month of colony growth. (B) Quantification of colony number from panel A using ImageJ analysis. Unpaired two-tailed t-test was performed. (C) Quantification of colony size from panel A using ImageJ analysis. Unpaired two-tailed t-test was performed. (D) Comparison of cell number upon TMZ and DMSO treatment. Cells ($1x10^5$ cells of TS603, NCH1681, and NCH612, and $2x10^5$ cells of SU-AO3) were seeded in a 6-well plate, 100 µM TMZ or 0.1% DMSO was added the next day. After 96 hours of incubation, cells were harvested and counted with trypan blue staining in an Illumina cell counter.

Thus I employed a range of assays, including MTT viability, soft agar growth, cell number counting, to evaluate the response of our IDH1 mutant PDTs to TMZ. Our results indicate that TS603, SU-AO3, and NCH1681 are resistant to TMZ and are representative of recurrent TMZ-R IDH1 mutant PDTs, whereas NCH612 exhibited slight sensitivity to TMZ. These results serve as basis for further investigations into the molecular mechanisms underlying TMZ resistance and the exploration of combination therapies to restore TMZ sensitivity in the next chapters.

4.2 Investigating transcriptome-based strategies for overcoming TMZ resistance

4.2.1 Transcriptome analysis of IDH1 mutant PDTs in response to TMZ treatment

To analyze the transcriptional changes induced by TMZ treatment, I conducted RNA-seq analysis on TMZ resistant PDTs of TS603, NCH1681, and TMZ sensitive PDT of NCH612. The cells were treated with 100 µM TMZ for 96 hours with daily drug refreshing, and the RNA was subjected to single-read analysis on a HiSeq 4000 sequencing platform.

Our analysis revealed that the TMZ-resistant TS603 and NCH1681 exhibited stable transcriptomes upon TMZ treatment, with only two genes downregulated in TS603 and four genes downregulated in NCH1681 (Figure 9 A, B). These results suggest a lack of response to the drug and may indicate that alternative mechanisms are responsible for TMZ resistance in these cells. In contrast, NCH612 exhibited slight sensitivity to TMZ treatment, with 88 downregulated genes and 141 upregulated genes (Figure 9C).

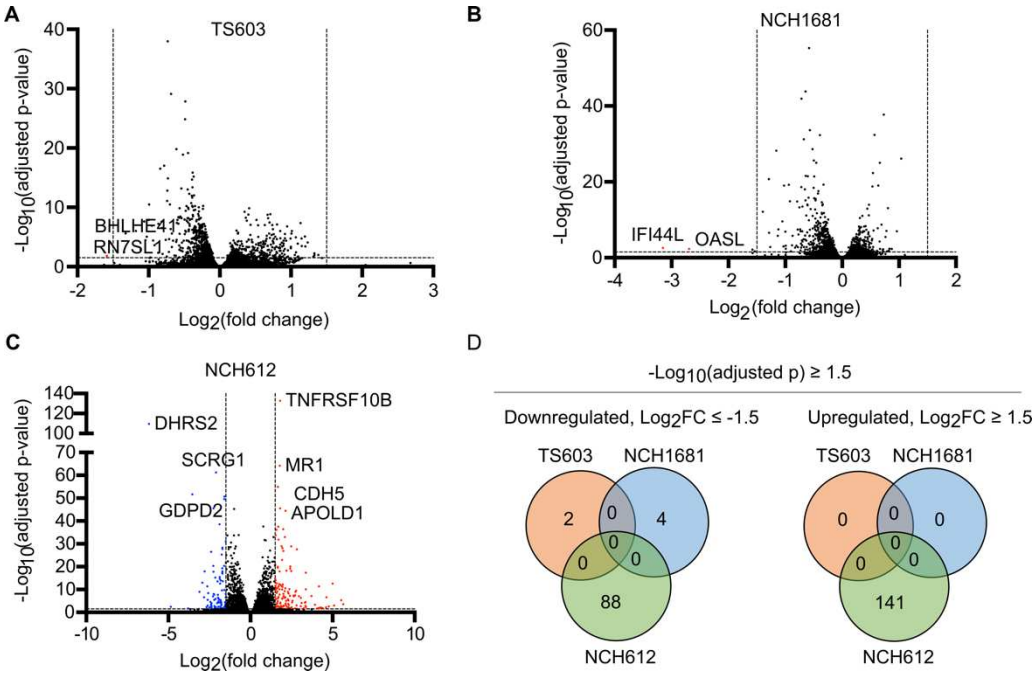

Figure 9. Transcriptional response of IDH1 mutant PDTs to TMZ treatment.
(A, B, C) Volcano plots showing the RNA-seq data of TS603, NCH1681, and SU-SO3 treated with TMZ. (D) Venn diagrams depicting the overlap of significant changes in gene expression (log2(fold change) ≤-1.5 or log2(fold change) ≥1.5, with log10(adjusted p value) >1.5) observed in the three IDH1mut PDTs upon TMZ treatment.

4.2.2 Enriched KEGG pathways in response to TMZ treatment

To explore the molecular interaction, reaction and relation networks, I submit the 88 downregulated and 141 upregulated genes in NCH612 in http://metascape.org for Kyoto Encyclopedia of Genes and Genomes (KEGG) pathway analysis. I found that the upregulated genes were enriched in several pathways, including P53, MAPK, Rap1 and Ras signaling pathways. The downregulated genes were enriched in pathways related to gastric acid secretion, protein digestion and absorption, and TGF-beta signaling pathway (Figure 10A). Additionally, I found that P53 was an upregulated transcriptional factor from GO_TRRUST analysis (Figure 10 B). P53 is a tumor suppressor protein that plays a crucial role in maintaining genomic stability by regulating the cell cycle, DNA repair, and programmed cell death (apoptosis). The fact that P53 activation and its molecular function as a tumor suppressor, led us to investigate whether activating P53 in other TMZ resistant lines could restore sensitivity to the drug.

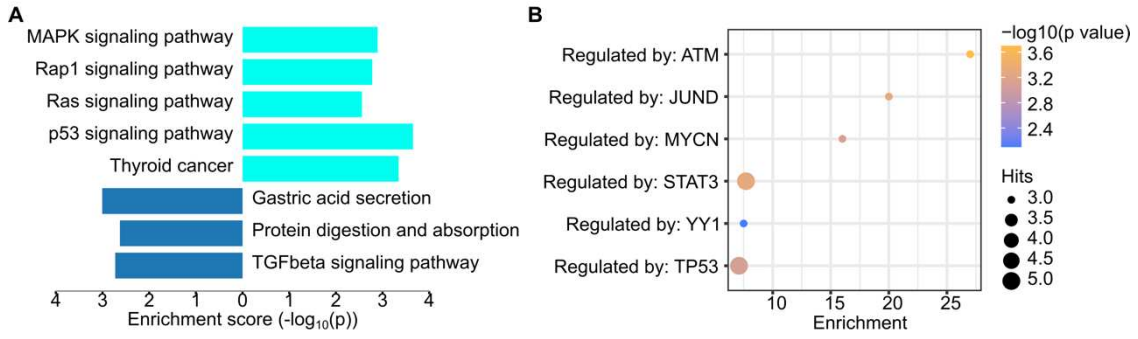

Figure 10. Pathway enrichment and transcriptional regulators in response to TMZ treatment.
(A) KEGG pathway analysis of down- and up-regulated proteins in NCH612. (B) Enrichment bubble plot of the activated transcriptional factors. The data was analyzed and obtained from Metascape, and the figures were generated using SRplot. Figures modified from [88].

4.2.3 Combination treatment of P53 activator RITA with TMZ

To test the hypothesis of whether activating P53 pathway would increase the sensitivity of cells to TMZ, I first examined the P53 gene mutation status in our PDTs using Panel-seq data generated from the lab. I found nonsynonymous SNVs (single nucleotide variation) in TP53 in all four lines (Table 3). The observed discrepancy between TP53 activation from pathway analysis and the fact that TP53 are all mutated in our PDTs might be due to the following reasons: it is possible that some of these nonsynonymous SNVs do not affect its transcriptional activity or that other compensating factors allow for the P53 signaling pathway upregulation upon TMZ treatment. Additionally, other genes within the P53 signaling pathway may also be upregulated, contributing to the overall enrichment of the pathway in response to TMZ treatment.

TP53 mutation status	
PDTs	**Nonsynonymous SNV**
TS603	exon3:C98G; exon4:C215G, C98G
SU-AO3	exon3:C98G; exon4:C215G, C98G
NCH1681	exon2:C173G, C92G; exon5:C452G; exon6:C569G, C452G
NCH612	exon3:C98G; exon4:C215G, C98G, C421T, C340T; exon7: C700T; exon8: C817T

Table 3. TP53 mutation status from panel-seq.

To further investigate the underlying molecular mechanisms and explore the potential for enhancing the efficacy of TMZ in treating IDH1 mutant glioma, I searched for drugs targeting the P53 signaling pathway. I found the drug RITA (reactivation of p53 and induction of tumor cell apoptosis) could induce p53-dependent apoptosis in both wild-type and mutant p53 neuroblastoma, activated p53, and triggered the expression of proapoptotic p53 target genes, specifically, it had a strong antitumor effect *in vivo* [89]. Thus, I hypothesize that the combination of RITA with TMZ may enhance the efficacy of TMZ and serve as a potential combination therapeutic strategy in treating IDH1mut glioma.

4.2.3.1 Direct RITA and TMZ combination therapy showed no additive effect

I began by examining the response of our cell lines to RITA, determining the IC_{50} values for TS603, SU-AO3, NCH1681, and NCH612 as 32.82 μM, 0.094 μM, 2.94 μM, and 4.67 μM, respectively. All of our IDH1 mutant PDTs exhibited sensitivity to RITA. I picked RITA concentration of 3 μM for initial combination treatment with TMZ, as this is the dosage close to the IC_{50} value of three PDTs. The solubility of RITA in DMSO is 20 mg/ml. I prepared a stock solution of 50 mM, which corresponds to dissolving 1 mg of RITA in 68.4 μL of DMSO. Therefore, a concentration of 3 μM RITA is equivalent to 0.006% of the DMSO control.

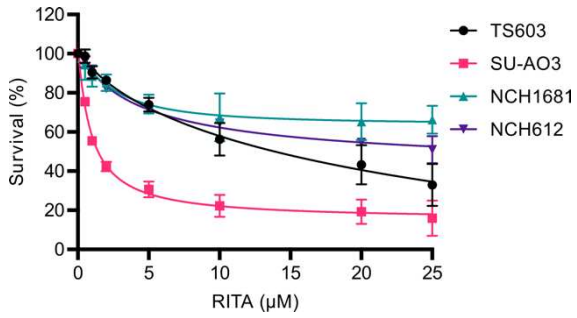

Figure 11. Dose response curve of RITA in IDH1 mutant PDTs .

	TS603	SU-AO3	NCH1681	NCH612
Bottom	-50,47	15,14	63,82	39,70
Top	104,8	103,7	95,75	104,9
IC_{50}	32,82	0,9365	2,936	4,668
HillSlope	-0,7052	-1,038	-1,447	-0,8350
logIC50	1,516	-0,02851	0,4678	0,6691
Span	155,3	88,60	31,93	65,25

Table 4. IC_{50} values of RITA in IDH1 mutant PDTs.

I conducted our first combination therapy by treating $1x10^5$ cells from TS603, NCH1681, and NCH612, along with $2x10^5$ cells from SU-AO3 in 12-well plates, with 3 μM RITA and 100 μM TMZ alone or in combination for 96 hours and counted the cells after the treatment. RITA exerted an efficacy in TS603 and SU-AO3 cell line, and the effect of TMZ and RITA combination was mainly due to RITA, as the cell number was not significantly differed between RITA alone or RITA combined with TMZ (Figure 12 A, B). However, RITA alone or RITA combined with TMZ showed no effect in NCH1681 and NCH612 compared with the controls (Figure 12 C, D). Our results indicate that direct RITA and TMZ combination therapy with such dosing regimen did not show a synergistic effect on IDH1mut glioma cell lines.

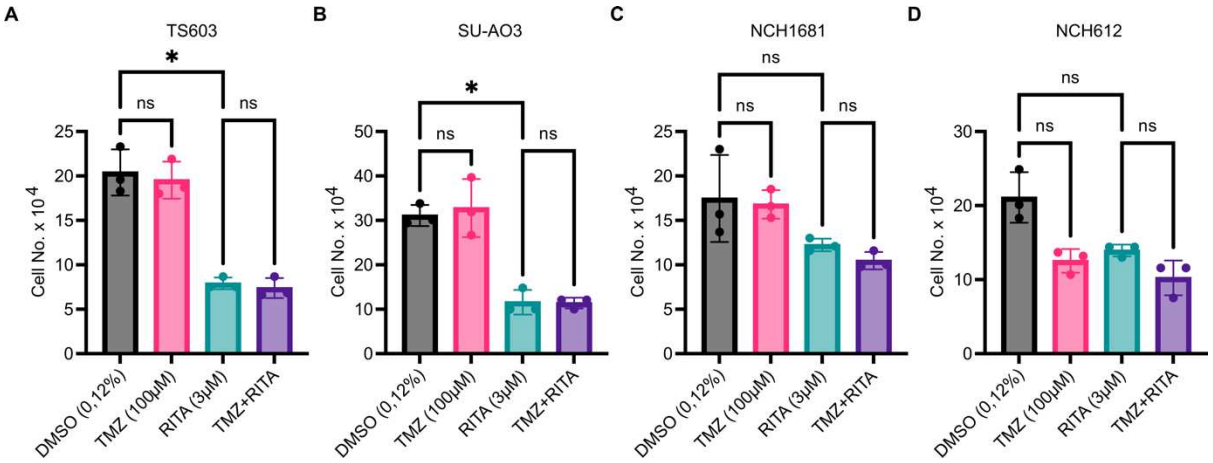

Figure 12. Efficacy of RITA and TMZ combination.
(A-D) Cell number counting demonstrating the efficacy of RITA and TMZ combination therapy. data analyzed with unpaired t test.

4.2.3.2 Pre-RITA treatment followed by TMZ shows varied synergistic effects

As I reported in section 4.2.3.1, our initial attempts to treat cells with a direct combination of RITA and TMZ did not yield the desired results. In light of these findings, I decided to explore a new treatment approach that involved pre-treating the cells with RITA before administering TMZ, based on our hypothesis that it takes time for RITA to activate the P53 pathway and increase the cells' sensitivity to TMZ. This new approach involved pre-treating the cells with RITA (Pre-RITA) first, followed by treatment with TMZ, instead of directly combining the two drugs.

To evaluate the effectiveness of the pre-RITA followed by TMZ treatment approach, I seeded cells that had been treated with 0.12% DMSO and 3 μM RITA from the previous experiment into 96-well plates and exposed them to different concentrations of TMZ. I observed that the MTT readings of the Pre-RITA treated cells were significantly lower than those of the control cells at each TMZ concentration, except for NCH612, in which the Pre-RITA treated samples had higher MTT readings than the control samples at higher TMZ concentrations (Figure 13 A, B, C, D).

To determine whether there was a synergistic effect between RITA and TMZ, I used Combenefit to obtain the synergy value for each combination treatment by inputting the survival data of RITA alone, TMZ alone, and Pre-RITA followed by TMZ. Here, the survival of the Pre-RITA treated cells was normalized to that of the DMSO treated cells, assuming that the concentration of 0.12% DMSO had no effect on the cells' response to TMZ. According to

the Bliss model, a synergy score less than -10 is considered as antagonistic, above 10 is synergistic, and in between -10 to 10 is considered additive.

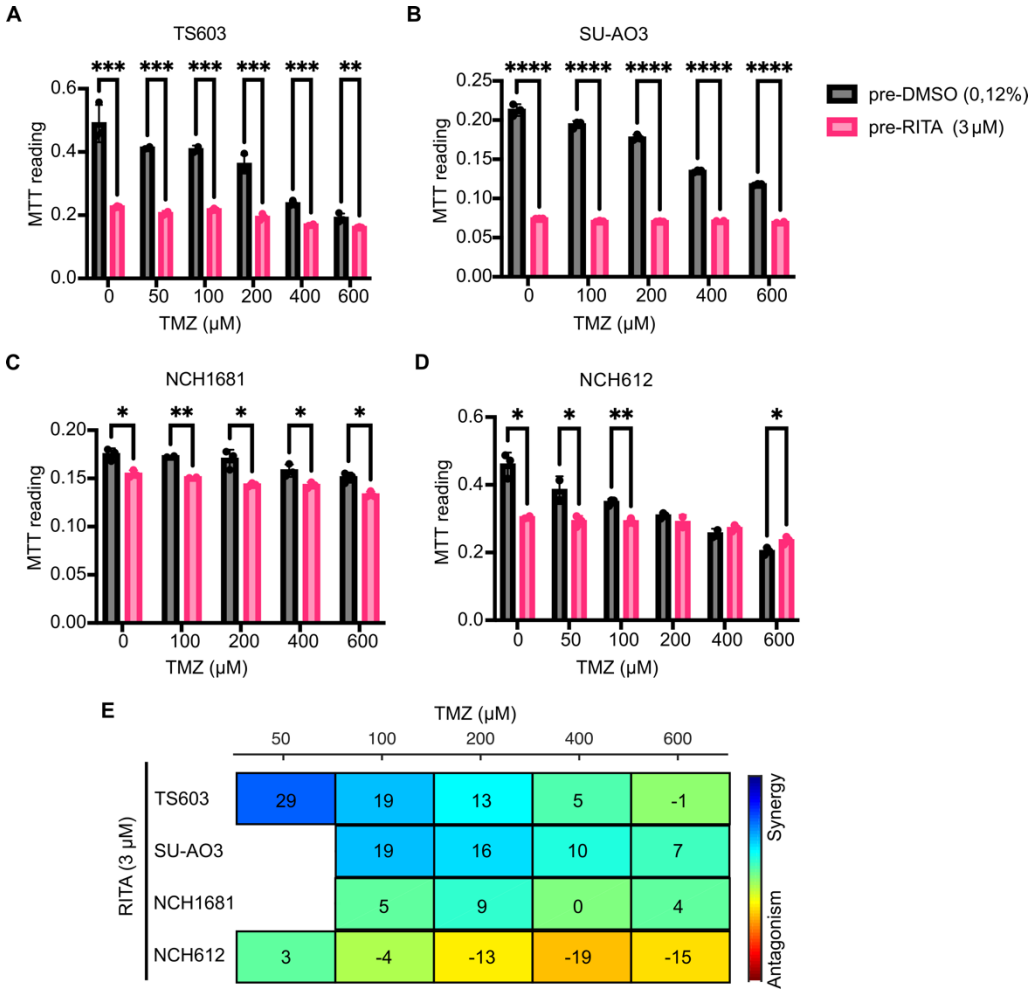

Figure 13. Response of PDTs to Pre-RITA treatment followed by TMZ treatment.
(A-D) MTT assay results of Pre-RITA treated cells exposed to varying concentrations of TMZ. Cells were pre-treated with 0.12% DMSO and 3 µM RITA for 96 hours, then seeded at 2000 cells per well in 96-well plates and exposed to variable concentrations of TMZ for another 96 hours. Data comparison using unpaired t test. (E) Synergy scores of 3µM RITA pre-treatment followed by TMZ combination regimen calculated using Combenefit.

The Combenefit analysis showed that the combination treatment had varying effects on different cell lines (Figure 13 E). TS603 and SU-AO3 showed a synergistic effect with Pre-RITA followed by TMZ treatment. In TS603, with 3 µM RITA, the synergy scores were 29, 19, and 13 at TMZ concentrations of 50µM, 100µM, and 200µM, respectively. In SU-AO3, the synergy scores were 19, 16, and 10 at TMZ concentrations of 100 µM, 200 µM, and 400 µM, respectively. On the other hand, NCH1681 only showed a slight additive effect at TMZ concentrations of 100 µM and 200µM. Surprisingly, NCH612 showed a significant antagonistic

effect between TMZ and RITA, with synergy scores of -13, -19, and -15 at TMZ concentrations of 200 µM, 400 µM, and 600 µM.

The results raise intriguing questions regarding the differential response of the four PDTs to the combination treatment regime, particularly in NCH612. Our previous analysis had indicated that TMZ treatment increased the activation of the P53 signaling pathway, which has been linked to increased TMZ sensitivity. However, contrary to our expectations, activating this pathway did not restore TMZ sensitivity in NCH612, and instead, I observed strong antagonism in this combination regime. In contrast, activating P53 in TS603 and SU-AO3 sensitized cells to TMZ. It is possible that there is a threshold level of P53 activation beyond which combining it with TMZ does not confer any benefit, as evidenced by the lack of synergistic effect in NCH612 despite the activation of the P53 pathway. However, there may be other factors at play that contribute to the different responses of the PDTs to the combination treatment regime. For example, there may be differences in the expression or activity of proteins involved in DNA damage response pathways, which can impact the cells' sensitivity to TMZ. Additionally, the cells may have different levels of drug uptake or metabolism, which can affect the concentration of TMZ within the cells and subsequently impact the drug's effectiveness. It is also possible that there are differences in the genetic or epigenetic profiles of the cells, which can influence their response to drug treatment. These findings highlight the complex interplay between different signaling pathways and their contribution to drug sensitivity in different cells.

4.3 Investigating metabolome-based strategies for overcoming TMZ-resistance

Reprogramming of cellular metabolism is a fundamental characteristic of cancer, and IDH1/2 mutations represent key therapeutic targets in this arena [90]. Given the critical role of metabolism in cancer, I hypothesized that the metabolic alterations associated with the IDH1 mutation may play a significant role in determining sensitivity or resistance to TMZ. Therefore, in this chapter, I aimed to investigate metabolome-based strategies for overcoming TMZ resistance in IDH1 mutant gliomas. Our approach involves analyzing the metabolic profile of IDH1 mutant glioma PDTs in response to TMZ treatment and identifying potential metabolic vulnerabilities that could be exploited to sensitize them to TMZ treatment.

4.3.1 Metabolome vulnerabilities of IDH1 mutant gliomas in response to TMZ treatment

In order to investigate the metabolic alterations that may contribute to TMZ resistance in IDH1mut gliomas, I performed a metabolome analysis of TS603, SU-A03, NCH1681, and

NCH612 PDTs. For sample preparation, 300,000 cells were seeded in 60 mm x 15 mm plates and treated with either 400 µM TMZ or 0.4% DMSO control or no treatment for 24 and 96 hours. Additionally, the no treatment samples were used for measurement of the base levels of metabolites to eliminate the effect of DMSO.

To prepare the samples for metabolome analysis, spheroids were dissociated into single cells using accutase, and cell numbers were counted. The cells were then washed three times with cold PBS and frozen in dry ice before being stored at -80°C. The metabolome analysis was performed using both GC/MS (Gas Chromatography-Mass Spectrometry) and MS/MS (Tandem Mass Spectrometry) metabolic assays. To ensure accurate data analysis, the protein concentration of the same vial after the metabolic assay was measured for normalization of the final concentration of metabolites. The TCA cycle was analyzed for 12 chemicals, while 29 fatty acids and 23 amino acids were measured.

To ensure the validity of the data, I compared each metabolic candidate using Grubb's method to remove any outliers that were much larger or smaller than the rest. Next, I used principal component analysis (PCA) to qualitatively analyze the major variances in the spectra and examine the separation of different variables, each represented by three biological replicates. I observed that the metabolic changes in TS603, SU-A03, and NCH1681 cells between DMSO and TMZ treatment could not be distinguished from PCA analysis. This lack of separation may be due to the high concentration of DMSO used, which may have exceeded the effect of TMZ at these concentrations. Although PCA analysis did not show any separation of TMZ and DMSO at 24 hours of treatment for all PDTs, NCH612 exhibited a clear separation between DMSO and TMZ treatments at 96 hours of treatment (Figure 14 A, B, C). As previously measured, this cell line is sensitive to TMZ and has a high DMSO tolerance, and DMSO did not exert toxicity to this line at such concentration (Figure 7, Table 2). Therefore, I focused on the metabolic changes in NCH612 at 96 hours of treatment, which provided valid data to demonstrate the effect of TMZ.

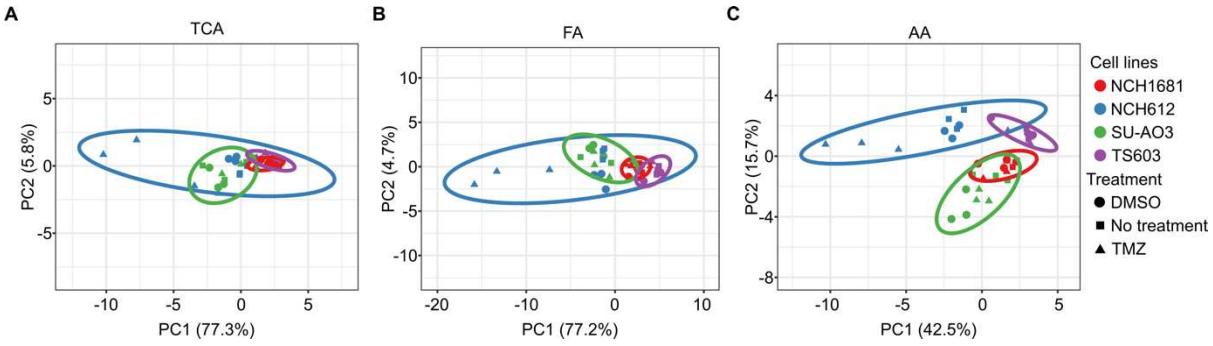

Figure 14. PCA analysis of metabolism in IDH1 mutant glioma.
(A-C) PCA analysis of TCA cycle, fatty acid, and amino acid metabolites, respectively. Data collected after 96 hours of treatment with 400μM TMZ, 0.4% DMSO, or no treatment in TS603, SU-AO3, NCH1681, and NCH612 cells. N=36 data points. Figure was made from https://biit.cs.ut.ee/clustvis/.

To visualize the metabolic changes in NCH612, I calculated the $\log_2$ fold change of TMZ and DMSO relative to the no-treatment samples. To better present this data, I used a balloon plot generated using SRplot. All values were converted to their absolute value due to the requirements of the balloon plot. Absolute $\log_2$ fold changes greater than 1 were considered significant and indicate up or downregulation of metabolites. I referred to the original analyzed data to determine whether a metabolite was up or downregulated.

In the TCA (tricarboxylic acid) cycle metabolites of NCH612, I observed the upregulation of several metabolites, including isocitric acid, oxaloacetic acid, 3-OH-Glutaric acid, 2-OH-Glutaric acid, Glutaric acid, pyruvic acid, succinic acid, and malic acid. These metabolites exhibited log2 fold change values of 1.2, 1.4, 1.4, 1.6, 1.2, 1.6, 1.4, and 1.6, respectively (Figure 15). Regarding fatty acid analysis in NCH612, I observed alterations in 19 out of 27 available fatty acid data, with positive log2 fold change values. The affected fatty acids include C5, C0, C5OH+MMA, C14, C4, C12, C16:1, C6, C5:1, C8:1, C16:1OH, C16, C18:1, C18, C8, C10:2, C14:2, C14:1, and C18:2, with log2 fold change values ranging from 1.0 to 2.0 (Figure 16). The "C" notation represents fatty acids with varying numbers of carbon atoms. Additionally, in the amino acid (AA) analysis of NCH612, I observed the upregulation of three out of the 20 measured amino acids. Specifically, Tyr, Glut, and MeGlut showed positive log2 fold change values of 1.0, 1.5, and 2.0, respectively (Figure 17). These observed upregulations suggest that these metabolites may play a significant role in the cellular response to TMZ treatment and potentially contribute to TMZ resistance.

In summary, our findings indicate that NCH612, a TMZ-sensitive cell line, undergoes significant metabolic changes upon treatment with 400μM TMZ for 96 hours. The alterations in metabolites include upregulation of 7 out of 11 metabolites in the TCA cycle, 19 out of 27 fatty acids, and 3 out of 20 amino acids. Based on these findings, I have focused our attention on targeting the TCA cycle and fatty acid-related metabolic pathways in our drug combination treatment approach.

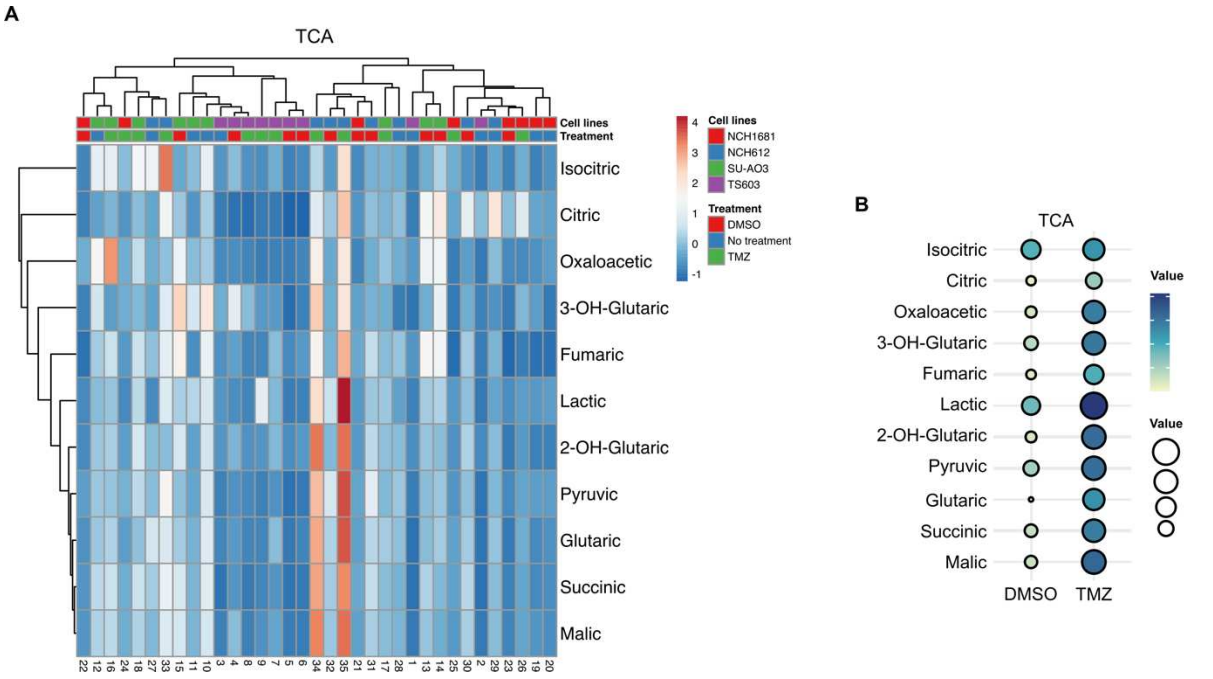

Figure 15. Metabolic of TCA alteration upon TMZ treatment.

(A) Heatmap PCA analysis of TCA cycle. (B) Bollon plot representing the metabolict change in NCH612 in TCA cycle. Data collected after 96 hours of treatment with 400μM TMZ, 0.4% DMSO, or no treatment. Figure is made from https://biit.cs.ut.ee/clustvis/.

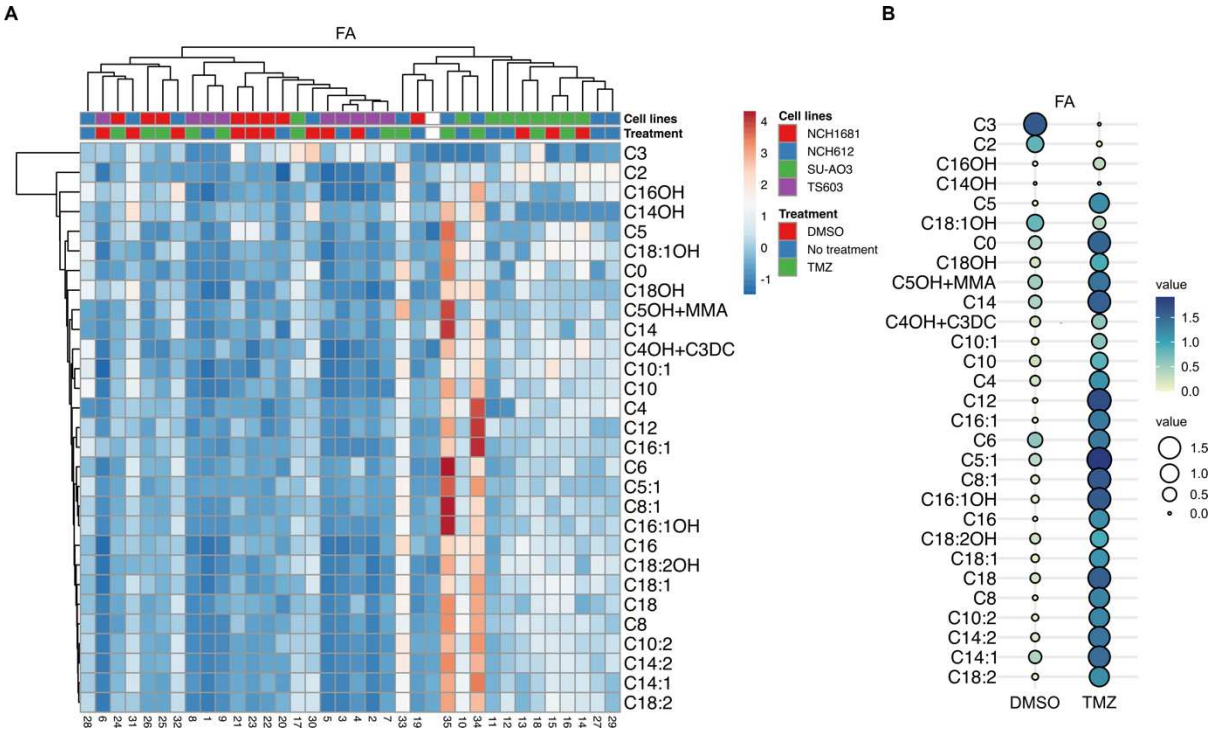

Figure 16. Metabolic of tatty acid (FA) alteration upon TMZ treatment.

(A) Heatmap PCA analysis of TCA cycle. (B) Bollon plot representing the metabolic change in NCH612 in TCA cycle. Data collected after 96 hours of treatment with 400μM TMZ, 0.4% DMSO, or

no treatment. C is abbreviations for various fatty acids with different carbon atoms. Figure is made from https://biit.cs.ut.ee/clustvis/.

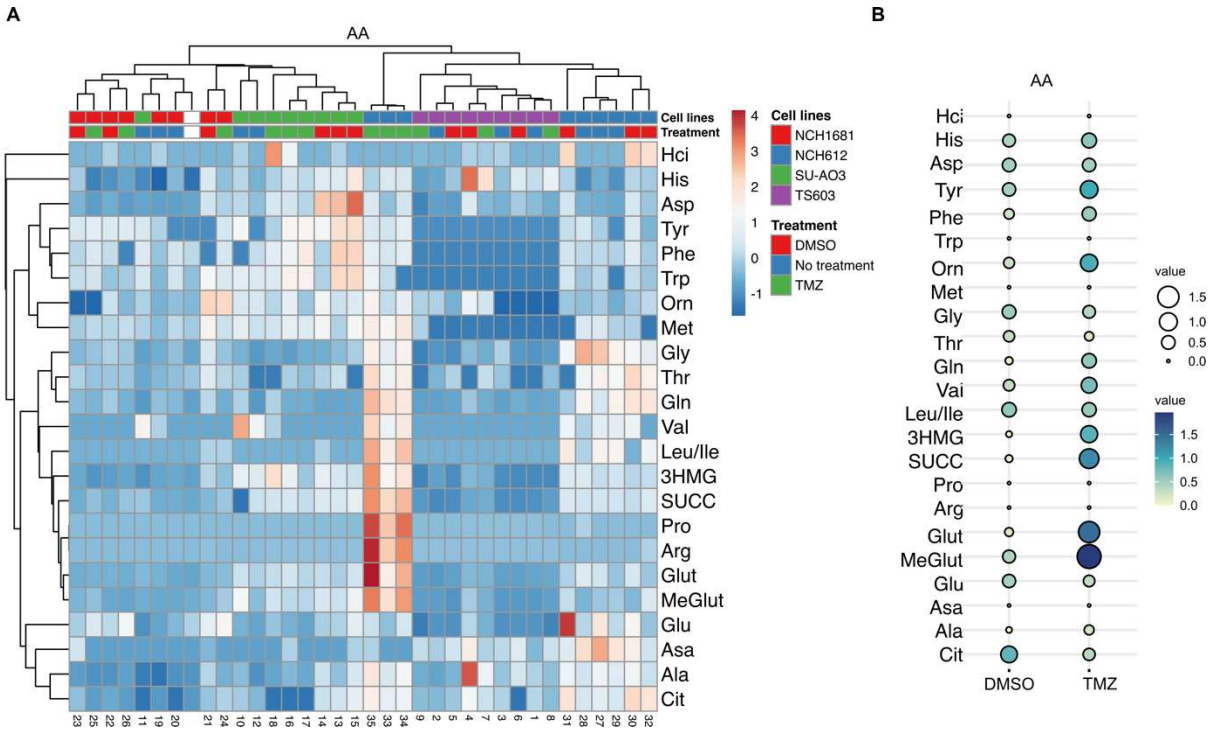

Figure 17. Metabolic of amino acid (AA) alteration upon TMZ treatment.
(A) Heatmap PCA analysis of Amino acids. (B) Bollon plot representing the amino acids change in NCH612. Data collected after 96 hours of treatment with 400μM TMZ, 0.4% DMSO, or no treatment. Each dot represents the average of three biological repeats with absolute log2 fold change relative to non-treatment samples. Figure is made from https://biit.cs.ut.ee/clustvis/.

4.3.2 Combination treatment of glycolysis inhibitor with TMZ

Cancer metabolism has its origins in the groundbreaking observations made by Otto Warburg, who noted that proliferating cells, including cancer cells, have a tendency to consume glucose and produce lactate even in the presence of oxygen. This phenomenon, known as aerobic glycolysis or the Warburg effect [91], reflects changes in cellular metabolism associated with proliferation rather than being a unique characteristic of malignancy. However, it is important to note that the majority of cancer cells rely on respiration to drive flux through the tricarboxylic acid (TCA) cycle in order to support tumor growth [92]. While there are certain tumors that may not respire, they still utilize the TCA cycle to obtain essential metabolites necessary for their growth [93]. In contemporary understanding, it is recognized that both glycolysis and the TCA cycle contribute to tumor growth by facilitating the synthesis of crucial metabolites [90, 94, 95].

Based on our analysis of the upregulated TCA cycle metabolites in response to TMZ in NCH612, I hypothesized that cell may need to increase its glucose intake to cope with the stress generated by TMZ treatment. Additionally, I considered whether the resistant cell line had built up a high level of glucose-related metabolites as a base level to alleviate the effect of the TMZ treatment. However, our investigation into the original data of TCA members without any treatment showed that this was not the case (Figure 18). The cell line SU-AO3 had the highest level of all TCA metabolites, followed by NCH612, then NCH1681, while TS603 had the lowest base level of metabolites. The results from two TMZ-sensitive cell lines, TS603 and SU-AO3, were contradictory as TS603 had the lowest base level of sugar metabolites while SU-AO3 had the highest. This suggests that there are no established levels of metabolites in TCA that can reliably predict the sensitivity or resistance of a cell line to TMZ treatment.

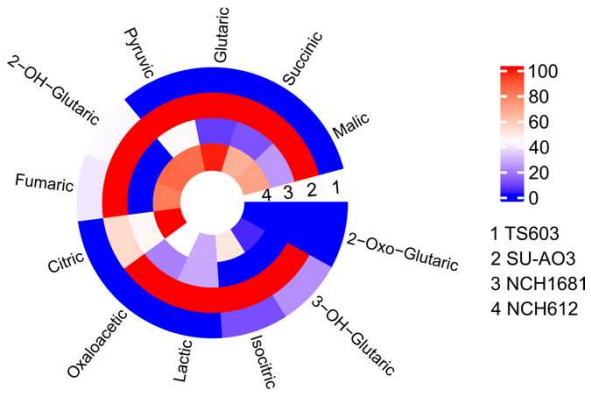

Figure 18. Baseline levels of TCA cycle metabolites.
The average level of each metabolite was normalized. The smallest value within the group is considered 0%, the largest value in each data set is considered 100%. And the data was analyzed in Prism and plotted in an SRplot.

After comparing the base level of the metabolites and exclude its role in contributing to the TMZ sensitivity. I focused on the upregulation of sugar metabolites in TMZ-sensitive NCH612 and investigated whether this was associated with TMZ resistance or sensitivity. I hypothesized that targeting glucose metabolism to deplete cancer cells of energy might sensitize the cells to TMZ.

Glucose analog 2-DG is a glucose molecule which has the 2-hydroxyl group removed, so that it cannot be metabolized like glucose. It has been used in various studies as an analog for glucose to investigate glucose transport and metabolism. It has been shown that combined with other potent cytotoxic agents, inhibitors of glycolysis could synergistically

eliminate cancer cells [96]. As 2-DG is relatively non-toxic and orally available, it is an attractive tool for potential therapies and, thus, has been tested in several clinical trials [97]. It seems that its most promising application may be as a synergistic agent in combination with other cytotoxic compounds [98].

I tested the efficacy of the glucose analog 2-DG in combination with TMZ in a soft agar colony formation assay in TS603, SU-AO3, NCH1681, and NCH612 (Figure 19). Contrary to our initial expectations, the results showed that the combination treatment of TMZ and 2-DG had a significant killing effect only in TS603, a TMZ-resistant line, with a significantly decreased colony number. In contrast, the other two resistant lines, SU-AO3 and NCH1681, showed no significant difference with or without 2-DG, and NCH612 showed a slight decrease in colony size with the addition of 2-DG, but the difference was not significant.

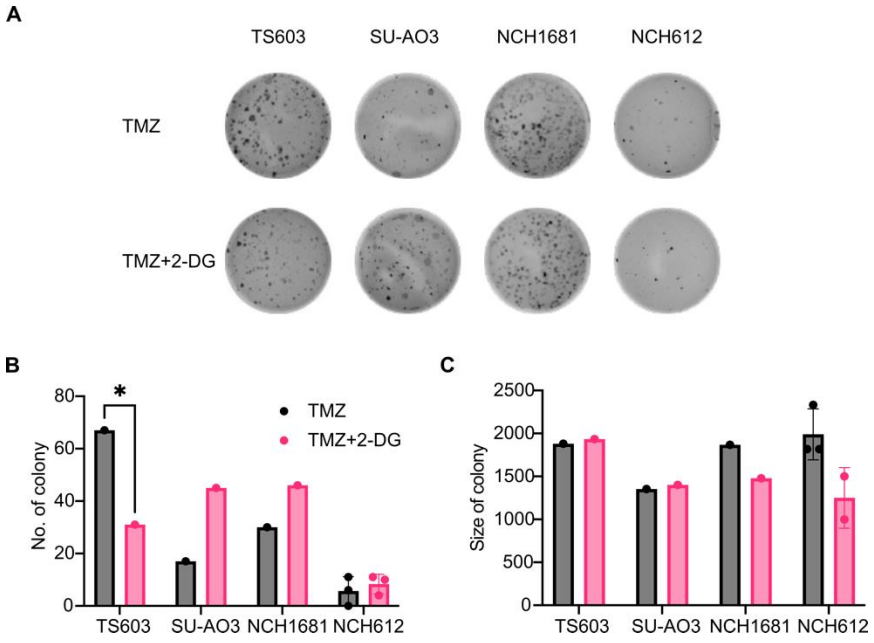

Figure 19. Effect of 2-DG and TMZ combination therapy.
(A) Representative images of colony formation in response to 2-DG and TMZ combination therapy in a soft agar assay. Five thousand cells were seeded in 24-well plates and grown for one week before treatment with 400 μM TMZ, 8 mM 2-DG, or the combination of both. Medium was refreshed weekly to provide adequate nutrients for cell growth. Colony formation was quantified after 20 days for TS603, 1 month for NCH1681, and 2 months for SU-AO3 and NCH612. (B-C) Quantification of colony number and size in response to TMZ or TMZ with 2-DG combination treatment, using ImageJ software. Note: D8375-10MG 2-Deoxy-D-Glucose solubility in water is 0.25g/5mL, which is equal to 300mM. A stock solution of 50mM was prepared initially. 8 mM 2-DG corresponds to 2.6% water.

The results of our study on 2-DG in combination with TMZ in various glioma PDTs have provided intriguing insights into the interplay between glucose metabolism and drug sensitivity. Our initial hypothesis was that the combination treatment of 2-DG and TMZ would have a synergistic effect and enhance the killing of glioma cells. However, the results showed that only the TMZ-sensitive cell line TS603 exhibited a significant decrease in colony number with the addition of 2-DG, while the other sensitive lines, SU-AO3 and NCH1681, showed no significant difference with or without 2-DG. Interestingly, the addition of 2-DG to the NCH612 cell line, which is resistant to TMZ, resulted in a slight decrease in colony size, but the difference was not significant.

The fact that only the TMZ-sensitive TS603 cell line responded to the combination treatment with 2-DG suggests that cells with low base levels of TCA metabolites may be more susceptible to this treatment regimen. The results also highlight the importance of considering the metabolic state of cancer cells in designing effective treatment strategies. Our findings provide a starting point for exploring the potential of glucose analogs in combination with chemotherapy drugs for the treatment of glioma and other cancers.

It has been observed that the inhibition of glycolysis is more effective in hypoxic conditions compared to normoxia, as cancer cells can utilize alternative sources like fatty acids or amino acids to produce ATP in normoxic conditions [99]. Therefore, it is advisable to repeat the experiments under hypoxic conditions to better understand the effects.

4.3.3 Combination treatment of carnitine inhibitor with TMZ

Based on our initial hypothesis that sensitive cell lines may increase their fatty acid intake to cope with drug-induced stress, I investigated the role of fatty acid metabolites as an alternative energy source in combination with TMZ treatment.

I compared the base level of fatty acid metabolites in all four PDTs. Surprisingly, NCH612, the most TMZ-sensitive cell line, had the highest baseline level of fatty acid metabolites compared to other cell lines (Figure 20), including the TMZ-resistant TS603 cell line, which had the lowest level. This unexpected result suggests that high baseline levels of fatty acid metabolites may indicate sensitivity to TMZ treatment rather than resistance. Therefore, considering the metabolic state of cells is crucial when designing combination therapies with TMZ.

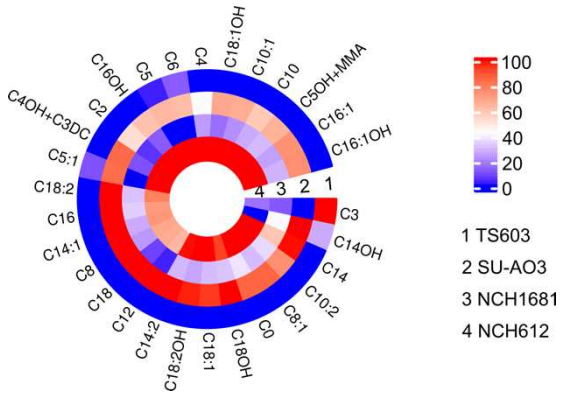

Figure 20. Baseline levels of fatty acids with different numbers of carbons.
The average level of each metabolite was normalized. The data was analyzed using Prism and plotted in an SRplot. The smallest value within the group was set to 0% and the largest value was set to 100% within each data set.

To further understand the mechanistic role of fatty acid metabolites in TMZ sensitivity, I plan to conduct additional experiments to explore the relationship between fatty acid metabolism and TMZ efficacy. Our hypothesis was that blocking the transportation of fatty acids into mitochondria could make cells sensitive to TMZ by disrupting the fatty acid energy supply. Fatty acids are transported into the mitochondria, where they undergo beta-oxidation to produce ATP, NADH, and FADH2 for ATP synthesis via oxidative phosphorylation.

I identified Mildronate, a drug that inhibits fatty acid transport into mitochondria, as a potential candidate for combination therapy with TMZ. Although it is primarily used to treat heart and blood vessel conditions, its potential as a cancer treatment has been investigated. I tested the combination efficacy of mildronate and TMZ to determine if targeting fatty acid metabolism could enhance the efficacy of TMZ in PDTs.

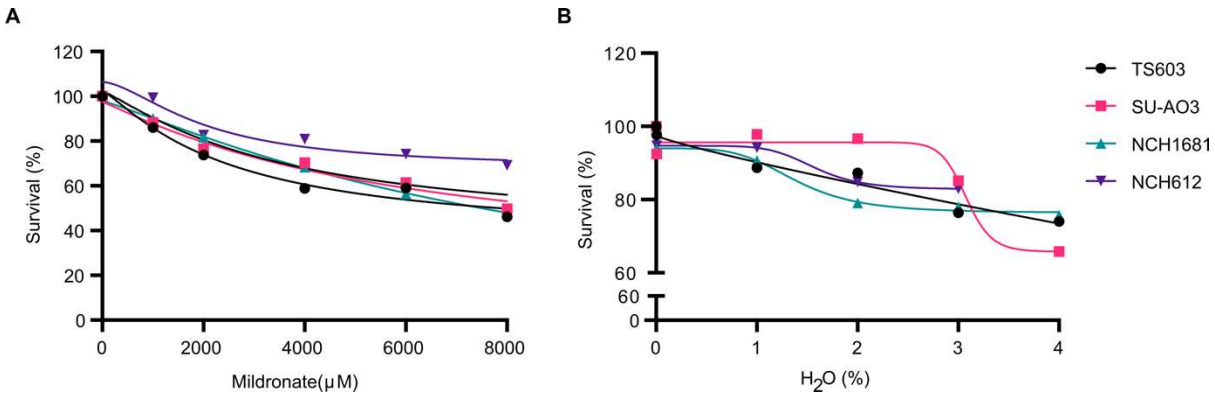

Figure 21. Dose response curve of Mildronate and water.
(A) dose response curve of Mildronate. (B) dose response curve of water.

Mildronate	TS603	SU-AO3	NCH1681	NCH612
Bottom	36,24	20,79	-11,79	67,79
Top	102,6	97,54	97,85	106,4
IC_{50}	2521	5954	9361	2031
HillSlope	-1,178	-1,080	-1,151	-1,638
$logIC_{50}$	3,402	3,775	3,971	3,308
Span	66,38	76,75	109,6	38,60

Table 5. IC_{50} values of Mildronate.

Water	TS603	SU-AO3	NCH1681	NCH612
Bottom	Unstable	65,78	76,38	82,81
Top	97,48	95,64	93,97	94,69
IC_{50}	42596	3,076	1,389	1,573
HillSlope	-0,8623	-24,39	-4,352	-6,680
$logIC_{50}$	4,629	0,4880	0,1426	0,1967
Span	Unstable	29,87	17,59	11,88
IC_{10}	Unstable	2.81	0.84	1.13

Table 6. IC_{50} values of water.

To assess cell sensitivity to Mildronate and determine the appropriate dosage for our in vitro experiments, I prepared the Mildronate stock 197 mM based on its maximum solubility of 29 mg ml^{-1} in water, which is 50 mg Mildronate dissolved in 1720 µL water.
Based on the dose response curve, the IC_{50} values of Mildronate for TS603, SU-AO3, NCH1681, and NCH612 were found to be 2521 mM, 5954 mM, 9361 mM, and 2031 mM, respectively (Figure 21 A, table 5).

I also measured the sensitivity of cells to water, and found that the IC_{50} values for SU-AO3, NCH1681, and NCH612 were 3.0 %, 1.4 %, and 1.6 %, respectively (Figure 21 B, table 6). The IC_{10} values for water in SU-AO3, NCH1681, and NCH612 were 2.8 %, 0.8 %, and 1.1 %, respectively, with equivalent Mildronate concentrations of 5600 mM, 1680 mM, and 2260 mM.

NCH1681 was particularly sensitive to water, with an EC_{80} of 1.01%, which is equivalent to Mildronate at 2000 mM. This restricts the use of Mildronate. The maximum concentration being used is 5000 mM, which is equivalent to 2.5% of water. For the purpose of calculating synergy, I assume that water has no effect on cell survival at this concentration

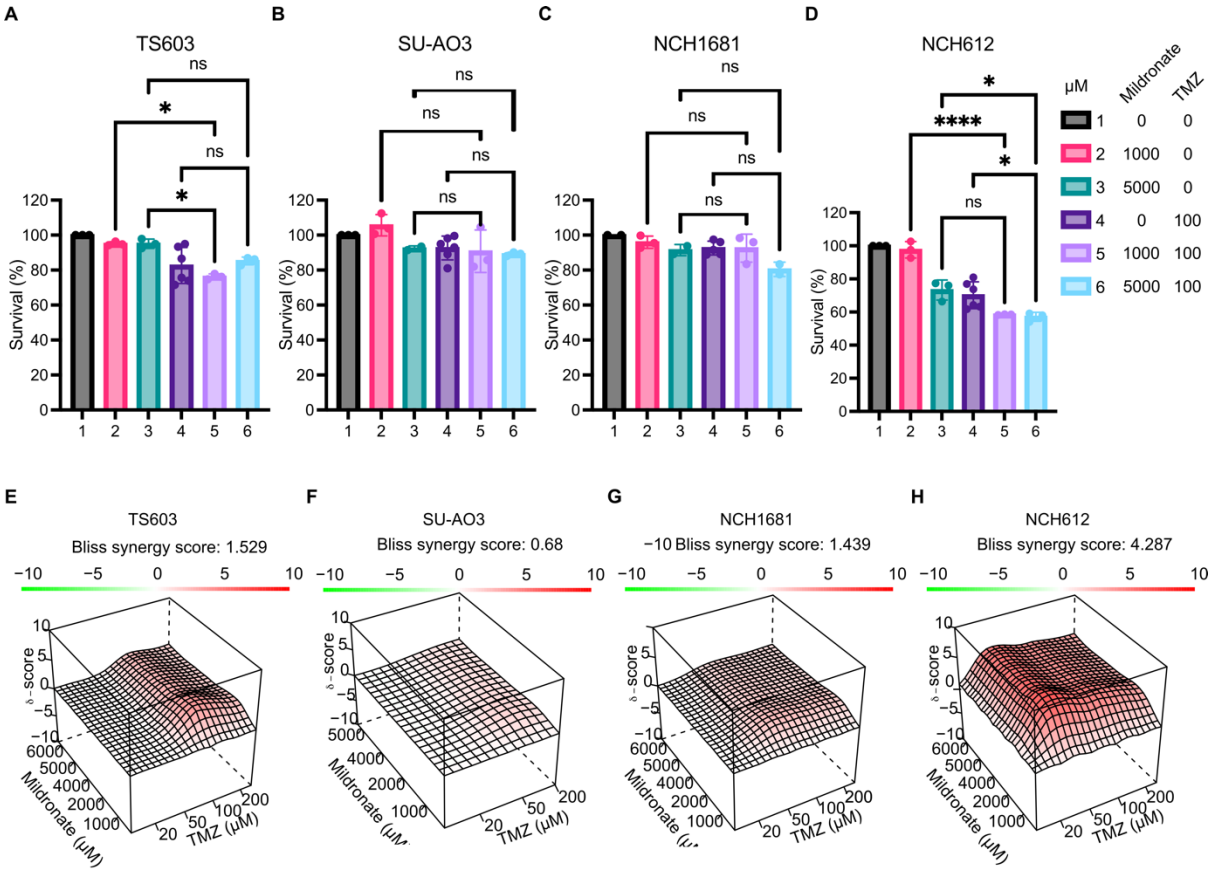

Figure 22. Combination Efficacy and Synergy of Mildronate and TMZ.
(A-D) Cell survival rate comparison between different combinations of Mildronate and TMZ in TS603, SU-AO3, NCH1681 and NCH612 cell lines. Data obtained from three biological repeats, each with three technical repeats. Data comparison with one-way ANOVA. (E-H) Synergy score of Mildronate and TMZ combination treatment on TS603 cell line calculated using SynergyFinder 2.0.

I evaluated the effect of combining different concentrations of mildronate (5000 μM and 1000 μM) with two different concentrations of TMZ (100 μM and 400 μM) on cell survival. After 96 hours of treatment, there was no significant difference in the survival of the combination treatment or single treatment in TS603, SU-AO3, and NCH1681, except for NCH612, where the combination treatment of 5000 μM mildronate and 100 μM TMZ resulted in lower survival (Figure 22 A, B, C and D). I then calculated the synergy score using the IC50s of mildronate and TMZ, as well as the survival data of the three combinations. The Bliss model was used to determine the synergy score using Combenefit and SynergyFinder 2.0 C. The synergy scores for TS603, SU-AO3, NCH1681, and NCH612 were 1.53, 1.44, 0.68, and 4.287, respectively.

Our experiments showed that the combination of mildronate and TMZ did not significantly increase cell death in most of the tested cell lines, except for NCH612. This suggests that the combination of mildronate and TMZ may not be a highly effective treatment strategy.

Interestingly, I observed that NCH612, which has the highest baseline levels of fatty acids, and also increased fatty acid level upon TMZ treatment, showed the strongest additive effect between mildronate and TMZ. This finding suggests the observed upregulation of fatty acids contribute parts to TMZ resistance.

Our study has several limitations, including the fact that I only tested a small number of cell lines and that our in vitro findings may not necessarily translate to *in vivo* settings. Additionally, It may also be useful to explore alternative approaches for targeting fatty acid metabolism, such as inhibitors that target enzymes involved in fatty acid synthesis or oxidative phosphorylation. Finally, more research is needed to understand the mechanisms underlying the observed effects of mildronate and TMZ combination therapy in NCH612 cells, and to determine why these findings can or cannot be extrapolated to other cell lines or subtypes. These findings highlight the complexity of metabolic adaptations to drug-induced stress and suggest that a more comprehensive understanding of metabolic rewiring in response to drug treatment is needed.

4.4 Investigating epigenetic approaches to overcome TMZ resistance

The contributions of mutant IDH to DNA methylation, histone methylation and the G-CIMP phenotype coalesce to maintain glioma cells in a self-renewing dedifferentiated state, thus, IDH-mutant gliomas are ideal candidates for epigenetic therapies.

Our previous work has demonstrated that non-cytotoxic, epigenetically targeted DNMT (DNA methyltransferase) inhibitor DAC can result in the reversal of DNA methylation marks induced by IDH1 [100]. To test the hypothesis that TMZ resistant cells may be sensitive to DAC treatment or that DAC treatment can restore sensitivity to TMZ, I aimed to investigate cell survival by directly combining DAC and TMZ or pre-treating cells with DAC before subjecting them to TMZ treatment.

4.4.1 Efficacy of DAC and TMZ combination therapy

In order to assess the combination efficacy and synergy of DAC and TMZ, I conducted an MTT survival assay to test the efficacy of DAC in our IDH1 mutant PDTs. I seeded 1000 cells in 100 µL medium in 96-well plates and the following day, I added 50µL of medium containing different concentrations of DAC to create a concentration gradient ranging from 0-2000 nM. After 96 hours of treatment, I measured the MTT reading and normalized the survival percentage to the highest DMSO treatment well, which contained 0.002% DMSO, equivalent

to the DMSO content of 2000 nM DAC. Based on the "inhibitor vs. response - variable slope (four parameters)" analysis of the dose-response curve, the IC_{50} values for TS603, SU-AO3, NCH1681, and NCH612 cell lines were calculated to be 73.89 nM, 135.3 nM, 563.2 nM, and 134.9 nM, respectively (Figure 23A). However, due to the undetermined 95% CI (profile likelihood) for this data set, I cannot confidently conclude the calculated IC_{50} values.

Based on the MTT assay analysis, I chose a DAC concentration of 500 nM for combination treatment, as the survival rate did not significantly decrease beyond this concentration. I then treated the cells with varying concentrations of TMZ in combination with 500 nM DAC for 96 hours and measured cell survival using the MTT assay.

Our results showed that the MTT reading obtained from the combination treatment of 0.5 μM DAC and TMZ are not significantly different from those obtained from the DMSO control with TMZ combination across all concentrations of TMZ in SU-AO3 and (Figure 23 D, F). In the case of TS603, a slight difference was observed only at a TMZ concentration of 50 μM (Figure 23C). While NCH1681 exhibited a reading difference at 50 μM and 100 μM TMZ concentration (Figure 23E).

To determine whether the drug combination has any benefit, I used the Bliss model in Combenefit to analyze the synergy based the dose-response data of TMZ, DAC, and the drug combination survival data. In this model, two drugs elicit their effects independently with a stochastic process, a synergy score below -10 indicates antagonism, a score above 10 indicates synergy, and a score between -10 and 10 represent additive effect. Our results showed that in TS603, the synergy score between DAC and TMZ was 14, 16 and 16 at TMZ concentration of 20 μM, 50 μM and 100 μM, respectively, when combined with 500 nM DAC. In NCH1681, a synergy score of 12 was observed at 20 μM TMZ with 500 nM DAC combination, but there was antagonism between DAC and TMZ at higher TMZ concentrations (400 μM) with a synergy score of -16. Surprisingly, I observed strong antagonism between 500 nM DAC and 0-200 μM TMZ in SU-AO3 and NCH612, with the synergy score ranging from -22 to -13. Specifically, in SU-AO3, the synergy score was -22, -14, -22 and -13 at TMZ concentration of 20 μM, 50 μM, 100 μM and 200 μM, respectively. In NCH612, the synergy score was -14, -13 and -13 at TMZ concentration of 20 μM, 50 μM and 100 μM, respectively.

In summary, while TS603 and NCH1681 showed slight additive effect between DAC and TMZ, SU-AO3 and NCH612 showed strong antagonism.

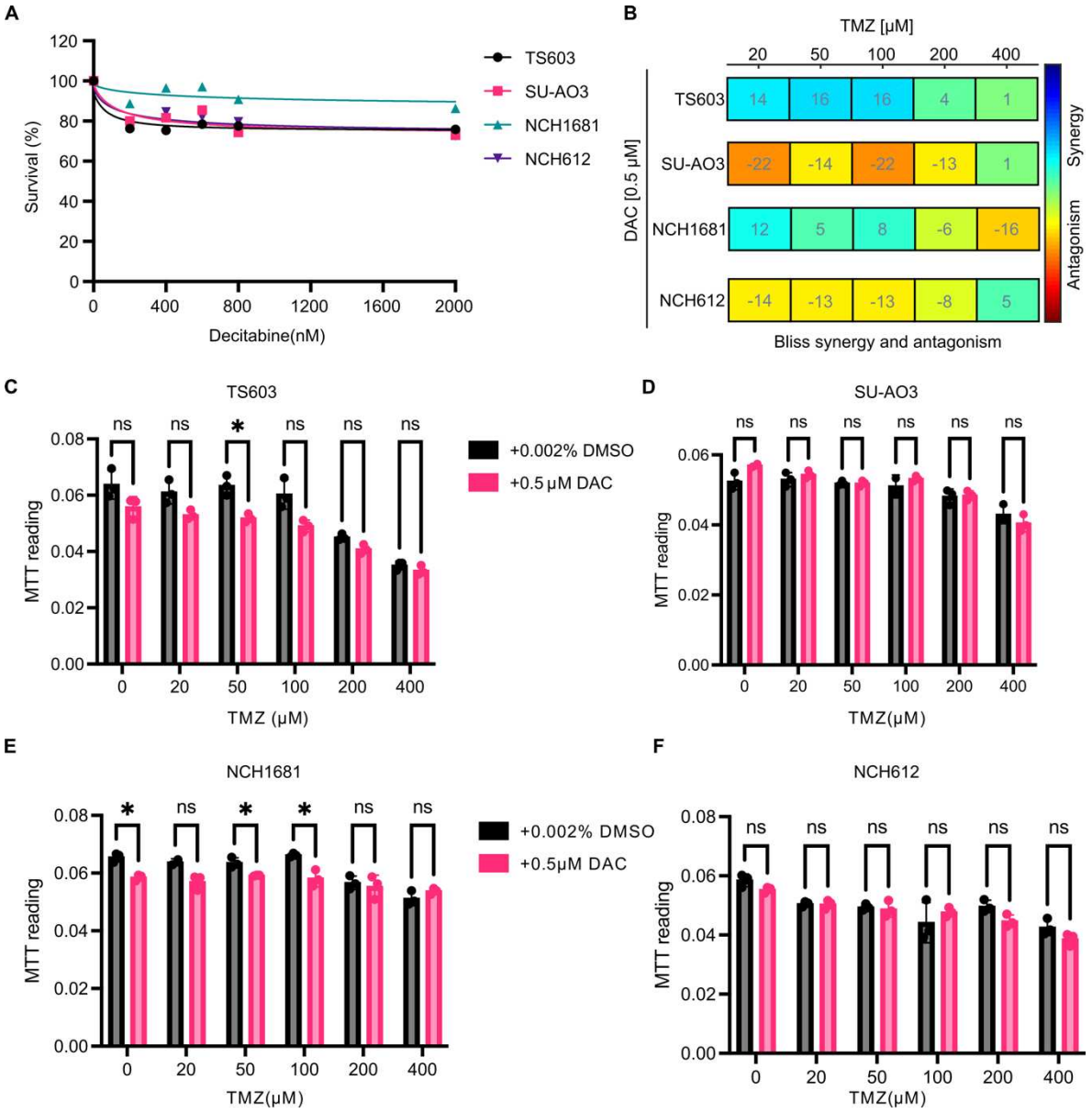

Figure 23. Combination efficacy and synergy of DAC and TMZ.
(A) Dose-response curve of DAC in four IDH1mut PDTs with each dot representing the average of three technical repeats. (B) Bliss synergy and antagonism score with 500nM DAC and different concentrations of TMZ in PDTs from Combenefit. (C-F) MTT reading of 0.5 μM DAC or 0.002% DMSO control with different combinations of TMZ, with data comparison using unpaired t test.

4.4.2 Synergistic efficacy of pre-treatment with DAC followed by TMZ treatment

Building upon our findings from assessing the combination efficacy and synergy of DAC and TMZ, I investigated the potential synergistic efficacy of pre-treating cells with DAC followed by TMZ treatment. I aimed to determine whether this pre-treatment model would yield different results in terms of cell survival compared to the direct drug combination model. Our

goal was to explore the possibility of enhancing the efficacy of TMZ treatment through pre-treatment with DAC.

I treated cells with 500 nM DAC as a pre-treatment and then subjected them to different concentrations of TMZ (0-400 μM). To conduct the experiment, I plated 300,000 cells in 2 mL medium on laminin-coated 6-well plates to facilitate medium changes and drug refreshing. I exchanged the medium daily with 500 nM DAC or 0.0005% DMSO, harvested the cells after 96 hours of treatment, and counted them with trypan blue. Afterward, 2000 cells from the pre-DAC or pre-DMSO treated PDTs were seeded in separate 96-well plates for subsequent combination treatment TMZ (0-400 μM) using the MTT assay. To compare the results, I used cell number standard of 0, 400, 800, 1200, 1600, 2000. By comparing the MTT readings from the cell number standard, I observed around a 50% decrease in the MTT reading from TS603, a 45% decrease from SU-AO3, a 25% decrease from NCH1681, and a 69% decrease from NCH612 cell lines compared to the DMSO pre-treated cell number standard reading. These readings represent subsequent continuous death after pre-DAC treatment, which showed the efficacy of DAC treatment alone on those PDTs (Figure 24 A, B, C, D). This experiment was repeated three times biologically, with each repeat consisting of three technical repeats. I have present the actual MTT reading rather than the survival rate for direct comparison.

From the results, I observed a decrease in MTT reading after Pre-DAC treatment compared to the DMSO pre-treated samples in TS603, NCH1681 and NCH612 (Figure 24 A, C, D), except for SU-AO3 (Figure 24B), in which there was no significant reading difference between the pre-DMSO control-treated, and pre-DAC treated samples. These results indicate that a better combination regime between DAC and TMZ is pre-DAC treatment followed by TMZ treatment, which provides more benefits than a direct combination of the two drugs.

I used Combenefit to calcualte the synergy score, assuming that 0.0005% DMSO had no effect on cell death. Therefore, I normalized the survival of DAC pretreated cell survival by comparing it with the DMSO-pre-treated sample for the synergy cell survival. Surprisingly, strong synergy between DAC and TMZ was observed in all four IDH1 mutant PDTs (Figure 24 E). At TMZ concentration of 20-200 μM, TS603, SU-AO3, and NCH612 exhibited synergy scores of approximately 20-37. In TS603, the synergy score was 37, 34, 28, and 21 at TMZ concentrations of 20 μM, 50 μM, 100 μM, and 200 μM, respectively. In SU-AO3, the synergy score was 21, 21, 16, and 12 at TMZ concentrations of 20 μM, 50 μM, 100 μM, and 200 μM, respectively. In NCH612, the synergy score was 23, 19, 15, and 11 at TMZ concentrations of

20 μM, 50 μM, 100 μM, and 200 μM, respectively. Although NCH1681 showed less synergy, it still with a synergy score of 10.

To further validate the synergistic effect between pre-DAC treatment and TMZ combination, I investigate the effectiveness of pre-DAC treatment followed by TMZ treatment on softagar colony formation. I treated TS603, SU-AO3, and NCH1681 with daily 500 nM DAC in 800 μL medium for 7 days, followed by the addition of 400 μM TMZ in 800 μL medium for 4 days, both drugs were refreshed daily. TS603, SU-AO3, and NCH1681 cells were seeded in 24-well plates with 5000 cells and treated after one week of seeding. The control group was treated with the same regime using 0.002% DMSO for DAC control for 7 days, followed by 0.4 % DMSO as control for TMZ for another 4 days. The cells were then allowed to grow for around 2 months before images were taken and analyzed. However, the softagar colony formation assay showed no difference in colony size or number between DAC treatment alone and pre-DAC treatment followed by TMZ in TS603, SU-AO3 and NCH1681 (Figure 24 F, G H), indicating that this combination regime may not be effective in this assay.

The difference between the high synergy score observed in the MTT assay and the lack of effect in the soft agar assay may be due to the use of high concentrations of DAC and TMZ in the soft agar assay. As per the Bliss model, the synergistic effect is primarily observed at lower concentrations of TMZ, and the extent of synergy decreases considerably with 400 μM TMZ treatment.

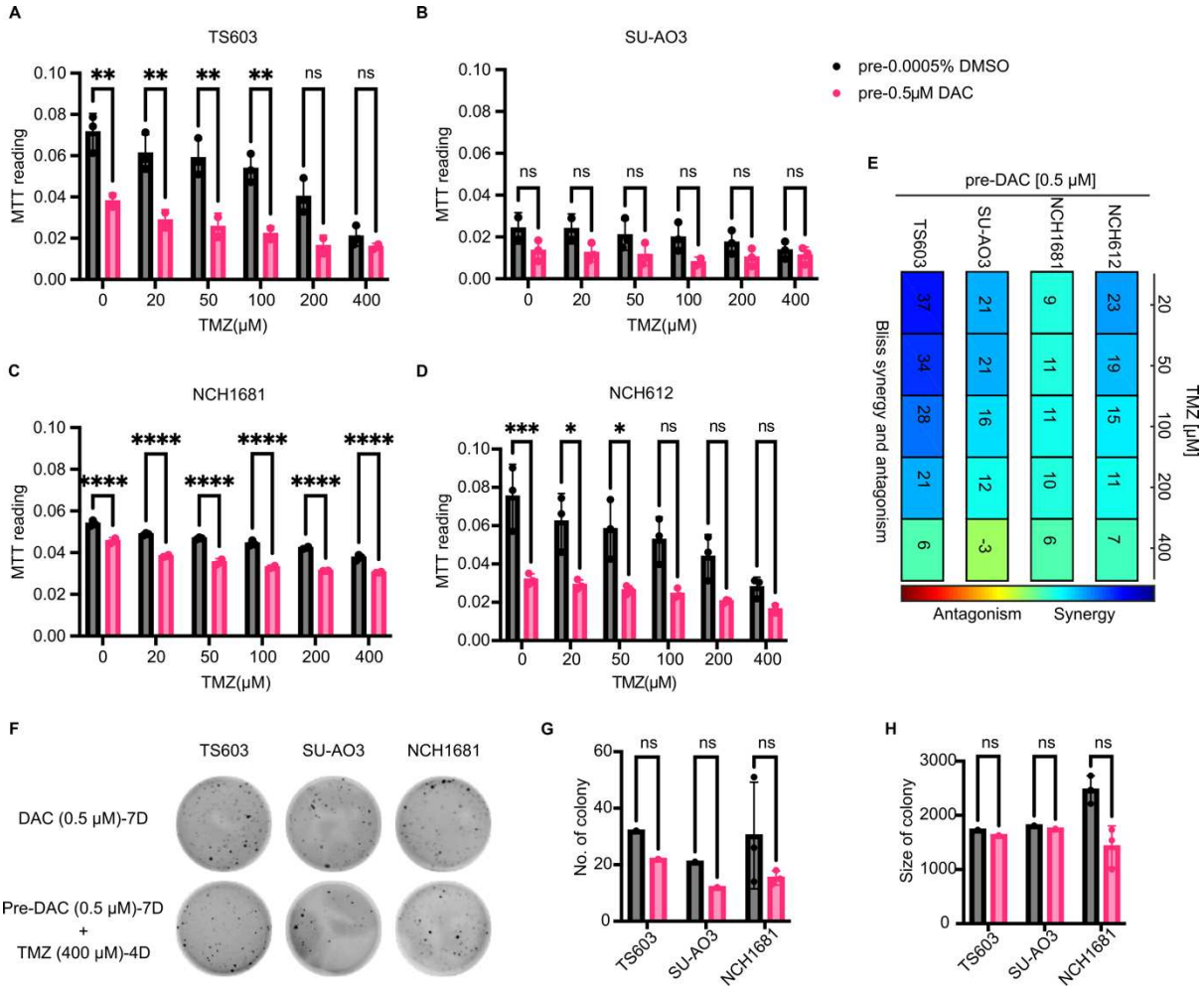

Figure 24. Synergistic efficacy of pre-treatment with DAC followed by TMZ treatment. (A-D) Comparison of MTT readings of TMZ response in 0.0005% DMSO and 0.5 μM DAC 96h pretreated PDTs. (E) Synergy score in four PDTs from Bliss synergy model from Combenefit. The survival of each concentration combination is calculated from the average MTT reading from A-D, survival is normalized to 0.0005% DMSO pretreated sample without TMZ treatment. (F) Softagar colony formation comparison between DAC treated alone and pre-DAC treatment followed by TMZ treatment regime. 5000 cells were seeded in 24-well plates and subject to daily 500 nM DAC treatment for 7 days, followed by another 4 days of daily 400 μM TMZ treatment. G. Quantification of colony number from F using two-way ANOVA. (H) Quantification of colony size from F using two-way ANOVA.

To compare the efficacy of direct DAC and TMZ combination regime with the Pre-DAC treatment regime followed by TMZ treatment, I calculated the synergy scores based on the concentrations I have tested. I submitted the mean results obtained from the bliss model from Combenefit to Synergy Finder 2.0. I obtained the synergy scores in TS603, SU-AO3, NCH1681, and NCH612 for the direct combination regime of DAC and TMZ, which were 2.171, 2.77, 0.69, and 2.17, respectively (Figure 25 A, C, E, G). Pre-DAC followed by TMZ

yielded higher synergy scores of 6.46, 7.60, 5.85, and 7.19, respectively (Figure 25 B, D, F, H). The 2D and 3D plots show the synergy scores between DAC and TMZ at different concentrations, with higher scores indicating stronger synergy. The pre-DAC treatment regime followed by TMZ treatment shows higher synergy scores compared to the direct combination regime, indicating that it may be a better treatment option. Additionally, the strongest synergy areas were observed at low DAC and low TMZ concentrations in all PDTs.

In conclusion, pre-treatment with DAC followed by TMZ treatment showed promising results in enhancing the efficacy of TMZ in resistant cells. The synergy between DAC and TMZ was strong, particularly at lower TMZ concentrations

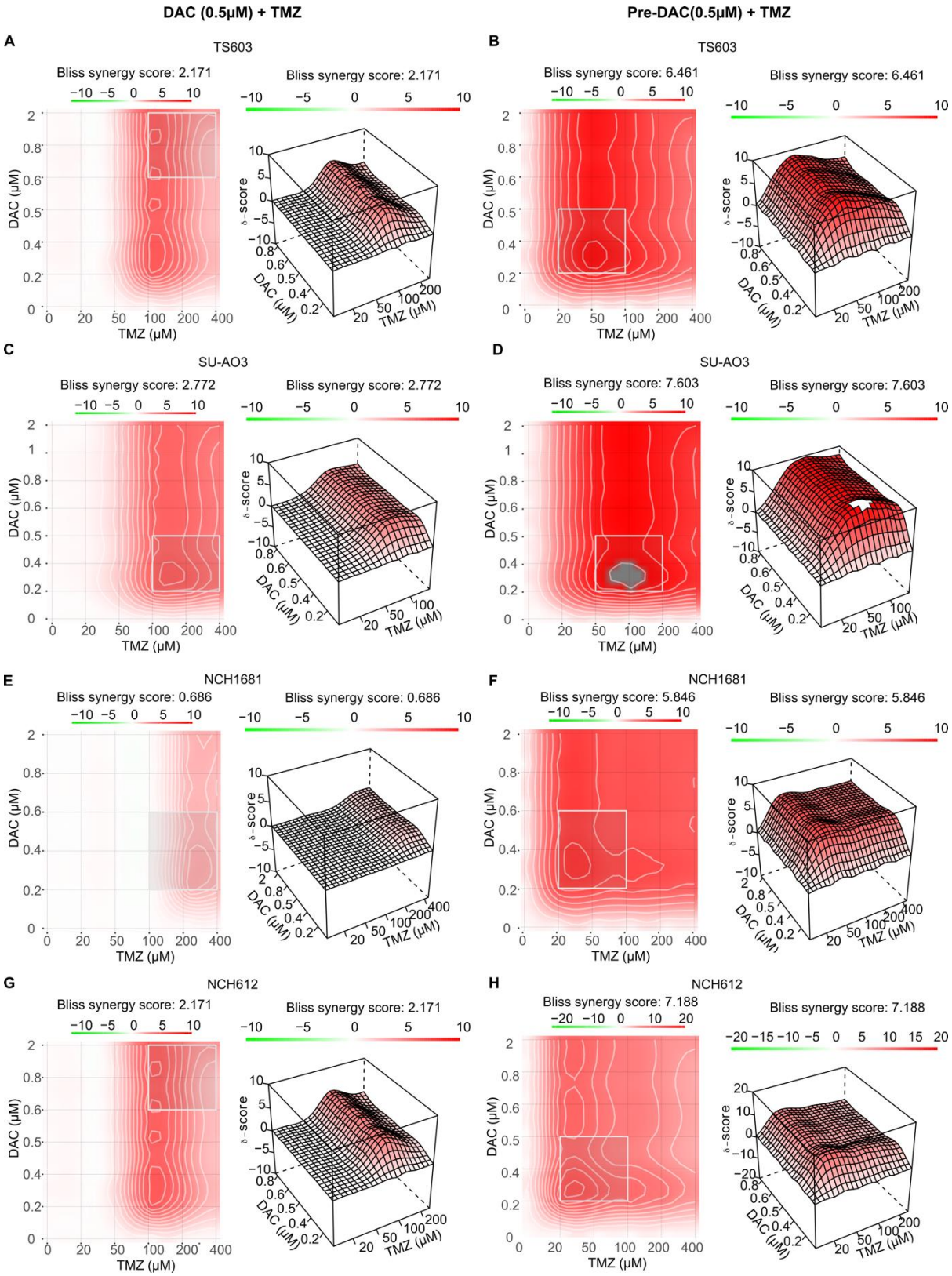

Figure 25. Synergy comparison of DAC versus pre-DAC treatment followed by TMZ treatment. (A, C, E, G) Bliss synergy plot in 2D and 3D from direct combinations of DAC and TMZ treatment. (B, D, F, H) Bliss synergy plot in 2D and 3D from pre-DAC treatment followed by combination with TMZ in TS603, SU-AO3, NCH1681 and NCH612 cell lines, respectively.

4.4.3 Pathway enrichment analysis following pre-DAC and TMZ treatment

Based on the potential of the pre-treatment with DAC followed by TMZ combination regime, I aimed to optimize the treatment by adjusting the concentration and duration of each drug. Given the observation of higher synergy scores at lower concentrations of TMZ and DAC, I lowered the concentration of both drugs. WI chose to use a three-day treatment regimen of DAC as it is commonly used in clinical practice, providing sufficient drug exposure for DNA demethylation and reactivation of tumor suppressor genes while minimizing toxicity and allowing for normal cell recovery between cycles. Therefore, our optimized treatment involved a 3-day pre-treatment of 100 nM DAC followed by 4 days of 100 μM TMZ.

To evaluate the efficacy of this optimized regimen, I conducted a soft agar assay. For the soft agar assay, I seeded 10,000 cells from TS603, NCH1681, NCH612, and 15,000 SU-AO3 in 12-well plates, each with two technical repeats. After one week of recovery, cells were treated with either 100nM DAC or 0.001% DMSO in 2mL medium with daily refreshing of new drugs for three days, followed by TMZ 100μM for 4 days. Alternatively, wells were treated with either DAC regime or TMZ regime alone for comparison. The control and treated wells followed the same treatment regime. After one week of treatment, colonies were allowed to form, and medium was exchanged weekly based on the growth of the colony. After one and a half months of growth, the colonies were stained with 0.005% crystal violet, and images were taken and normalized using Image J. However, images for NCH612 were not shown due to technical issues, resulting in no colony formation at this treatment regime. Surprisingly, data from TS603, SU-AO3 and NCH1681 showed no difference in colony number or size for DAC treatment versus DAC pre-treatment, contrary to our expectations (Figure 26).

The unexpected results of our soft agar assay suggest that the concentration and duration of each drug may still need to be adjusted to achieve the desired outcome. To gain a deeper understanding of the molecular and biological changes that occur in response to the treatment regime, I performed RNA analysis to identify potential targets or pathways that are affected, which may aid in refining the treatment regime and identify potential therapeutic targets.

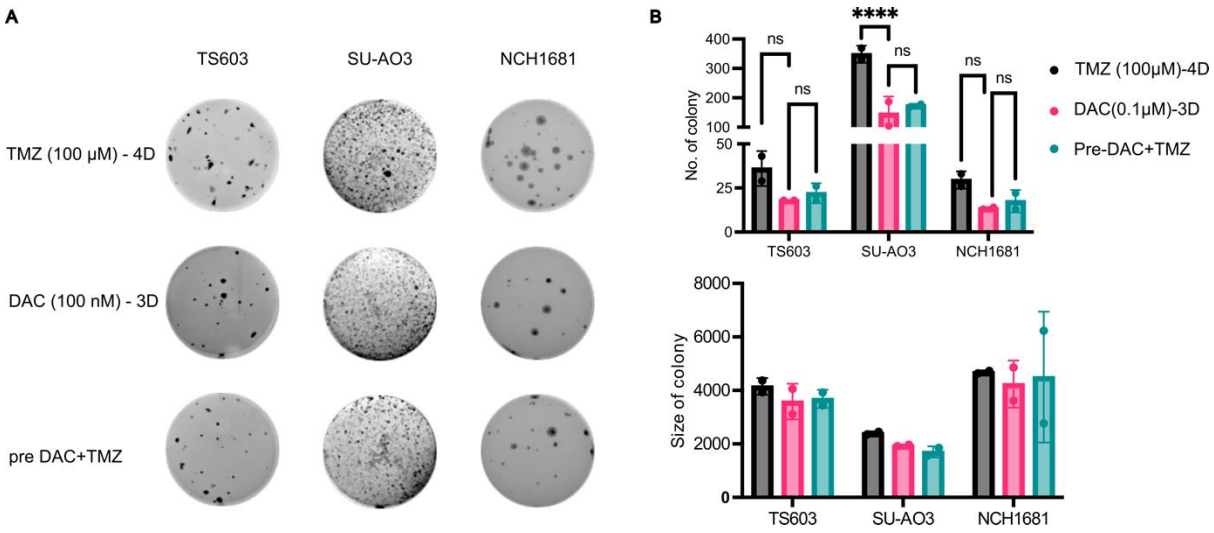

Figure 26. Adjusted pre-DAC and TMZ treatment regimes.
(A) Representative image of soft agar colonies following treatment with either 100 nM DAC and 100 μM TMZ for 3 and 4 days, respectively, or with DAC or TMZ alone. 10,000 cells from TS603, NCH1681, NCH612, and 15,000 SU-AO3 were seeded in 12-well plates with two technical repeats. (B) Comparison of colony number and size between the TMZ, DAC, and pre-DAC plus TMZ treatment regimens shown in panel A. Data were analyzed using Image J, and comparisons were made using a two-way ANOVA.

To ensure consistency with the soft agar assay, I utilized the same treatment regime for RNA-seq analysis. I seeded 500,000 cells in 2 mL medium of TS603, NCH1681, and NCH612 in laminin-coated 12-well plates. The cells were treated with 100nM DAC or 0.001% DMSO in 2mL medium with daily refreshing of new drugs for three days, followed by TMZ 100μM for 4 days. After treatment, cells were harvested, washed with cold PBS, and RNA was extracted. The extracted RNA was stored at -80°C until being sent for HiSeq 4000 single-read analysis.

For the RNA-seq analysis, I employed a significance cutoff of -log10 (adjusted p value) ≥ 1.5 and log2 fold change ≥ 1.5 or ≤- 1.5 for upregulation and downregulation, respectively. I first compared the gene expression changes induced by DAC, TMZ alone, and the pre-DAC treatment followed by TMZ treatment regime within each PDT (Figure 27 A, B, C). In TS603, treatment with DAC alone resulted in 65 downregulated genes and 367 upregulated genes. However, pre-DAC treatment followed by TMZ treatment showed a significant increase in the number of upregulated genes, with 36 genes downregulated and 626 genes upregulated. Similar trends were observed in NCH1681 and NCH612. In NCH1681, treatment with DAC alone resulted in the downregulation of only one gene and upregulation

of 105 genes. Pre-DAC treatment followed by TMZ treatment caused downregulation of 11 genes and upregulation of 451 genes. In NCH612, treatment with DAC alone resulted in 108 downregulated genes and 214 upregulated genes, while pre-DAC treatment followed by TMZ treatment resulted in 104 downregulated genes and 798 upregulated genes. The significant increase in the number of upregulated genes observed in all three cell lines with the pre-DAC and TMZ treatment regime compared to DAC or TMZ alone suggests a potential synergistic effect of the combination treatment. This may indicate that the pre-treatment with DAC could have a priming effect on the cells, making them more responsive to the subsequent TMZ treatment.

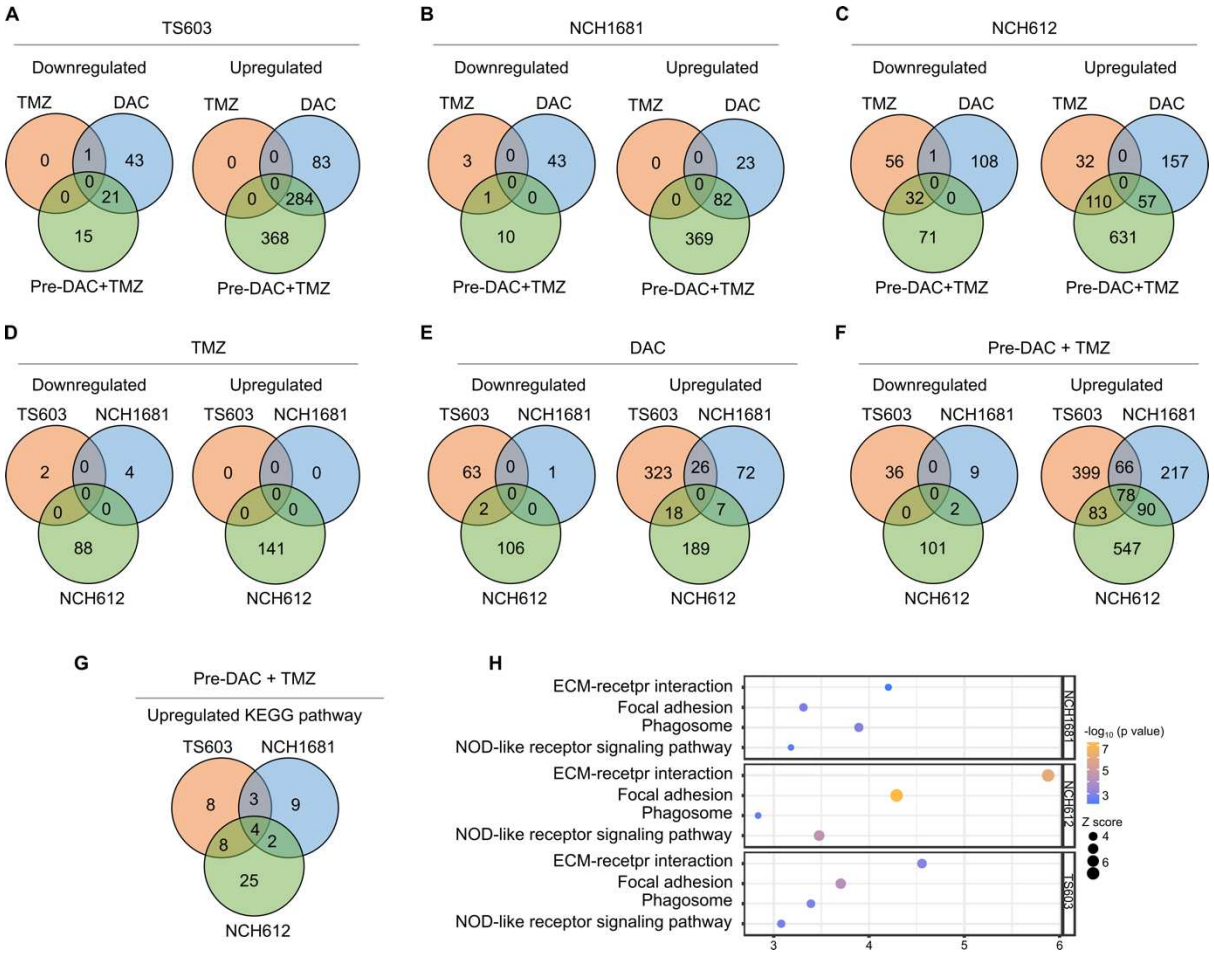

Figure 27. Pathway analysis of RNA-seq data from pre-DAC and TMZ treatment regimen.
(A-C) Venn diagram showing the commonly altered genes induced by DAC, TMZ alone, and the pre-DAC treatment followed by TMZ treatment regime within each PDT. (D-F) Venn diagram showing the up- and downregulated genes shared across the three treatment groups (TMZ, DAC alone, and pre-DAC plus TMZ inTS603, NCH1681 and NCH612. (G) Venn diagram showing the commonly upregulated KEGG pathway in common in TS603, NCH1681 and NCH612. (H) dot plot of the four commonly upregulated KEGG pathways inTS603, NCH1681 and NCH612, figure plot from SRplot.

I then compared the up- and downregulated genes shared across the three treatment groups (TMZ, DAC alone, and pre-DAC plus TMZ) to identify potential universal responsive genes for each drug treatment. I found that there were no commonly shared alterations in the first two treatment groups (Figure 27 D, E). However, in the pre-DAC plus TMZ treatment group (Figure 27 F), I observed a set of 78 genes that were commonly upregulated in TS603, NCH1681, and NCH612. I submitted these 78 genes for KEGG pathway analysis and found that only one pathway was enriched - Platelet activation, with a -log10 P value of -2.5. In cancer, platelet activation and aggregation can also promote tumor growth, invasion, and metastasis by facilitating the interaction of cancer cells with the blood vessel walls and helping them evade the immune system.

The upregulation of the platelet activation pathway may reflect an adaptive response to the drug treatment. It is possible that the activation of this pathway is a protective mechanism that enable the cells to cope with the stress of the treatment and potentially limit the damage caused the drugs. As such, pre-DAC followed by TMZ treatment may present new opportunities for targeting platelet activation pathway as a potential therapeutic strategy.

By analyzing the KEGG pathways enriched in each PDTs following the pre-DAC followed by TMZ treatment regime, I identified 23 enriched KEGG pathway in TS603, 18 in NCH1681 and 39 in NCH612 (Figure 27 G). Out of these pathways, four KEGG pathways were commonly enriched in all three. These pathways include Focal adhesion, ECM-receptor interaction, Phagosome and NOD-like receptor signaling pathway (Figure 27 H). These pathways play important roles in cellular processes such as cell adhesion, extracellular matrix remodeling, endocytosis, and immune response. They have been previously implicated in cancer development and progression, and their dysfunction has been associated with poor prognosis. Interestingly, these pathways have also been reported to be involved in drug resistance mechanisms in cancer cells.

The KEGG pathway enrichment analysis of the 78 genes shared in all three PDTs and the individual analysis of each PDT resulted in different commonly altered pathways. While Focal adhesion, ECM-receptor interaction, Phagosome and NOD-like receptor signaling pathways are not directly related to platelet activation pathway, they do share some common features. Focal adhesion pathway plays a role in cell adhesion and migration, and it involves the interaction between integrins and extracellular matrix components such as collagen and fibronectin. ECM-receptor interaction pathway, on the other hand, is involved in cell adhesion and communication with the extracellular matrix. Phagosome pathway is involved in the internalization and degradation of extracellular particles and microorganisms. NOD-

like receptor signaling pathway, on the other hand, is involved in the regulation of the innate immune response to pathogens. All these pathways share a common feature of cellular interactions with the extracellular environment. Similarly, platelet activation pathway involves platelet adhesion, activation, and aggregation in response to various stimuli, including the extracellular matrix components and inflammatory mediators. Therefore, these pathways share common features of interactions with extracellular components and processes involved in cell adhesion and immune response. These findings emphasize the significance of targeting interactions with extracellular interactions and process for new therapeutic approaches.

Integrins are a family of 24 heterodimeric cell surface receptors that participate in signal transduction involved in many cellular processes. They also mediate cellular communication within the extracellular matrix during adhesion, motility, migration, invasion and angiogenesis. Integrins avß3 and avß5 are identified as preclinical therapeutic targets in GBM. Cilengitide is a selective integrin inhibitor targeting avß3 and avß5, which its currently under evaluation of phase II trial in rGBM [14, 59]. Given these encouraging developments, it is worthwhile to consider exploring the potential of Cilengitide in our tumor models.

4.5 FDA approved drug repurposing for IDH1-mutant TMZ resistant PDTs

This section draws on our publication [88] with some modifications.

4.5.1 FDA-approved drug screening pipeline using high-throughput droplet microarray (DMA)

To overcome the challenges encountered in identifying optimal drug targets and treatment combinations with TMZ, I collaborated with Prof. Levkin, Dr. Anna A. Popova, Dr. Haijun Cui from the Institute of Biological and Chemical Systems-Functional Molecular Systems at the Karlsruhe Institute of Technology (KIT) to conduct a high-throughput drug screening of FDA-approved compounds using the DMA platform (Figure 28).

The DMA platform is a miniaturized chip that consists of hundreds of nanoliter droplets, each with the volume determined by the size of hydrophilic spots surrounded by superhydrophobic barriers (Figure 28 A). The DMA slides contained 588 square hydrophilic sports (1mm x 1mm), and anti-cell adhesion solution to the hydrophilic spots of DMA was applied to prevent cell adhesion to the bottom surface of the array.

2208 FDA-approved drugs at a concentration of 5μM and 2 nL per spot with five replicates were printed on DMA, with DMSO as the control group (Figure 28 A). The outer rows were excluded from the drug screening due to the edge effect. Each slide contained 92 drugs and 1 DMSO control, and a total of 24 DMA slides were used in the drug screening process. 300 nL of culture medium containing 300 cells of TS603 and NCH1681 were seeded in the hydrophilic spot of DMA. Using the hanging drop method, a single-spheroid array on the DMA against them were created (Figure 28 B). This part of the experiment was conducted by Haijun Cui.

Cell viability was assessed using an automated microscope, which captured fluorescence images of the spheroids stained with calcein AM for live cells and propidium iodine (PI) for dead cells (Figure 28 C). The images were analyzed to determine the ratio of live cells to total cells (live + dead). The percent viability of each drug-treated spheroid is normalized to the viability of DMSO-treated spheroids and averaged the percent viability data in five replicates. Drugs that reduced viability to less than 50% were considered as effective compound candida. This part of the experiment was conducted by Marcel Schilling and Markus Reischl.

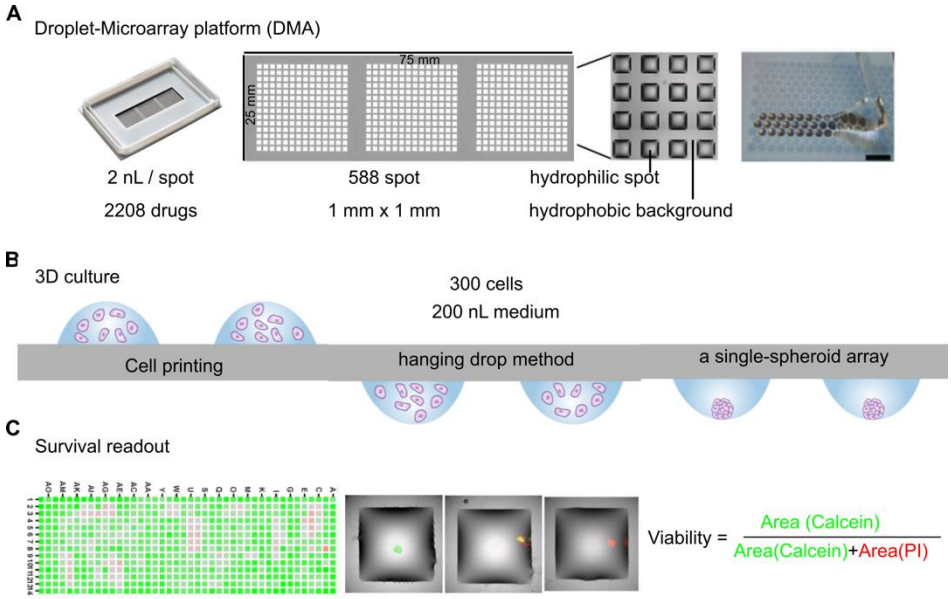

Figure 28. High-throughput drug screening pipeline using DMA.
(A) DMA platform with 588 hydrophilic spots (1mm x 1mm). 2208 FDA-approved drugs with 2 nL per spot were printed. (B) Hanging drop method for single-spheroid array formation on DMA. Each spot is printed with 200 nL medium containing 300 cells. (C) Computer-based readout of DMA slides for measuring cell viability. Figure A has been adapted from the official website of the Levkin research group (https://www.levkingroup.com/index.php/miscellaneous/pictures-and-videos). Figure B and Figure C have been modified from images provided by Haijun Cui.

4.5.2 Hit compound identification and validation

Using the drug screening pipeline and quantification criteria established in section 5.1, 22 hit compounds for NCH1681 and 29 hit compounds for TS603, with 10 compounds shared between them were identified (Figure 29 A).

In order to validate the generality of these drug candidates and to exclude any cell-specific results, I included two additional PDTs, NCH612 and SU-AO3 and tested whether the candidate compounds induced cell killing using MTT assay in a 96-well format (Figure 29 B). I seed 1000 to 5000 cells in 100 µL of medium into each well of a 96-well plate. The next day, I added 50 µL medium containing drugs to achieve the desired final concentration as designed. The outer rows were seeded with 100 µL of PBS to reduce the evaporation of inner walls and reduce the edge effect. After 96 hours of incubation, I measured MTT readings and adjusted them by subtracting the background reading obtained from wells containing only medium but without cells. For Verteporfin (VP), due to its autofluorescence, we set a color background at each concentration by adding different concentrations of VP to wells containing only medium but no cells. I then normalized the survival percentage of each treatment well to that of the non-treated wells based on the adjusted reading. The IC_{50} values were calculated using the GraphPad Prism software, based on the [inhibitor] vs. response variable slope (four parameter) equation derived from the dose-response curve. From the list of candidate compounds, I selected 10 drugs, and all four PDTs showed sensitivity to these drugs with IC_{50} below 1µM (Figure 29 B).

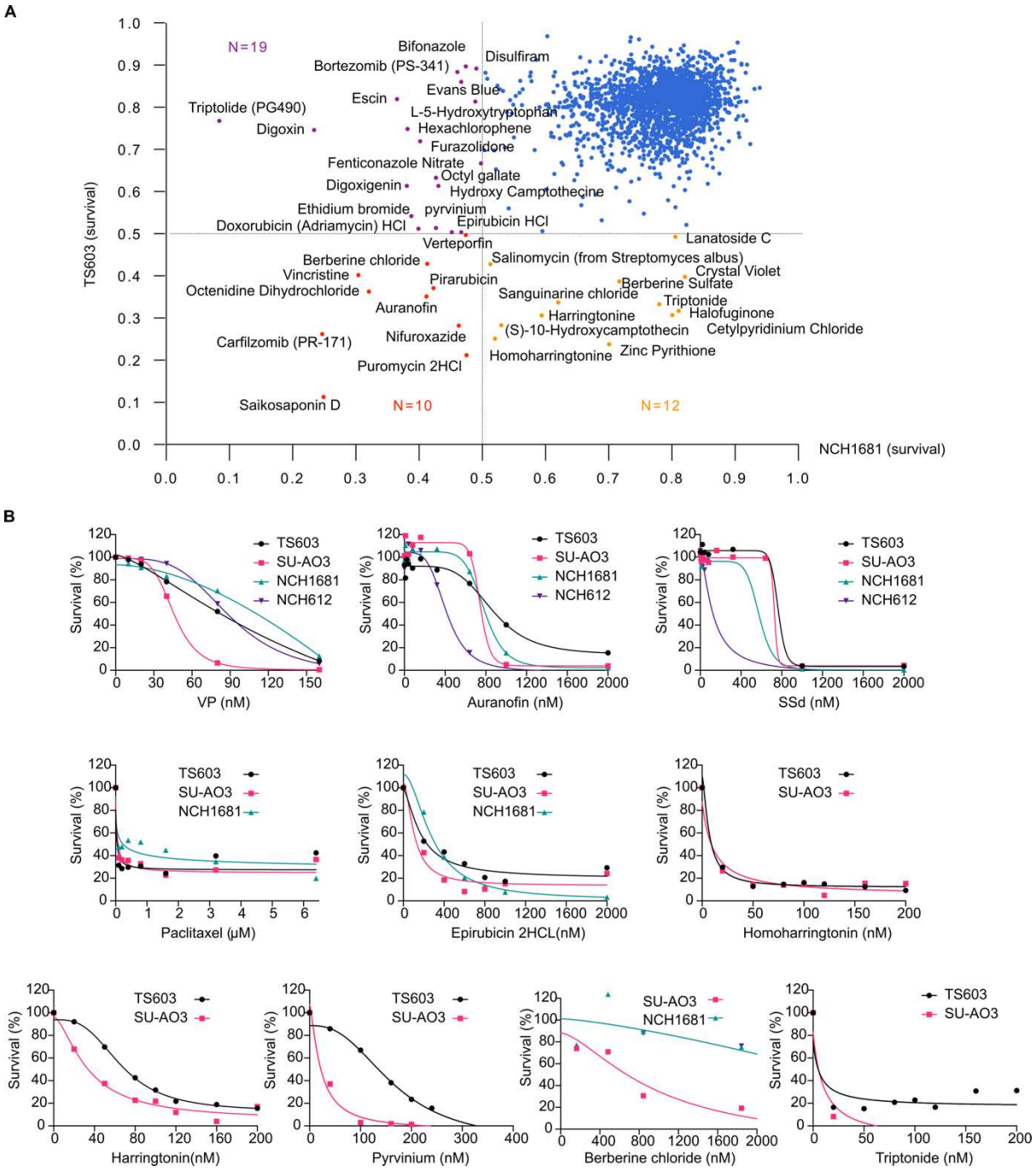

Figure 29. Hit compounds identification and candidates validation.

(A) Viability of TS603 and NCH1681 treated with the drug library. The x-axis represents cell survival in NCH1681, and the y-axis represents cell survival in TS603. The top candidates are labeled in different colors to show efficacy in each cell line or both. (B) Dose-response curves of the candidates determined by the MTT assay. Each dot represents the average of three technical replicates. Figures modified from [88].

FDA-approved drugs		Mechanism of action	BBB-crossing	IC_{50} (nM)			
				TS603	SU-AO3	NCH1681	NCH612
1	VP	disrupt the YAP-TEAD complex	Yes	182.8	45.96	679.7	90.49
2	Auranofin	inhibit the thioredoxin reductase (TrxR) enzyme in mitochondria	Yes	866.1	743.3	783.6	414.1
3	Saikosaponin D (SsD)	calcium mobilizing agent (SERCA inhibitor)	No	763.7	727.7	578.4	124.7
4	Epirubicin 2HCl	inhibit nucleic acid (DNA and RNA) and protein synthesis	No	170.6	106.7	280.5	
5	Paclitaxel (PTX)	Target microtubules	No	36.94	51.32	78.8	
6	Homoharringtonin	Inhibits protein synthesis	No	6.77	10.84		
7	Pyrvinium	Attenuate Hedgehog Signaling Downstream of Smoothened	No	165.5	21.18		
8	Harringtonin	prevent the initial elongation step of protein synthesis	No	66.42	33.21		
9	Triptonin	Stimulate the 5-HT1B receptors on smooth muscle cells of blood vessels	No	6.767	10.29		
10	Berberine Chloride	modulate lipid and glucosemetabolism	No	too less point	954.7	Unstable	too less point

Table 7. IC_{50} of the drug candidates and their reported mechanism of act.
Table is modified from [88].

4.5.3 On/off target study of VP (verteporfin)

After screening, VP was selected for further assessment among the screened candidates due to its potential as an antitumor agent and ability to cross the blood brain barrier. Visudyne, a commercial drug containing VP, is a plant-derived photosensitizer that is FDA-approved to treat macular degeneration, through a process called photodynamic therapy. Recent studies have suggested that VP may have potential as a treatment for some neurodegenerative diseases, such as Alzheimer's and Parkinson's disease. It has been shown to have antitumor effect without light activation and has demonstrated the ability to cross blood-brain barrier with

no observed toxicity in long-term *in vivo* treatment. Additionally, VP is under phase I/II clinical trials for the treatment of recurrent high-grade EGFR-mutated glioblastoma to evaluate its side effects and determine the optimal dosage. To evaluate the potential on/off target effects of VP, I initially examined its impact on YAP1, followed by utilizing mass spectrometry for the identification of true on and off-targets of VP via proteomics.

4.5.3.1 VP exerts its anti-tumor activity in IDH1 mutant PDTs independent of YAP1

VP is known as a YAP1 (Yes-associated protein 1) inhibitor in the absence of light activation, therefore, I sought to determine whether VP exhibits similar YAP1 inhibitory activity in our cell models. YAP1 has been the subject of extensive research in the field of cancer biology. It functions as a transcriptional coactivator, playing a critical role in the regulation of cell proliferation, apoptosis, and stem cell properties. It acts as a downstream effector of the Hippo signaling pathway, which is a key regulator of organ size and tumorigenesis. Dysregulation of the Hippo pathway and aberrant YAP1 activation have been implicated in the development and progression of various types of cancer, including liver, lung, breast, ovarian, pancreatic, and colorectal cancer. In many cases, YAP1 activation promotes cancer cell proliferation, migration, invasion, and resistance to conventional chemotherapy and radiotherapy, rendering it a promising therapeutic target for cancer treatment.

To verify the efficacy of VP, I employed additional cell viability assays-CellTiter-Glo and softagar assays. For CellTiter-Glo assay, 4000 cells are seeded in 96-well plates and treated with VP for 96 hours, and survival is based on the reading normalized to DMSO-treated controls. Our results showed that TS603, SU-AO3, and NCH1681 had IC_{50} values of 95.83 nM, 141.2 nM, and 899.7 nM, respectively (Figure 30A). These values were higher than those obtained the MTT assay (182.8 nM,45.96nM and 697.9nM), but dose response curve and IC_{50} values were not significantly different. For the anchorage-independent colony assay, 100,000 cells were seeded in the middle layer of soft agar in 6-well plates and allowed to grow for one week. The cells were then treated with 1 μM VP or 0.04% DMSO for 1 hour before drug removal and exchange with fresh medium. The cells were grown for an additional month, with medium exchange weekly according to the growth need of the cells. VP-treated wells showed no colony formation, indicating high sensitivity to VP across all PDTs despite differences in IC_{50} values (Figure 30B).

I also detected cytoplasmic accumulations of VP after 30 mins of treatment with 1 μM VP using its autofluorescence in the far-red spectrum (660–780 nm) [101] (Figure 30C).

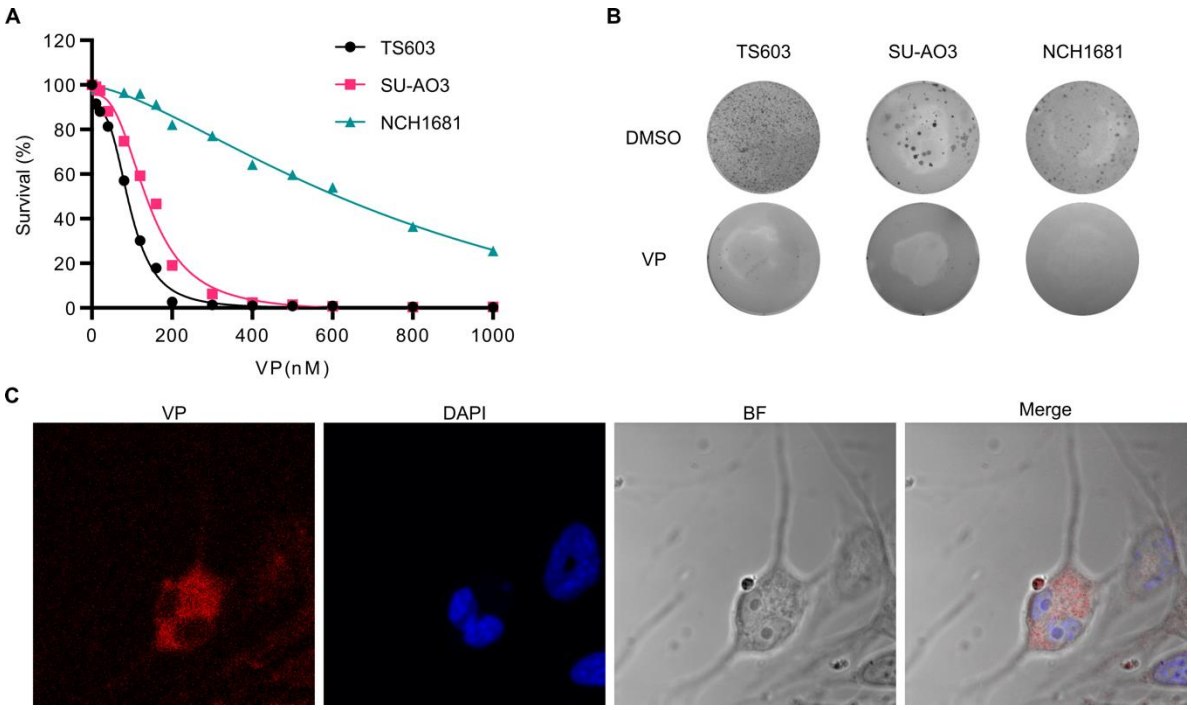

Figure 30. Effects of VP on IDH1 mutant PDTs.
(A) Dose-response curve of VP from CellTiter-Glo assay. 4000 cells are seeded in 96-well plates, and survival is based on the reading relative to DMSO after 96 hours of VP treatment. Each dot represents the average data from three technical repeats. (B) Anchorage-independent colony assay of IDH mutant gliomas upon VP treatment. The indicated glioma lines were seeded in the middle of a soft agar layer for one-week growth, then subjected to 1 μM VP or 0.04% DMSO as a control for 1 h treatment. After removal of the drug, colonies were analyzed after four weeks of growth. (C) Cytoplasmic accumulation of VP accumulates detected in the far-red spectrum at 647 nm in confocal microscopy. The figures have been modified from [88].

I observed a time and dosage dependent decrease in YAP1 protein levels in NCH1681 cells following VP treatment. After a 2-hour treatment period, I observed a significant decrease in the level of YAP1 protein with increasing concentrations of VP, with the most significant decrease observed at a concentration of 1 μM VP (Figure 31A). In the time-course treatment with 1μM VP, I observed that the YAP1 protein level had already decreased significantly after just 30 mins of treatment, and further treatment for up to 3 hours did not result in a significant additional decrease in YAP1 protein levels (Figure 31A).

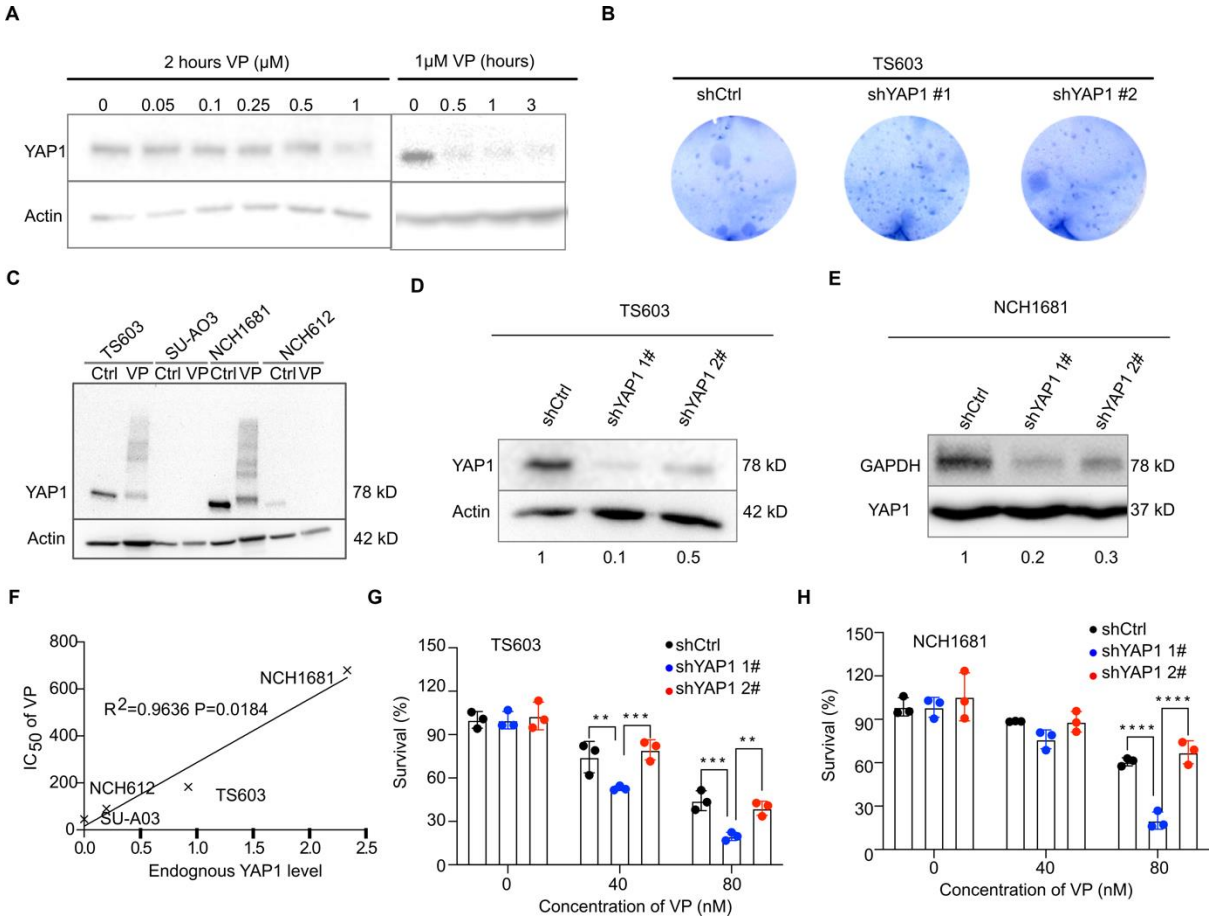

Figure 31. VP antitumor effect is YAP1 independent.

(A) VP inhibits YAP1 protein in a time and dose dependent manner. (B) colony formation of YAP1 knockdown in TS603. All wells are seeded with 10,000 cells in a 12-well plate for 1.5-month growth. (C) IDH mutant PDTs with different endogenous YAP1 level and YAP1 levels decreases upon VP 1μM 2-hour treatment. (D) YAP1 protein levels in ShRNA-mediated YAP1 knockdown in TS603 cell line. Quantification of YAP1 protein levels is indicated below the image. (E) YAP1 protein levels in ShRNA-mediated YAP1 knockdown in NCH1681. Quantification of YAP1 protein levels is indicated below the image. (F) Negative correlation between endogenous YAP1 protein level and IC50 of VP in PDTs. Pearson correlation: R=0.9816, p=0.0184. (G) Survival of TS603 with different shYAP1 know down level upon VP treatment. Data from MTT assay (n=3 technical repeats). Data analyzed with two-way ANOVA, p<0.001. (H) Survival of NCH1681 with different shYAP1 knock down levels. data from MTT assay (n=3 technical repeats). Data analyzed with two-way ANOVA, p<0.001. The figures have been modified from [88].

I observed consistent YAP1 protein degradation upon VP treatment in all 4 PDTs, with varying levels of endogenous YAP1 in each cell line (Figure 31 D). Notably, NCH1681 exhibited the highest levels of YAP1, but did not exhibit the strongest response to VP treatment. In contrast, SU-AO3, which has undetectable YAP1 levels, displayed higher sensitivity to VP exposure (Figure 31F). This negative correlation between YAP1 protein level and IC_{50} of PDTs to VP

suggests that YAP1 may not be the only target of VP. To test this hypothesis, I used shRNA-mediated knockdown of YAP1 in both TS603 and NCH1681 cells. Two shRNAs were employed, resulting in 90% and 50% knockdown in TS603 and 80% and 50% knockdown in NCH1681 (Figure 31 D, E). However, I found that YAP1 loss did not affect the colony formation ability of TS603 (Figure 31B). TS603 cells with varying levels of YAP1 were all sensitive to VP treatment, with no colony formation observed (not shown). Interestingly, I observed that the greatest reduction in YAP1 level led to increased sensitivity to VP treatment. For example, in TS603, shYAP1 1# with 90% of YAP1 knockdown showed lower survival rates to VP at 40 nM and 80 nM for 96 hours of treatment compared to shYAP1 2#, which had only 50% YAP1 knockdown (Figure 31G). Similarly, in NCH1681, shYAP1 1# with 80% YAP1 knockdown showed higher sensitivity than shYAP1 2#, which had 50% YAP1 knockdown (Figure 31H). These results suggest that YAP1 may not be the sole target of VP in our PDTs.

4.5.3.2 Downregulation of nucleocytoplasmic transport pathway in response to VP

To identify the actual target of VP in TMZ-R IDH1 mutant PDT models, I performed whole cell lysate mass spectrometry analysis to examine the global effect of VP on the proteome. I measured 5964 proteins in TS603, SU-AO3 and NCH1681 and identified differentially abundant proteins using an absolute $\log_2$(fold change) cutoff of 2 and a $-\log_{10}$(adjusted P) threshold of 2. VP treatment resulted in significant changes in protein expression levels in all three PDTs, Specifically, 134 proteins were upregulated, and 477 proteins were downregulated in TS603 (Figure 32A), 104 proteins were upregulated, and 363 proteins were downregulated proteins in SU-AO3 (Figure 32C), and 92 proteins were upregulated and 372 proteins were downregulated in NCH1681 (Figure 32 E). I submit those proteins to Metascape, where I analyzed the KEGG (Kyoto Encyclopedia of Genes and Genomes) pathway using the data from enrichment_GO. Each PDT exhibited unique pathways for the up- and down-regulated proteins (Figure 32 B, D, F).

In the upregulated KEGG pathway, I identified 24 enriched KEGG pathways in TS603, 4 in SU-AO3, and 45 in NCH1681, but no common upregulated KEGG pathways were found (Figure 32G). However, in the downregulated KEGG pathways, 25 KEGG pathways were enriched in TS603, 34 in SU-AO3, and 13 in NCH1681, with 7 pathways enriched between them, including amyotrophic lateral sclerosis, nucleocytoplasmic transport, oxidative phosphorylation, thermogenesis, Parkinson's disease, Alzheimer's disease, and pathways of neurodegeneration in multiple diseases (Figure 32 G, H).

Of particular interest was the nucleocytoplasmic transport pathway, which was the most highly ranked enriched KEGG pathway in all three PDTs regarding the enrichment score, -log10 (p value), z score, and gene hits. Nucleocytoplasmic transport is essential for the movement of macromolecules, such as proteins and RNA, between the nucleus and cytoplasm. Dysregulation of nucleocytoplasmic transport has been linked to various diseases, including cancer and neurodegenerative disorders. Our findings suggest that VP may modulate the nucleocytoplasmic transport pathway in TMZ resistant IDH1 mutant PDT models, highlighting its potential as a therapeutic target for these cancers.

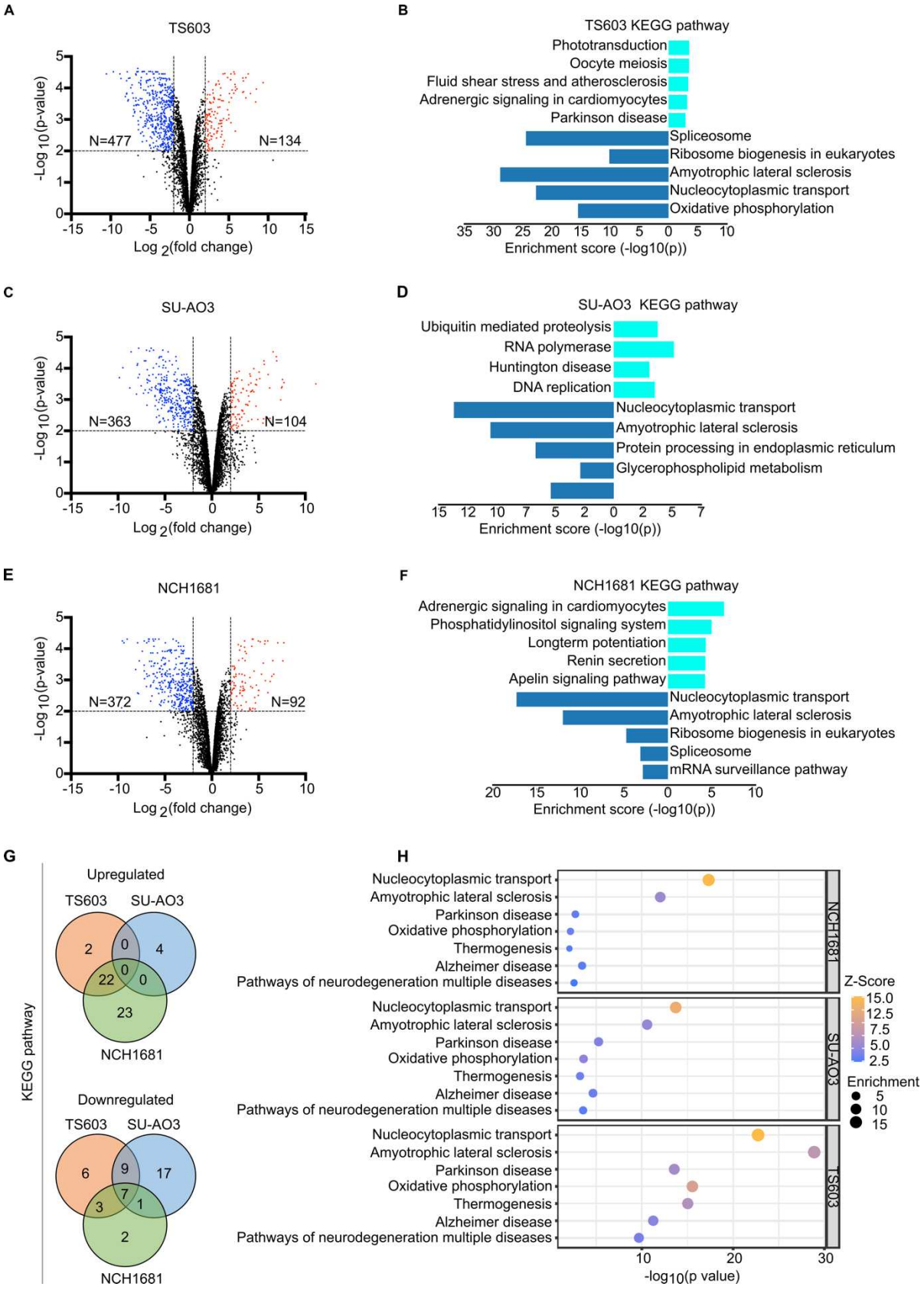

Figure 32. Gene alterations and KEGG pathway enrichment from mass spectrometry analysis. (A, C, E): Volcano plots of protein expression from three independent experiments with TS603, SU-AO3, and NCH1681 treated with 1 μM VP or 0.04% DMSO for 2 hours. The -log10(adjusted p values)

threshold is 2, and log2 protein levels threshold is -2 and 2. (B, D, F): The enriched KEGG pathway in each PDT. Pathways and data were analyzed and downloaded from Metascape, and figures were plotted using SRplot. G. Venn diagram showing commonly up- and down- regulated KEGG pathways. H, Enrichment bubble plot of the seven downregulated KEGG pathways shared by TS603, SU-AO3 and NCH1681. The figures have been modified from [88].

4.5.3.3 Nuclear pore complex (NPC) is the potential target of VP

In addition to the KEGG pathways that were commonly altered across all three IDH1 mutant PDTs, I also examined the commonly altered proteins. I found that only two proteins were consistently upregulated, while 59 proteins were commonly downregulated (Figure 33 A).

To gain insight into the molecular networks, I performed KEGG pathway and biological process analyses on these 59 downregulated proteins using Metascape.
Our KEGG pathway analysis revealed a notable enrichment in the nucleocytoplasmic transport pathway, which was consistent with the previously analyzed shared pathway between the three PDTs when I conducted separate analyses for each PDT (Figure 33 B). Furthermore, I identified the nuclear pore complex (NPC) as the primary biological process affected by VP treatment (Figure 33 B). NPCs have critical roles in the transportation of macromolecules between the nucleus and cytoplasm and are composed of around 30 nucleoporins (NUPs) [34, 35]. Upon further examination of the NUP family in our MS dataset, I observed that almost all NUP family members of NUPs were significantly downregulated in all three PDTs (Figure 33 C, D, E), suggesting a specific impact of VP on this protein family.

These findings provide new insight into the molecular mechanisms underlying the response of IDH1 mutant gliomas to VP treatment and highlight the potential of targeting nuclear pore complex as a therapeutic strategy for this disease.

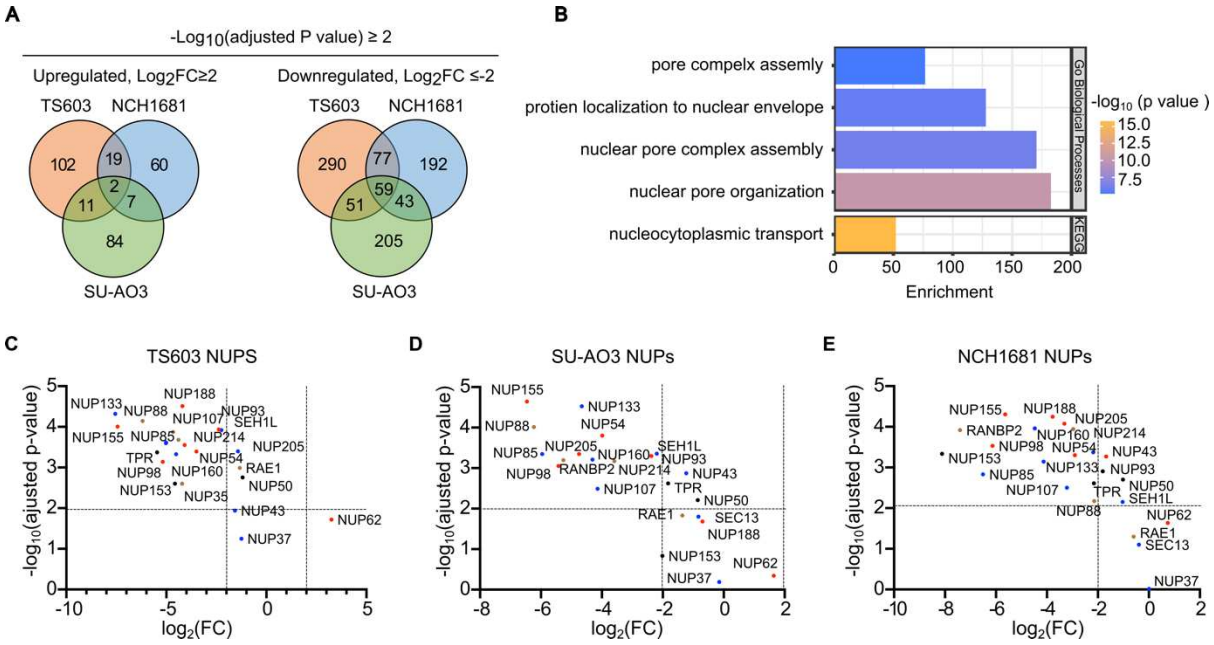

Figure 33. VP treatment specifically targets nuclear pore complex (NPC).
(A) Venn diagrams demonstrating the overlap of VP-driven translational changes (log2(fold change) ≤-2 or ≥2 and -log10(adjusted P value) ≥2) in the 3 IDH1 mutant PDTs. (B) KEGG pathway analysis revealed nucleocytoplasmic transport as the commonly altered pathway among all tested PDTs, with a corresponding biological process involving the nuclear pore organization. (C,D,E). Nup family member protein levels in the MS data of 3 IDH1 mutant PDTs. Color coding represents different subunits of the nuclear pore complex (NPC). Blue represents coat nuclearporin complex, red represents inner ring NUPs, brown represent cytoplasmic filament NUPs, and black represents nuclear basket. The figures have been modified from [88].

4.5.3.4 NUP107 is deactivated and is an upstream regulator for VP response

In order to identify the upstream regulator responsible for the observed response to VP treatment in each PDT, I conducted an Ingenuity Pathway Analysis (IPA) and found a list of predicted upstream regulators.

IPA analysis predicted a total of 128 upstream regulators in TS603, 121 in SU-AO3, and 178 in NCH1681, with 12 proteins predicted to be commonly regulated, including CST5, RAB1B, NUP133, NUP107, NUP93, COPS5, BCAP31, NTF3, mir-1, CLOCK, MYC, ASPSCR1-TFE3 (Figure 34 A). However, some genes in the predicted list for the cell line lack vital information, such as their predicted activation state. Therefore, I narrowed down our focus to genes with defined activation states. Using this criteria, I identified 12 candidates in TS603, 6 in SU-AO3 and 7 in NCH1681 (Figure 34 A). Among these candidates, only two upstream regulators, CST5 and NUP107, were commonly shared across all three cell lines. CST5 was

precited to be activated, but its expr log ratio was not available from the prediction. Therefore, I focused our attention on NUP107 as a potential upstream regulator for the observed response to VP treatment (Figure 34 B).

Since NUP107 was predicted to be an inhibited upstream regulator, I conducted a Western blot analysis to verify this prediction and observed a significant reduction in NUP107 protein levels following VP treatment (Figure 34 C). This result suggests that NUP107 may play a crucial role in the response to VP treatment across multiple PDTs.
To gain further insight into the degradation pathway of NUP107, I tested whether it is broken down by the proteasome, which is one of the three main protein degradation pathways in cells, alongside the lysosomal and autophagy pathways. However, our treatment with MG132, a proteasome inhibitor, failed to rescue NUP107 protein degradation (Figure 34 D), indicating that NUP107 is likely degraded through a proteasome-independent pathway. Additional investigation is needed to determine the specific pathway involved in NUP107 degradation.

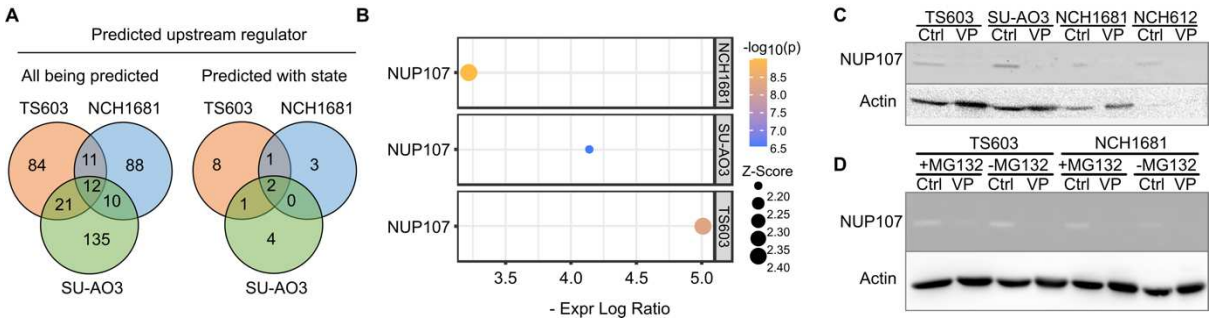

Figure 34. NUP107 is an upstream regulator inhibited in response to VP treatment.
(A) Venn diagram showing the predicted upstream regulators shared among TS603, NCH1681, and SU-AO3. (B) Enrichment bubble plot of the commonly shared upstream regulator NUP107 in TS603, SU-AO3, and NCH1681. (C) Western blot analysis confirms a significant reduction in NUP107 protein levels following 1 µM VP treatment for 1 hour in all four tested PDTs. (D) Proteasome inhibition using MG132 did not rescue NUP107 degradation upon VP treatment, indicating that NUP107 is likely degraded through a proteasome-independent pathway. The figures have been modified from [88].

4.5.3.5 High NUP107 expression correlates with poor patient survival in astrocytoma

Expanding upon the discovery of NUP107 as an upstream regulator in response to VP treatment in our IDH1 mutant PDTs, I aimed to explore the biological significance of NUP107 expression levels in IDH1 mutant gliomas and its correlation with patient survival. To

investigate this, I conducted an analysis utilizing two cancer genomic data platforms: TCGA and the CGGA.

Analysis of the TCGA dataset revealed a significant increase in NUP107 expression in IDH mut-codel, IDH mut-non-codel, and IDH WT samples compared to normal tissues ($p<0.0001$, ordinary one-way ANOVA). However, no significant difference in NUP107 expression was observed between the IDH mut-codel and IDH mut-non-codel subtypes of IDH mutant glioma ($p=0.3918$, ordinary one-way ANOVA) (Figure 35 A). Similar results were obtained when comparing IDH wt and IDH mutant samples in the CGGA dataset (Figure 35 B).

To assess the impact of NUP107 expression on patient survival, I utilized the CGGA dataset, which included survival data from 500 patients with IDH mutation. Using the median log2 expression of NUP107 from IDH mutant glioma (3.2585) as a cutoff, patients were categorized into high or low NUP107 expression groups. I found a significant difference in overall survival between patients with high and low NUP107 expression (median overall survival of 1208 days for NUP107 high and 1582 days for NUP107 low; $p=0.0047$, Gehan-Breslow-Wilcoxon test) (Figure 35 C). Subsequent analysis revealed no significant difference in survival within the IDH mut-codel subgroup (median overall survival of 2549 days for NUP107 high and 2097 days for NUP107 low; $P=0.0677$, Gehan-Breslow-Wilcoxon test) (Figure 35 D). However, within the IDH mut-non-codel subgroup, I observed a significant difference in median overall survival between patients with high NUP107 expression (609 days) and those with low NUP107 expression (1286 days) ($p < 0.0001$, Gehan-Breslow-Wilcoxon test) (Figure 35 E).

These findings indicate that high NUP107 expression is associated with decreased overall survival in IDH mutant glioma, particularly within the IDH mut-codel (astrocytoma) subtypes. Thus, NUP107 expression level may hold potential as a biomarker for predicting patient response to VP treatment.

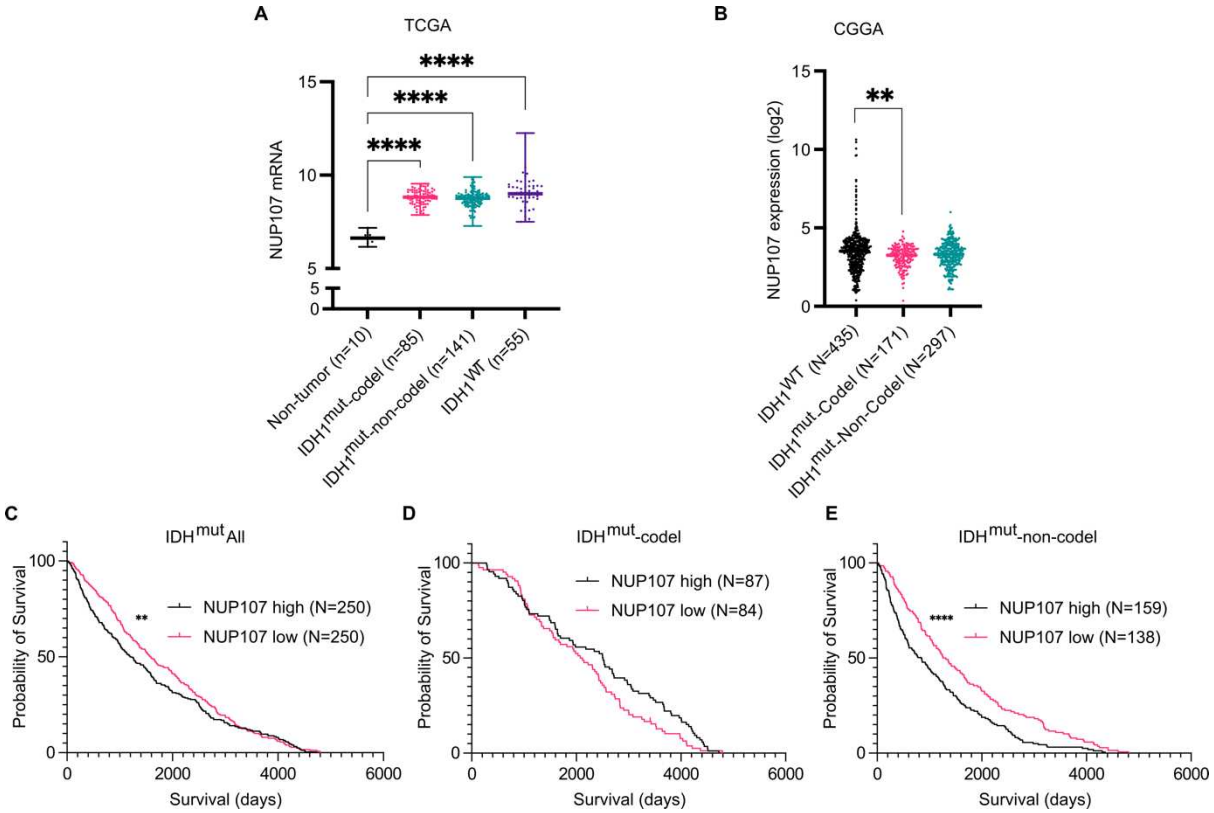

Figure 35. NUP107 expression and patient survival.

(A) NUP107 expression analysis in IDH1 mutant glioma samples from TCGA data showed significant differential expression compared to non-tumor samples ($p<0.0001$, ordinary one-way ANOVA). (B) NUP107 expression analysis in IDH1 mutant glioma samples from CGGA data also showed significant differential expression compared to non-tumor samples ($p=0.0029$, ordinary one-way ANOVA). (C) Kaplan-Meier analysis revealed a significant association between high NUP107 expression and shorter overall survival in IDH1 mutant patients ($p=0.0047$, Gehan-Breslow-Wilcoxon test). (D) No significant difference was observed in overall survival between high and low NUP107 expression in IDH1 mut-codel patients ($p=0.0677$, Gehan-Breslow-Wilcoxon test). (E) Kaplan-Meier analysis showed that higher NUP107 expression was associated with shorter overall survival in IDH1 mut-non-codel astrocytoma patients ($p<0.0001$, Gehan-Breslow-Wilcoxon test). The figures have been modified from [88].

5 Conclusions

The primary objective of this study was to identify potential drug options for the treatment of glioma with IDH1 mutation. I first investigated the molecular mechanisms that determine the sensitivity or resistance to TMZ, with the aim of reversing TMZ sensitivity and enhancing its efficacy in tumor models. Additionally, I aimed to identify synergistic drugs that could be used in combination with TMZ. Furthermore, I explored the possibility of repurposing drugs for the treatment of glioma.

I confirmed three out of four patient-derived tumorspheres (PDTs) from lower-grade gliomas with IDH1 R132 mutations diagnosed as grade 2 and 3 (TS603, SU-AO3, and NCH1681) were resistant to TMZ, while one (NCH612) was sensitive. I tested transcriptional, metabolic, and epigenetic vulnerabilities in the tumor models to identify approaches to reverse TMZ resistance and find synergistic drugs to enhance its efficacy.

For transcriptional analysis, I conducted RNA-seq analysis. KEGG pathway and GO_TRRUST analysis revealed the upregulation of P53 signaling pathway and P53 as an upregulated transcriptional factor. RITA, a P53 activator, was tested alone and in combination with TMZ. Although all four PDTs had Nonsynonymous SNV of P53 mutation, all four PDTs responded to RITA treatment alone. Pre-treating cells with RITA followed by TMZ treatment resulted in strong synergy in TS603 and SU-AO3, strong antagonism in NH612, and slightly additive in NCH1681. Direct RITA and TMZ combination therapy did not show a synergistic effect on the PDTs.

In efforts to investigate metabolome-based strategies for overcoming TMZ resistance, I compared the base level of metabolites and the metabolic changes upon TMZ treatment in TCA cycle, fatty acids, and amino acids using GCMS and MSMS metabolic assays**.** I found significant upregulation of metabolites in TCA cycle. However, inhibiting glucose usage with 2-DG in combination with TMZ treatment only showed efficacy in TS603. I also observed that a high baseline level of fatty acids might correlate with TMZ sensitivity as observed in NCH612. However, inhibiting the enzyme for carnitine synthesis with Mildronate, which blocks the transport of fatty acid into the mitochondria, showed no effect in all four PDTs. Combining Mildronate with TMZ treatment only demonstrated further efficacy in NCH612.

To test epigenetic approaches to reverse or synergize TMZ treatment, I used different treatment regimens of DAC with TMZ combination treatment. All four PDTs responded to DAC, with NCH612 being the most sensitive and NCH1681 being the least sensitive,

followed by TS603 and SU-AO3. Direct combination of DAC and TMZ brought slightly synergistic effects in TS603 and NCH1681 at low drug concentrations, while strong antagonism was observed in SU-AO3 and NCH612. Pre-treatment of cells with DAC followed by TMZ treatment resulted in strong synergy in TS603, SU-AO3, and NCH612, with only an additive effect in NCH1681. RNA-seq analysis of this pre-treatment regimen showed more upregulated genes and enriched pathways compared to either drug treatment alone, with enriched pathways in common being Focal adhesion, ECM-receptor interaction, Phagosome and NOD-like receptor signaling pathways.

In the search for alternative drugs to treat IDH1 mutant TMZ-resistant gliomas, a high-throughput droplet microarray was employed for FDA-approved drug screening. Among the 2208 drugs screened, I identified over 20 alternative drugs to treat IDH1 mutant TMZ-resistant gliomas, with VP being a promising candidate. By studying the mechanism of VP, YAP1 was excluded as its target through western blot and shRNA of YAP1 know down, as cells with low or no YAP1 still respond strongly to VP. I performed total lysate-mass spectrometry analysis to study the protein response to VP treatment. I found that pathways related to nucleocytoplasmic transportation were significantly downregulated and identified that almost all components of the nuclear pore complex were also downregulated. Ingenuity Pathway Analysis showed that NUP107 is a potential upstream regulator associated with response to VP, and I further validate the decrease of the protein with western blot and identified its degradation is proteosome independent. Additionally, publicly available large-scale cancer genomics data from TCGA and CCGA shows a significant correlation between high NUP107 gene expression levels and decreased patient survival in IDH1 mutant astrocytoma.

Overall, the work presented in this thesis suggest that a combination of P53 activator RITA and TMZ, glucose inhibitor 2-DG and TMZ, Mildronate and TMZ, and DAC pre-treatment followed by TMZ may reverse TMZ resistance and enhance its efficacy in some lower-grade gliomas with IDH1 R132 mutations. Additionally, VP is a promising candidate as an alternative drug to treat IDH1 mutant TMZ-resistant gliomas, potentially through downregulating the NUP107 protein.

6 Discussion

6.1 The variable sensitivity to TMZ and molecular mechanisms

The sensitivity or resistance of TMZ treatment among the four IDH1 mutant PDTs remains unclear. NCH612, TS603, and SU-AO3, which have 1p/19q codeletion and are oligodendrogliomas, exhibit varying levels of sensitivity to TMZ, while NCH1681, with intact 1p/19q deletion, is the least sensitive. Clinical treatment of patients before cell culture may contribute to this difference. Further analysis suggests that upregulation of pathways and metabolites in NCH612 might explain its higher sensitivity. However, it is possible that the other three lines have already developed stable transcriptome and metabolome profiles that are not responsive to TMZ. Therefore, additional cell lines with varying TMZ sensitivity are needed to identify universal markers for predicting TMZ response.

6.2 Different synergistic responses to RITA and TMZ Combination

The four PDTs exhibit varying synergistic responses to pre-treatment with RITA, a P53 activator, followed by TMZ treatment. TS603 and SU-AO3 show strong synergy, NH612 shows antagonism, and NCH1681 only shows a slight additive effect. The upregulation of P53 in NCH612 upon TMZ treatment may contribute to resistance rather than sensitivity. To confirm this, further experiments targeting P53 inactivation and assessing TMZ sensitivity are necessary. Since RITA may activate the P53 pathway differently among the four IDH1 mutant PDTs, monitoring gene expression in the P53 signaling pathway before TMZ combination treatment is crucial. Other factors, such as DNA damage response pathways and drug uptake/metabolism, may also influence the response to combination treatment. Further investigations are required to elucidate the involvement of the P53 signaling pathway in TMZ resistance.

6.3 Determinants of tumor metabolism and drug synergy

The efficacy of combining 2-DG with TMZ treatment is observed mainly in TS603, which exhibits the lowest baseline level of TCA cycle metabolites. This suggests that cells with lower levels of TCA metabolites may be more susceptible to this treatment. Considering the metabolic state of cancer cells is crucial for designing effective treatment strategies, particularly in glioma and other cancers.

The high baseline level of fatty acids correlates with TMZ sensitivity, as observed in NCH612. Combining Mildronate with TMZ treatment enhances efficacy in NCH612, suggesting that cells with high fatty acid requirements may be more vulnerable to TMZ treatment. Further studies targeting fatty acid transportation, fatty acid supply deprivation, or measuring fatty acid ß-oxidation rates can provide more direct insights into the impact of fatty acid energy supply on TMZ sensitivity. These findings also highlight the importance of controlling dietary fat intake during chemotherapy.

Metabolic preferences in tumors are determined by a combination of factors. Intrinsic factors, such as genetic alterations, cell lineage/tissue of origin, histological subtype, and tumor grade, influence tumor metabolism. Extrinsic factors, including nutrient and oxygen availability, extracellular matrix attachment, stromal cell interactions, and exposure to radiation and chemotherapy, also play a role. The integration of these factors creates metabolic dependencies in tumors. Understanding the context-specific metabolic preferences and vulnerabilities in malignant cells is essential for exploiting cancer metabolism for clinical benefit.

6.5 Different efficacy of DAC and TMZ combination treatment

The varying response of cells to DAC indicates that NCH612 is the most sensitive, followed by TS603 and SU-AO3, while NCH1681 is the least sensitive. It would be valuable to compare the initial methylation status of the four PDTs and observe changes in methylation upon DAC treatment. The lack of response in NCH1681 may be due to its non-hypermethylated state, rendering DAC ineffective in altering its methylation profile. Confirming this hypothesis requires further testing. If proven true, the hypermethylation status of cells could serve as a potential marker for predicting TMZ response.

Pre-treatment of cells with DAC followed by TMZ shows greater efficacy than combining the two drugs directly. Additionally, more genes and genetic pathways are upregulated, indicating enhanced drug effects. These altered pathways involve interactions with extracellular components, cell adhesion, and immune response processes. These findings underscore the importance of targeting extracellular interactions and processes for novel therapeutic approaches and emphasize the need to understand the precise mechanisms of drug action.

6.6 Potential of NPC targeting for treating IDH1 mutant TMZ-resistant glioma

My study highlights the potential of targeting the nucleopore complex (NPC) as a novel pathway for the treatment of IDH1 mutant gliomas. Further validation, such as genetic knockdown of NUP107 and investigating the mechanism by which VP destroys nucleoporins, is necessary. Exploring the functional and structural redundancy of nucleoporins and understanding their degradation in response to VP treatment will provide insights into potential drug resistance. The efficient and rapid response observed in this pathway could also guide the clinical design of drug treatment regimens.

6.7 Challenges and future directions

Experimental design and data analysis in glioma research face several challenges, including cell context-dependent effects, heterogeneity, and plasticity. To overcome these challenges, thorough characterization of brain tumors through histological studies, single-cell RNA sequencing, and methylation profiling is necessary. Statistical approaches such as single-cell sequencing and clustering analysis can help identify and correct for heterogeneity and plasticity effects. Stratified sampling and factorial designs are essential to ensure the representation of cell subpopulations and identify variable interactions. Validation across multiple cell models further strengthens the robustness of findings.

The development of effective therapeutic strategies for glioma necessitates the integration of complex genomic, transcriptomic, epigenomic, and proteomic programs. However, individualization is critical to tailor treatment approaches and improve their efficacy. By considering the unique characteristics of each patient's tumor, personalized medicine can be advanced, enabling the identification of specific drug therapies that address their individual needs.

The DMA platform has demonstrated its capability in generating high-density single-spheroid arrays, providing a convenient means for direct live microscopy-based characterizations. This innovative tool offers an affordable and efficient solution, particularly for patients experiencing tumor recurrence after standard treatment with limited alternative drug options. In the future, the potential exists to acquire patient samples and utilize FDA-approved drug screening to identify the most suitable drug or drug combination for each individual. This integration of personalized medicine holds promise for the development of tailored drug therapies that align with the unique characteristics of each patient's tumor.

In conclusion, effective treatment strategies in glioma research require targeting interactions with extracellular components, understanding drug mechanisms, and addressing metabolic preferences. The findings presented in this study contribute valuable insights into the interplay of signaling pathways and their role in determining drug sensitivity in different cells. By overcoming experimental challenges, pursuing personalized approaches, and leveraging innovative tools like the DMA platform, the field can advance toward more effective and tailored treatments for glioma patients.

7 References

1. Turcan, S., et al., IDH1 mutation is sufficient to establish the glioma hypermethylator phenotype. Nature, 2012. 483(7390): p. 479-83.
2. Ostrom, Q.T., et al., CBTRUS Statistical Report: Primary Brain and Other Central Nervous System Tumors Diagnosed in the United States in 2015–2019. Neuro-Oncology, 2022. 24(Supplement_5): p. v1-v95.
3. Suzuki, H., et al., Mutational landscape and clonal architecture in grade II and III gliomas. Nat Genet, 2015. 47(5): p. 458-68.
4. Cahill, D. and S. Turcan, Origin of Gliomas. Semin Neurol, 2018. 38(1): p. 5-10.
5. Melin, B., Genetic causes of glioma: new leads in the labyrinth. Curr Opin Oncol, 2011. 23(6): p. 643-7.
6. Louis, D.N., et al., The 2021 WHO Classification of Tumors of the Central Nervous System: a summary. Neuro-Oncology, 2021. 23(8): p. 1231-1251.
7. Blum, A., P. Wang, and J.C. Zenklusen, SnapShot: TCGA-Analyzed Tumors. Cell, 2018. 173(2): p. 530.
8. Zhao, Z., et al., Chinese Glioma Genome Atlas (CGGA): A Comprehensive Resource with Functional Genomic Data from Chinese Glioma Patients. Genomics Proteomics Bioinformatics, 2021. 19(1): p. 1-12.
9. Weller, M., et al., EANO guidelines on the diagnosis and treatment of diffuse gliomas of adulthood. Nature Reviews Clinical Oncology, 2021. 18(3): p. 170-186.
10. Louis, D.N., et al., The 2021 WHO Classification of Tumors of the Central Nervous System: a summary. Neuro Oncol, 2021. 23(8): p. 1231-1251.
11. Weller, M., et al., Glioma. Nature Reviews Disease Primers, 2015. 1(1): p. 15017.
12. Duffau, H. and L. Taillandier, New concepts in the management of diffuse low-grade glioma: Proposal of a multistage and individualized therapeutic approach. Neuro Oncol, 2015. 17(3): p. 332-42.
13. Boots-Sprenger, S.H.E., et al., Significance of complete 1p/19q co-deletion, IDH1 mutation and MGMT promoter methylation in gliomas: use with caution. Modern Pathology, 2013. 26(7): p. 922-929.
14. Yang, K., et al., Glioma targeted therapy: insight into future of molecular approaches. Mol Cancer, 2022. 21(1): p. 39.
15. Mohile, N.A., et al., Therapy for Diffuse Astrocytic and Oligodendroglial Tumors in Adults: ASCO-SNO Guideline. J Clin Oncol, 2022. 40(4): p. 403-426.
16. Parsons, D.W., et al., An integrated genomic analysis of human glioblastoma multiforme. Science, 2008. 321(5897): p. 1807-12.

17. Xu, W., et al., Oncometabolite 2-hydroxyglutarate is a competitive inhibitor of α-ketoglutarate-dependent dioxygenases. Cancer Cell, 2011. 19(1): p. 17-30.
18. Miller, J.J., et al., Isocitrate dehydrogenase-mutant glioma: evolving clinical and therapeutic implications. Cancer, 2017. 123(23): p. 4535-4546.
19. Choi, C., et al., 2-hydroxyglutarate detection by magnetic resonance spectroscopy in IDH-mutated patients with gliomas. Nature medicine, 2012. 18(4): p. 624-629.
20. Rohle, D., et al., An inhibitor of mutant IDH1 delays growth and promotes differentiation of glioma cells. Science, 2013. 340(6132): p. 626-630.
21. Reitman, Z.J. and H. Yan, Isocitrate dehydrogenase 1 and 2 mutations in cancer: alterations at a crossroads of cellular metabolism. J Natl Cancer Inst, 2010. 102(13): p. 932-41.
22. Yan, H., et al., IDH1 and IDH2 mutations in gliomas. New England journal of medicine, 2009. 360(8): p. 765-773.
23. Molenaar, R.J., et al., Wild-type and mutated IDH1/2 enzymes and therapy responses. Oncogene, 2018. 37(15): p. 1949-1960.
24. Louis, D.N., et al., The 2016 World Health Organization classification of tumors of the central nervous system: a summary. Acta neuropathologica, 2016. 131: p. 803-820.
25. Yang, H., et al., IDH1 and IDH2 mutations in tumorigenesis: mechanistic insights and clinical perspectives. Clin Cancer Res, 2012. 18(20): p. 5562-71.
26. Reitman, Z.J., et al., Profiling the effects of isocitrate dehydrogenase 1 and 2 mutations on the cellular metabolome. Proc Natl Acad Sci U S A, 2011. 108(8): p. 3270-5.
27. Hvinden, I.C., et al., Metabolic adaptations in cancers expressing isocitrate dehydrogenase mutations. Cell Rep Med, 2021. 2(12): p. 100469.
28. Tretter, L. and V. Adam-Vizi, Alpha-ketoglutarate dehydrogenase: a target and generator of oxidative stress. Philos Trans R Soc Lond B Biol Sci, 2005. 360(1464): p. 2335-45.
29. Yoo, H.C., et al., Glutamine reliance in cell metabolism. Exp Mol Med, 2020. 52(9): p. 1496-1516.
30. Baksh, S.C. and L.W.S. Finley, Metabolic Coordination of Cell Fate by α-Ketoglutarate-Dependent Dioxygenases. Trends Cell Biol, 2021. 31(1): p. 24-36.
31. Kaelin, W.G., Jr. and S.L. McKnight, Influence of metabolism on epigenetics and disease. Cell, 2013. 153(1): p. 56-69.
32. Losman, J.-A., P. Koivunen, and W.G. Kaelin, 2-Oxoglutarate-dependent dioxygenases in cancer. Nature Reviews Cancer, 2020. 20(12): p. 710-726.
33. Lu, C., et al., IDH mutation impairs histone demethylation and results in a block to cell differentiation. Nature, 2012. 483(7390): p. 474-8.

34. Noushmehr, H., et al., Identification of a CpG island methylator phenotype that defines a distinct subgroup of glioma. Cancer Cell, 2010. 17(5): p. 510-22.
35. Malta, T.M., et al., Glioma CpG island methylator phenotype (G-CIMP): biological and clinical implications. Neuro Oncol, 2018. 20(5): p. 608-620.
36. Li, K.K., et al., Identification of subsets of IDH-mutant glioblastomas with distinct epigenetic and copy number alterations and stratified clinical risks. Neurooncol Adv, 2019. 1(1): p. vdz015.
37. Mellinghoff, I.K., et al., Vorasidenib, a Dual Inhibitor of Mutant IDH1/2, in Recurrent or Progressive Glioma; Results of a First-in-Human Phase I Trial. Clin Cancer Res, 2021. 27(16): p. 4491-4499.
38. Stupp, R., et al., Radiotherapy plus concomitant and adjuvant temozolomide for glioblastoma. N Engl J Med, 2005. 352(10): p. 987-96.
39. Johnson, D.R. and B.P. O'Neill, Glioblastoma survival in the United States before and during the temozolomide era. J Neurooncol, 2012. 107(2): p. 359-64.
40. Newlands, E.S., et al., Temozolomide: a review of its discovery, chemical properties, pre-clinical development and clinical trials. Cancer Treat Rev, 1997. 23(1): p. 35-61.
41. Denny, B.J., et al., NMR and molecular modeling investigation of the mechanism of activation of the antitumor drug temozolomide and its interaction with DNA. Biochemistry, 1994. 33(31): p. 9045-51.
42. Ostermann, S., et al., Plasma and cerebrospinal fluid population pharmacokinetics of temozolomide in malignant glioma patients. Clin Cancer Res, 2004. 10(11): p. 3728-36.
43. Portnow, J., et al., The neuropharmacokinetics of temozolomide in patients with resectable brain tumors: potential implications for the current approach to chemoradiation. Clin Cancer Res, 2009. 15(22): p. 7092-8.
44. Rosso, L., et al., A new model for prediction of drug distribution in tumor and normal tissues: pharmacokinetics of temozolomide in glioma patients. Cancer Res, 2009. 69(1): p. 120-7.
45. Zhang, J., M.F. Stevens, and T.D. Bradshaw, Temozolomide: mechanisms of action, repair and resistance. Curr Mol Pharmacol, 2012. 5(1): p. 102-14.
46. Roos, W.P., et al., Apoptosis in malignant glioma cells triggered by the temozolomide-induced DNA lesion O6-methylguanine. Oncogene, 2007. 26(2): p. 186-97.
47. Yu, W., et al., O(6)-Methylguanine-DNA Methyltransferase (MGMT): Challenges and New Opportunities in Glioma Chemotherapy. Front Oncol, 2019. 9: p. 1547.
48. Chatterjee, N. and G.C. Walker, Mechanisms of DNA damage, repair, and mutagenesis. Environ Mol Mutagen, 2017. 58(5): p. 235-263.

49. Butler, M., et al., MGMT Status as a Clinical Biomarker in Glioblastoma. Trends Cancer, 2020. 6(5): p. 380-391.
50. Sun, X. and S. Turcan, From Laboratory Studies to Clinical Trials: Temozolomide Use in IDH-Mutant Gliomas. Cells, 2021. 10(5).
51. Caccese, M., et al., Mismatch-Repair Protein Expression in High-Grade Gliomas: A Large Retrospective Multicenter Study. Int J Mol Sci, 2020. 21(18).
52. Reddel, R. and A. Aref, Targeting brain cancer. Science, 2022. 377(6605): p. 467-468.
53. Johnson, B.E., et al., Mutational analysis reveals the origin and therapy-driven evolution of recurrent glioma. Science, 2014. 343(6167): p. 189-193.
54. Daniel, P., et al., Temozolomide Induced Hypermutation in Glioma: Evolutionary Mechanisms and Therapeutic Opportunities. Front Oncol, 2019. 9: p. 41.
55. Touat, M., et al., Mechanisms and therapeutic implications of hypermutation in gliomas. Nature, 2020. 580(7804): p. 517-523.
56. Goel, N.J., et al., Economic implications of the modern treatment paradigm of glioblastoma: an analysis of global cost estimates and their utility for cost assessment. J Med Econ, 2021. 24(1): p. 1018-1024.
57. Chen, J., et al., Cost-Effectiveness of Short-Course Radiation Plus Temozolomide for the Treatment of Newly Diagnosed Glioblastoma Among Elderly Patients in China and the United States. Front Pharmacol, 2021. 12: p. 743979.
58. Messali, A., J.W. Hay, and R. Villacorta, The cost-effectiveness of temozolomide in the adjuvant treatment of newly diagnosed glioblastoma in the United States. Neuro Oncol, 2013. 15(11): p. 1532-42.
59. Al-Lazikani, B., U. Banerji, and P. Workman, Combinatorial drug therapy for cancer in the post-genomic era. Nat Biotechnol, 2012. 30(7): p. 679-92.
60. Maynard, A., et al., Therapy-Induced Evolution of Human Lung Cancer Revealed by Single-Cell RNA Sequencing. Cell, 2020. 182(5): p. 1232-1251.e22.
61. Menden, M.P., et al., Community assessment to advance computational prediction of cancer drug combinations in a pharmacogenomic screen. Nat Commun, 2019. 10(1): p. 2674.
62. Chapman, P.B., et al., Improved survival with vemurafenib in melanoma with BRAF V600E mutation. N Engl J Med, 2011. 364(26): p. 2507-16.
63. Lim, Z.F. and P.C. Ma, Emerging insights of tumor heterogeneity and drug resistance mechanisms in lung cancer targeted therapy. J Hematol Oncol, 2019. 12(1): p. 134.
64. DeVita, V.T. and P.S. Schein, The use of drugs in combination for the treatment of cancer: rationale and results. N Engl J Med, 1973. 288(19): p. 998-1006.

65. Bayat Mokhtari, R., et al., Combination therapy in combating cancer. Oncotarget, 2017. 8(23): p. 38022-38043.
66. Plana, D., A.C. Palmer, and P.K. Sorger, Independent Drug Action in Combination Therapy: Implications for Precision Oncology. Cancer Discov, 2022. 12(3): p. 606-624.
67. Arrowsmith, J., Phase II failures: 2008–2010. Nature Reviews Drug Discovery, 2011. 10(5): p. 328-329.
68. Goldie, J.H. and A.J. Coldman, A mathematic model for relating the drug sensitivity of tumors to their spontaneous mutation rate. Cancer Treat Rep, 1979. 63(11-12): p. 1727-33.
69. Chou, T.C. and P. Talalay, Quantitative analysis of dose-effect relationships: the combined effects of multiple drugs or enzyme inhibitors. Adv Enzyme Regul, 1984. 22: p. 27-55.
70. Loewe, S., Die quantitativen probleme der pharmakologie. Ergebnisse der Physiologie, 1928. 27(1): p. 47-187.
71. Berenbaum, M.C., The expected effect of a combination of agents: the general solution. J Theor Biol, 1985. 114(3): p. 413-31.
72. Hoelder, S., P.A. Clarke, and P. Workman, Discovery of small molecule cancer drugs: successes, challenges and opportunities. Mol Oncol, 2012. 6(2): p. 155-76.
73. Slamon, D.J., et al., Use of chemotherapy plus a monoclonal antibody against HER2 for metastatic breast cancer that overexpresses HER2. N Engl J Med, 2001. 344(11): p. 783-92.
74. Cunningham, D., et al., Cetuximab monotherapy and cetuximab plus irinotecan in irinotecan-refractory metastatic colorectal cancer. N Engl J Med, 2004. 351(4): p. 337-45.
75. Rodon, J., J. Perez, and R. Kurzrock, Combining targeted therapies: practical issues to consider at the bench and bedside. Oncologist, 2010. 15(1): p. 37-50.
76. Wang, X., H. Zhang, and X. Chen, Drug resistance and combating drug resistance in cancer. Cancer Drug Resist, 2019. 2(2): p. 141-160.
77. de la Fuente, M.I., et al., Olutasidenib (FT-2102) in patients with relapsed or refractory IDH1-mutant glioma: A multicenter, open-label, phase Ib/II trial. Neuro Oncol, 2023. 25(1): p. 146-156.
78. Pushpakom, S., et al., Drug repurposing: progress, challenges and recommendations. Nat Rev Drug Discov, 2019. 18(1): p. 41-58.
79. Gupta, S.C., et al., Cancer drug discovery by repurposing: teaching new tricks to old dogs. Trends Pharmacol Sci, 2013. 34(9): p. 508-17.

80. Zhang, Z., et al., Overcoming cancer therapeutic bottleneck by drug repurposing. Signal Transduct Target Ther, 2020. 5(1): p. 113.
81. Gelijns, A.C., N. Rosenberg, and A.J. Moskowitz, Capturing the unexpected benefits of medical research. N Engl J Med, 1998. 339(10): p. 693-8.
82. Cha, Y., et al., Drug repurposing from the perspective of pharmaceutical companies. Br J Pharmacol, 2018. 175(2): p. 168-180.
83. Hennekens, C.H., M.L. Dyken, and V. Fuster, Aspirin as a therapeutic agent in cardiovascular disease: a statement for healthcare professionals from the American Heart Association. Circulation, 1997. 96(8): p. 2751-3.
84. Escher, C.M., et al., Botulinum toxin in the management of chronic migraine: clinical evidence and experience. Ther Adv Neurol Disord, 2017. 10(2): p. 127-135.
85. Novac, N., Challenges and opportunities of drug repositioning. Trends Pharmacol Sci, 2013. 34(5): p. 267-72.
86. Riva, L., et al., Discovery of SARS-CoV-2 antiviral drugs through large-scale compound repurposing. Nature, 2020. 586(7827): p. 113-119.
87. Krishnamurthy, N., et al., Drug repurposing: a systematic review on root causes, barriers and facilitators. BMC Health Serv Res, 2022. 22(1): p. 970.
88. Cui, H., et al., Repurposing FDA-Approved Drugs for Temozolomide-Resistant IDH1 Mutant Glioma Using High-Throughput Miniaturized Screening on Droplet Microarray Chip. Advanced Healthcare Materials. n/a(n/a): p. 2300591.
89. Burmakin, M., et al., Dual Targeting of Wild-Type and Mutant p53 by Small Molecule RITA Results in the Inhibition of N-Myc and Key Survival Oncogenes and Kills Neuroblastoma Cells In Vivo and In Vitro. Clinical Cancer Research, 2013. 19(18): p. 5092-5103.
90. Martínez-Reyes, I. and N.S. Chandel, Cancer metabolism: looking forward. Nat Rev Cancer, 2021. 21(10): p. 669-680.
91. Warburg, O., On the origin of cancer cells. Science, 1956. 123(3191): p. 309-14.
92. Bonekamp, N.A., et al., Small-molecule inhibitors of human mitochondrial DNA transcription. Nature, 2020. 588(7839): p. 712-716.
93. Cardaci, S., et al., Pyruvate carboxylation enables growth of SDH-deficient cells by supporting aspartate biosynthesis. Nat Cell Biol, 2015. 17(10): p. 1317-26.
94. DeBerardinis, R.J. and N.S. Chandel, We need to talk about the Warburg effect. Nat Metab, 2020. 2(2): p. 127-129.
95. Ghergurovich, J.M., et al., Local production of lactate, ribose phosphate, and amino acids within human triple-negative breast cancer. Med, 2021. 2(6): p. 736-754.
96. Pająk, B., et al., Synergistic Anticancer Effect of Glycolysis and Histone Deacetylases Inhibitors in a Glioblastoma Model. Biomedicines, 2021. 9(12).

97. Pajak, B., et al., 2-Deoxy-d-Glucose and Its Analogs: From Diagnostic to Therapeutic Agents. Int J Mol Sci, 2019. 21(1).
98. Raez, L.E., et al., A phase I dose-escalation trial of 2-deoxy-d-glucose alone or combined with docetaxel in patients with advanced solid tumors. Cancer Chemotherapy and Pharmacology, 2013. 71(2): p. 523-530.
99. Matthiesen, S., R. Jahnke, and M.R. Knittler, A Straightforward Hypoxic Cell Culture Method Suitable for Standard Incubators. Methods Protoc, 2021. 4(2).
100. Turcan, S., et al., Efficient induction of differentiation and growth inhibition in IDH1 mutant glioma cells by the DNMT Inhibitor Decitabine. Oncotarget, 2013. 4(10): p. 1729-36.
101. Gibault, F., et al., Non-photoinduced biological properties of verteporfin. Current medicinal chemistry, 2016. 23(11): p. 1171-1184.

A Publications

Cui, H., **Sun, X.,** Schilling, M., Herold-Mende, C., Reischl, M., Levkin, P. A., Popova, A. A., Turcan, Ş., Repurposing FDA-Approved Drugs for Temozolomide-Resistant IDH1 Mutant Glioma Using High-Throughput Miniaturized Screening on Droplet Microarray Chip. *Adv. Healthcare Mater.* 2023, 2300591. (Co-first authorship)

Engin Demirdizen, Ruslan Al-Ali, Ashwin Narayanan, **Xueyuan Sun**, Julianna Patricia Varga, Bianca Steffl, Manuela Brom, Damir Krunic, Claudia Schmidt, Gabriele Schmidt, Felix Bestvater, Julian Taranda, Şevin Turcan, TRIM67 drives tumorigenesis in oligodendrogliomas through Rho GTPase-dependent membrane blebbing, ***Neuro-Oncology***, 2022; noac233

Sun, Xueyuan, and Sevin Turcan. "From laboratory studies to clinical trials: temozolomide use in IDH-mutant gliomas." **Cells**10.5 (2021): 1225.

Narayanan, Ashwin, Enrique Blanco-Carmona, Engin Demirdizen, **Xueyuan Sun**, Christel Herold-Mende, Matthias Schlesner, and Sevin Turcan. "Nuclei isolation from fresh frozen brain tumors for single-nucleus RNA-seq and ATAC-seq." **JoVE (Journal of Visualized Experiments)** 162 (2020): e61542.

B Acknowlegment

As I approach the end of my PhD journey, I am filled with both excitement and a sense of pride for being a part of such prestigious research teams in the Heidelberg area. None of this would have been possible without the help and support of many individuals.

First and foremost, I am deeply grateful to my supervisor, Dr. Sevin Turcan. Her initial agreement to hire me and her unwavering support throughout the project have been instrumental. Her humble personality and vast scientific knowledge have guided me every step of the way, offering constant encouragement and belief in my abilities. I cannot thank her enough for everything she has done for me during these four and a half years. Her unwavering confidence in my potential has been a driving force that motivated me to overcome challenges. I am truly indebted to her for opening the door to the field of cancer research and guiding me throughout this transformative experience.

I would also like to express my gratitude to my current and previous group members, Dr.Ruslan Al-Ali, Dr. Anna Schönrock, Dr. Engin Demirdizen, Dr. Ashwin Narayanan, Bianca Steffl, Dr. Julian Taranda, Kevin Jimenez-Cowell, Deniz Dogan, Marilin Koch, Minh Deo, and Salam Ullah. Their contributions have created a supportive and warm team environment, and I have cherished the caring and insightful conversations we have had along the way.

I extend my thanks to DKFZ and Heidelberg University for providing valuable platforms, training programs, and organized activities that have not only allowed me to explore scientific career opportunities but have also facilitated the development of invaluable social networks.

I am grateful to the UNITE committees and my TAC committee members, Dr. Haikun Liu, Dr. Christiane Opitz, Prof. Angel Peter, and Dr. Jan Korbel, for their guidance and constructive input at each step of my PhD journey.

I would also like to express my appreciation to my thesis defense committee members, Prof. Peter Angel, Prof. Stefan Wiemann, and Prof. Benedikt Brors for dedicating their time and efforts to reviewing my thesis and contributing to the evaluation of my final PhD defense.

Lastly, I want to acknowledge the unwavering support of my family. Despite their limited education, my parents have always encouraged and supported me in pursuing higher

education. Their vision and belief in the power of knowledge have been fundamental in shaping my academic journey.

I dedicate this achievement to my husband and children, Marcel Rene Kalt, Noah Ming Kalt, and Mia Ling Kalt. Without their love and unwavering support, this PhD journey would not have been possible. My husband's confidence in my abilities and selfless care for our children have been exceptional. He has always reassured me that our children are content and encouraged me to pursue my research without worry. I am immensely grateful for his unwavering support. I am privileged to share the pursuit of a doctoral degree with him. I would also like to express my deepest gratitude to our children, whose happiness and unconditional love have outweighed any challenges along the way. Their hugs and smiles have been a constant source of refreshment during stressful times.

To all those mentioned above, as well as to everyone who has supported me behind the scenes, I extend my heartfelt gratitude.

23. August 2023

Corrigendum to

“Investigating New Drug Options for Temozolomide Resistant IDH1 Mutant Glioma”

PhD thesis

Xueyuan Sun

Doctoral school of the Combined Faculty of Mathematics, Engineering and Natural Sciences of the Ruprecht - Karls - University Heidelberg

The following parts have to be corrected:

Page 30, line 7- line9 :

"In most MGMT-deficient GBM patients, the initial response to TMZ is eventually followed by tumor recurrence coincident with mutations in genes that encode MMR proteins and the development of a hypermutator phenotype." [1] is cited Reddel & Aref, Science, Vol. 377, (2022)

Page 35, line 5:

“MMT status” should be “MMR status”

Page 40, Figure 6.

“Figure 6. IDH mutation status of the PDTs and their growth rate.” [2]is cited and modified from Cui H & Sun X, *Adv Healthc Mater*. 2300591(2023)

Page 61, line 19 – line 21 :

"The contributions of mutant IDH to DNA methylation, histone methylation and the G-CIMP phenotype coalesces to maintain glioma cells in a self-renewing dedifferentiated state, thus, IDH-mutant gliomas are ideal candidates for epigenetic therapies." [3] is cited from Pirozzi & Han, Nature Reviews Clinical Oncology Vol. 18, pages 645–661 (2021)

Page 93, line 27-34:

“The DMA platform has demonstrated its capability in generating high-density single-spheroid arrays, providing a convenient means for direct live microscopy-based characterizations. This innovative tool offers an affordable and efficient solution, particularly for patients experiencing tumor recurrence after standard treatment with limited alternative drug options. In the future, the potential exists to acquire patient samples and utilize FDA-approved drug screening to identify the most suitable drug or drug combination for each

Correspondence to: Xueyuan Sun, Email: lynn07022018@gmail.com

individual. This integration of personalized medicine holds promise for the development of tailored drug therapies that align with the unique characteristics of each patient's tumor.“[2] is cited and modified from Cui H & Sun X, *Adv Healthc Mater*. 2300591(2023)

1. Reddel, R. and A. Aref, *Targeting brain cancer.* Science, 2022. **377**(6605): p. 467-468.
2. Cui, H., et al., *Repurposing FDA-Approved Drugs for Temozolomide-Resistant IDH1 Mutant Glioma Using High-Throughput Miniaturized Screening on Droplet Microarray Chip.* Adv Healthc Mater, 2023: p. e2300591.
3. Pirozzi, C.J. and H. Yan, *The implications of IDH mutations for cancer development and therapy.* Nat Rev Clin Oncol, 2021. **18**(10): p. 645-661.

Correspondence to: Xueyuan Sun, Email: lynn07022018@gmail.com